

**Numerical methods in soil hydrology: TDR waveform analysis and water vapor diode  
simulation**

by

**Zhuangji Wang**

A dissertation submitted to the graduate faculty  
in partial fulfillment of the requirements for the degree of  
**DOCTOR OF PHILOSOPHY**

Major: Soil Science (Soil Physics)

Program of Study Committee:  
Robert Horton, Major Professor  
Daniel Attinger  
Dan B. Jaynes  
James Rossmanith  
Tom Sauer

Iowa State University

Ames, Iowa

2017

Copyright © Zhuangji Wang, 2017. All rights reserved.

## **DEDICATION**

For

My parents, Zhaokuan Wang and Yuye Hu

## TABLE OF CONTENTS

DEDICATION .....	ii
ABSTRACT .....	v
CHAPTER 1. GENERAL INTRODUCTION .....	1
Soil Water Content and Time Domain Reflectometry .....	1
Soil Heat and Water Movement and Water Vapor Diode .....	6
Objectives .....	7
Organization of the Thesis .....	8
References .....	8
CHAPTER 2. TANGENT LINE / SECOND ORDER BOUNDED MEAN OSCILLATION WAVEFORM ANALYSIS FOR SHORT TDR PROBE .....	11
Abstract .....	11
Abbreviation .....	12
Introduction .....	12
Algorithms .....	14
Materials and Methods .....	17
Results and Discussion .....	18
Summary .....	23
Acknowledgements .....	24
References .....	24
Appendix .....	25
CHAPTER 3. A COMPARISON OF SECOND ORDER DERIVATIVE BASED MODELS FOR TIME DOMAIN REFLECTOMETRY WAVEFORM ANALYSIS .....	27
Abstract .....	27
Abbreviation .....	28
Introduction .....	28
Theory .....	31
Materials and Methods .....	35
Results and Discussion .....	37
Conclusions .....	45
Acknowledgements .....	45
References .....	45
CHAPTER 4. THE IMPACT OF WATER VAPOR DIODES ON SOIL WATER REDISTRIBUTION .....	48
Abstract .....	48
Abbreviation .....	49
Introduction .....	49
Theory .....	50
Materials and Methods .....	54
Results and Discussion .....	58
Summary .....	63
Acknowledgements .....	64

References .....	64
Appendix A .....	66
Appendix B .....	69
CHAPTER 5. A TWO-DIMENSIONAL SIMULATION OF WATER VAPOR DIODES..	71
Abstract .....	71
Abbreviation .....	72
Introduction .....	72
Materials and Methods .....	73
Results and Discussion .....	80
Summary .....	83
Acknowledgements .....	84
References .....	84
CHAPTER 6. GENERAL CONCLUSIONS .....	87
APPENDIX: NUMERICAL SCHEMES FOR CHAPTER 4 AND CHAPTER 5 .....	88
Numerical Scheme for Chapter 4 .....	88
Numerical Scheme for Chapter 5 .....	89
ACKNOWLEDGEMENTS .....	91

## ABSTRACT

Soil water content impacts all soil physical, chemical and biological properties. Soil water movement in shallow soil layers has critical importance for plant water use, foundation stability, energy transfer and chemical diffusion. Numerical analysis is one way to study soil water. New numerical methods are presented in this thesis to determine soil water content from time domain reflectometry (TDR) measurements and simulate soil water accumulation in selected soil layers. TDR enables nondestructive and continuous soil water content measurements. Traditional TDR waveguides have relatively long probes ( $>150$  mm), but new TDR waveguides tend to use short probes ( $<40$  mm) to enable the measurements of water content near the soil surface. However, analyzing TDR waveforms obtained with short TDR probes can be challenging for traditional numerical analysis methods. A new numerical method is needed for analyzing the short-probe TDR waveforms. Coupled heat and water movement can be used to describe the liquid water and water vapor fluxes under combined soil matric potential gradients and thermal gradients. Water vapor flux is the dominant means of soil water movements in relatively dry soil layers. If the naturally occurring water vapor fluxes can be controlled, it is possible to impact the water content distribution in soil profiles. A water vapor diode (WVD), acting as a check valve, allows water vapor flux to occur only in one direction but heat flux occurs in both directions. By installing a subsurface WVD, it is possible to impose direction-controlled vapor fluxes, and WVDs can be used to accumulate or remove water in particular soil layers. However, necessary properties of the WVDs should be clearly defined, and the performance of the WVD should be investigated. Thus, the objectives of this thesis are to (1) develop a new tangent line/second order bounded mean oscillation (TL-BMO) model for analyzing short-probe TDR waveforms to determine the soil water content, and compare TL-BMO with tradition models, such as tangent line (TL) and adaptive waveform interpretation with Gaussian filter (AWIGF); (2) introduce the concept of a WVD and use numerical simulations to analyze the influence of WVDs on soil water redistribution. The TL-BMO is evaluated with TDR waveforms obtained by short-probe sensors in Nicollet, Ida and Hanlon soil samples for a range of water contents to test its accuracy and stability. The root mean squared error of the TDR estimated water content and

the gravimetric water content is  $<2\%$ . In order to compare TL-BMO with the traditional models, waveforms obtained with long- and short-probe TDR sensors in  $\text{CaCl}_2$  solutions for a range of electrical conductivities are used. The results indicate that the TL-BMO model is consistent with the traditional TDR waveform models for some of the waveforms, but the TL-BMO performs better than the traditional models on some challenging waveforms. Thus, TL-BMO can effectively analyze the waveforms from both long- and short-probe TDR sensors. Inspired by the methods used with TL-BMO, the AWIGF model was also revised with a newly designed corner-preserving filter. The performance of the revised AWIGF model on short-probe TDR waveforms was similar to that of the TL-BMO model. One dimensional numerical simulations of soil water redistribution with WVDs are conducted to illustrate the concept and properties of WVDs. Four WVD configurations are discussed to control soil water redistribution. Simulation results indicate that WVDs can increase the local water contents by at least  $0.1 \text{ m}^3 \text{ m}^{-3}$  in a silt loam, but the effects of WVDs varied with deployment depth and separation distance between two adjacent WVDs. Two dimensional numerical simulations are performed to evaluate the effects of two possible designs of the WVDs, i.e., an egg-carton design and a Tyvek design. The soil water content can be altered by  $0.02 \text{ m}^3 \text{ m}^{-3}$  with the WVDs in the numerical examples, and the unsaturated subsurface drainage can be increased due to the soil water accumulation induced by the WVDs. In conclusion, the TL-BMO model can provide stable and accurate analysis of short-probe TDR waveforms, and the TL-BMO model is flexible enough to be used on for both long- and short-probe TDR sensors. The WVD can effectively manipulate soil water redistribution of soil profile water due to the naturally occurring thermal gradients. WVDs can be deployed to cause water accumulation in specific soil layers, and to assist in unsaturated subsurface drainage of soil profile water.

## CHAPTER 1. GENERAL INTRODUCTION

Numerical analysis is used as one approach to perform soil physics research. In soil hydrology, numerical analysis can be used to predict soil water movement under a range of initial and boundary conditions. Soil water content ( $\theta$ ) and soil water movement in upper soil layers have critical importance for several hydrological processes. In this thesis, I will discuss some applications of numerical analysis in soil hydrology studies. This chapter provides a general introduction on the use of time domain reflectometry (TDR) in determining soil water content, and it introduces a coupled heat and water movement model for soil water simulation. The objectives of this thesis are presented. The final section of this chapter details the organization of the thesis.

### **Soil Water Content and Time Domain Reflectometry**

Soil water content is important to many hydrological, environmental and agricultural problems. At the soil surface, water content relates to soil erosion and nutrient leaching (Hatfield et al., 2001). Evaporation and condensation in the upper soil layer, can alter soil water content, and are critical for the soil surface energy balance (Gowda et al., 2013). For the rhizosphere, plant water uptake is related to available soil water content (Jorenush and Sepaskhah, 2003).

Time domain reflectometry (TDR) is a method that can estimate soil water content nondestructively and continuously through the values of soil relative permittivity (Noborio, 2001; Topp et al., 1980; Robinson et al., 2003). TDR measurements estimate the relative permittivity of bulk soil, and determine the soil water content, since soil water is the major contributor for the soil relative permittivity (Robinson et al., 2003; Greco 2006).

A TDR sensor usually consists of two or three transmission probes inserted into the soil. The propagation time of a voltage signal pulse along the probes is related to the relative permittivity of the soil surrounding the probe. The transmission probes are connected to a cable tester through a coaxial cable. When the voltage signal pulse passes the intersection of the coaxial cable and the probes, part of the signal pulse propagates and part of the signal is reflected. The reflection coefficient ( $\rho$ ) is calculated as the ratio of complex amplitude of reflected

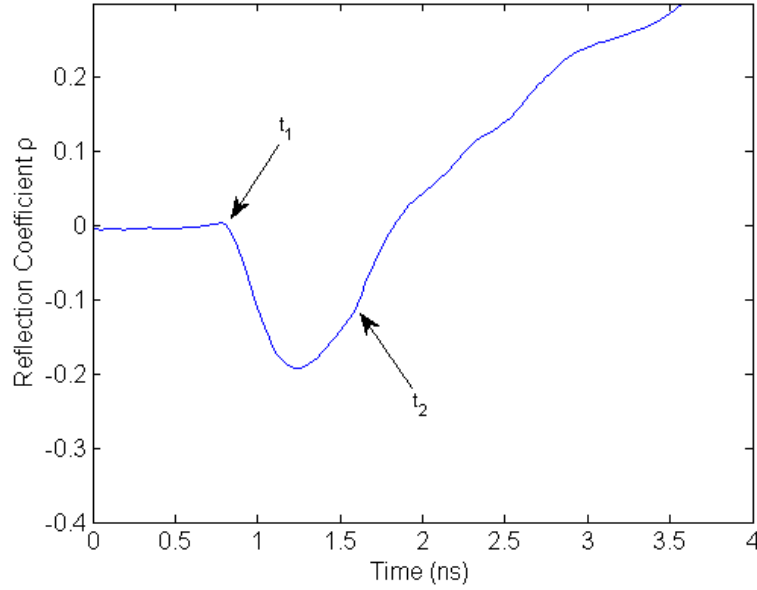


Figure 1.1. A waveform obtained in Ida loam with water content  $\theta_v = 0.138$ . The horizontal axis is time in nanoseconds, and the vertical axis is the reflection coefficient.

signal to the complex input signal. The change of  $\rho$  with respect to time can be plotted as a TDR waveform (Fig. 1.1).  $t_1$  and  $t_2$  are the reflection positions marking the time when the voltage signal pulse passes the intersection, and the soil relative permittivity,  $\epsilon_r$ , and soil water content are determined with Eqs. [1.1] and [1.2] (Topp et al.,1980)

$$\epsilon_r = \left( \frac{c(t_2 - t_1)}{2l} \right)^2 \quad [1.1]$$

and

$$\theta = 4.3 \times 10^{-6} \epsilon_r^3 - 5.5 \times 10^{-4} \epsilon_r^2 + 2.92 \times 10^{-2} \epsilon_r - 5.3 \times 10^{-2} \quad [1.2]$$

where  $c$  is the speed of light and  $l$  is the length of the TDR probes. From the equations, the goal and challenge of a TDR measurement is to accurately determine the propagation time from the TDR waveform.

A TDR sensor is the major factor that influences the position of  $t_1$ , and  $t_1$  is considered to be a constant value for a TDR sensor used for repeated measurements. A common method



to determine  $t_1$  is to calculate the intersection of a tangent line obtained before the uphill portion of the  $t_1$  spike and the base line (the horizontal portion at the left end of the TDR waveforms)  $t_b$ , and add an off-set  $t_c$ , then  $t_1 = t_b + t_c$  (Heimovaara, 1993; Evett, 2000). Calibrations in pure water and in dry air are used to determine  $t_c$  and the effective length of the TDR sensors.

Determining  $t_2$  is the challenging part. First, an accurate determination of  $t_2$  is related to the probe length and to the TDR resolution. In order to make measurements near the surface, relatively short TDR probes are used. For example, the thermo-TDR in Ren et al. (1999) used a short TDR probe design (~40 mm) to enable the small-scale soil water content measurements. The newly designed TDR probes from Campbell Scientific Inc., for example CS640 or CS645, also use short probe lengths (75 mm) to improve the portability of the sensors. Although the TDR200 system (Campbell Scientific Inc. Utah) has good measurement resolution, multiple reflections and their superposition may still reduce the accuracy of  $t_2$  estimation for short probe TDR sensors. TDR waveforms can be also biased in some specific soil conditions, such as in low water content or high salinity situations, which cause the failure of  $t_2$  determination with winTDR (Or et al., 2004) or TACQ (Evett, 2000). Thus, a stable and accurate method to analyze TDR waveforms is needed.

TDR waveform analysis methods based on second order differentiation of the waveform are available, i.e., the adaptive waveform interpretation with Gaussian filtering (AWIGF) by Schwartz et al. (2014) and the second order bounded mean oscillation (BMO) by Wang et al. (2014), respectively.

An adaptive waveform interpretation with Gaussian filtering (AWIGF) algorithm can be used if the TDR probe is relatively long, i.e., 150 to 300 mm (Schwartz et al., 2014). A Gaussian filter is used to pretreat the waveforms, and the second-order derivative is determined from the smoothed waveforms. Under certain conditions, the local maximum of the second-order derivative of the smoothed waveform is used to determine  $t_2$ . However, for short probes under conditions of low media permittivity, AWIGF is subject to errors, and the algorithm may choose the global minimum point as  $t_2$ , which is not suitable for short-probe TDR waveforms (Wang et al., 2014). Thus, an improvement for the use of AWIGF on short probes is needed.

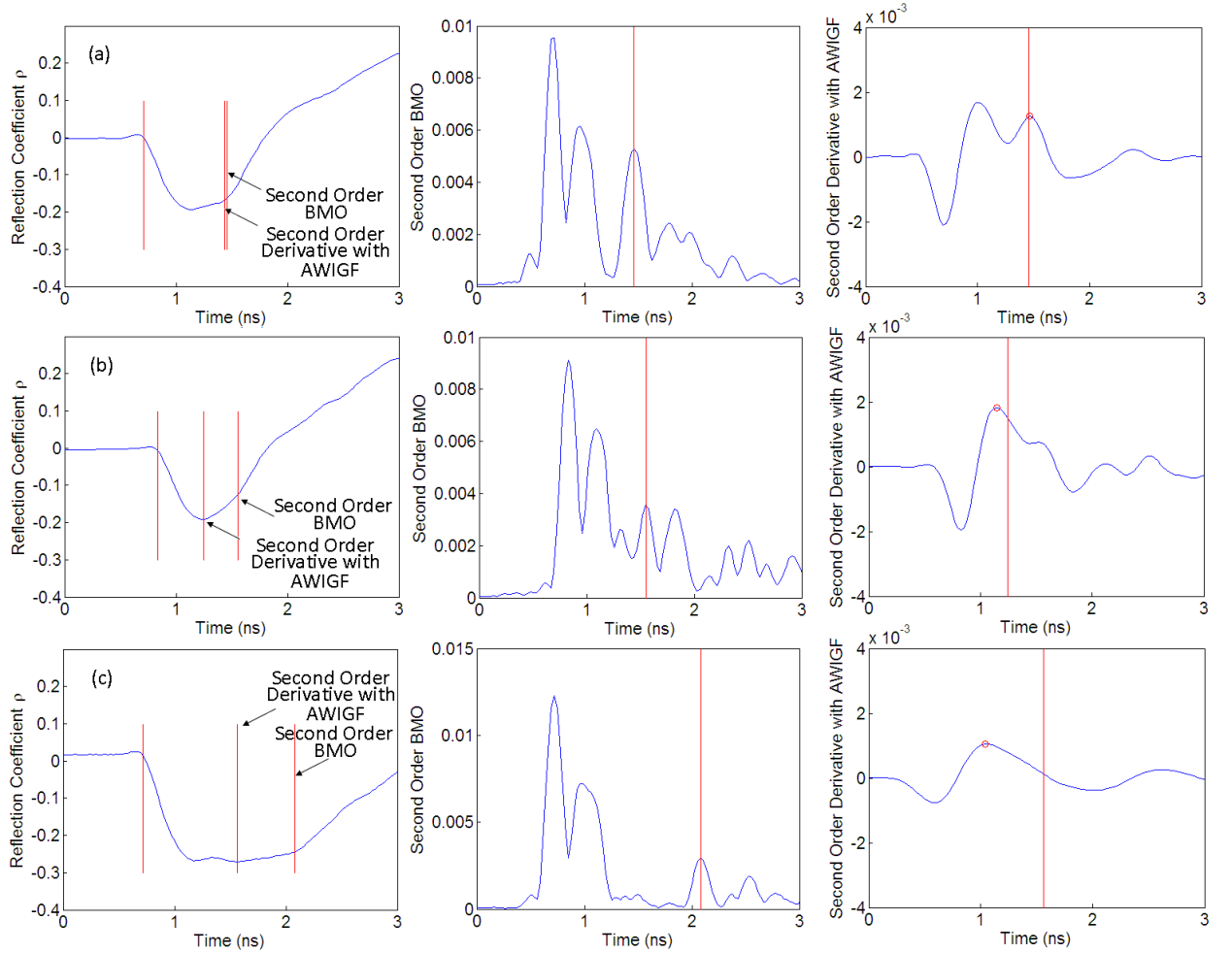


Figure 1.2. A comparison between AWIGF and second order BMO on short probe waveforms.

Second order BMO tends to determine the non-smooth changes of the slope in the TDR waveforms, where the first-order derivative of the waveforms has a jump discontinuity (Wang et al., 2014). Although second-order BMO can provide accurate estimation of  $t_2$ , an automatic implementation of second-order BMO encounters problems when used on short-probe TDR waveforms, because second-order BMO is sensitive to local oscillations in the waveforms (Wang et al., 2014), which generate multiple local maxima near  $t_2$ . Thus, increasing stabilization is needed for the second order BMO method to be useful in an automated model.

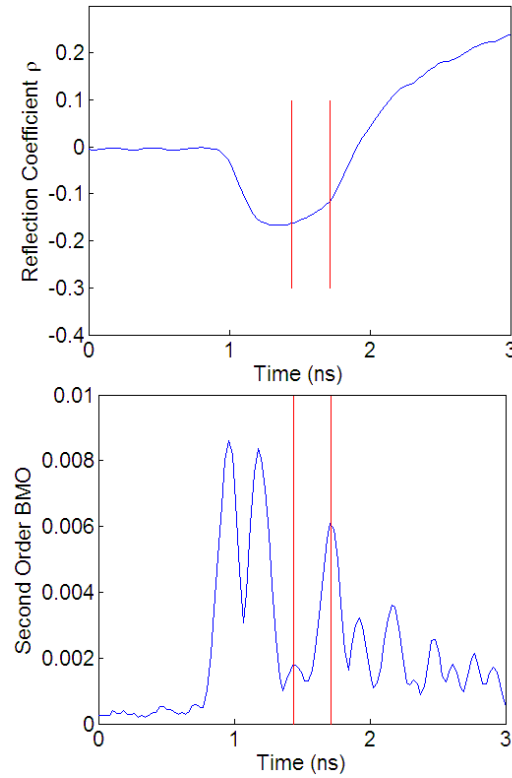


Figure 1.3. The failure of the second order BMO.

A comparison between AWIGF and second order BMO is presented in Fig. 1. 2. The  $t_2$  of short-probe TDR waveforms are determined by AWIGF and second-order BMO. The three TDR waveforms are: (a) waveform from Ida silt loam with water content of  $0.14 \text{ m}^3 \text{ m}^{-3}$ ; (b) waveform from Ida silt loam with water content of  $0.13 \text{ m}^3 \text{ m}^{-3}$ ; (c) waveform from Ida silt loam with water content of  $0.37 \text{ m}^3 \text{ m}^{-3}$ . Each row shows waveform ( $\rho$  vs.  $t$ ), the second-order BMO with corresponding  $t_2$  (red line), and second-order derivative using AWIGF with maximum value point (red circle) and  $t_2$  (red line), respectively. From the analysis, by selecting the correct local maxima, the second order BMO provides better estimations of  $t_2$  than does AWIGF. However, there is potential failure of the second order BMO, which is shown in Fig. 1.3, where a small peak near 1.5 ns confuses the selection of the correct  $t_2$ . The second order BMO is sensitive to such local maxima; thus, it is necessary to design an automatic approach that can eliminate the effects of the small peaks.

### **Soil Heat and Water Movement and Water Vapor Diode**

Soil water content is a static description of soil water, while soil water movement represents a dynamic feature of soil water. Soil water movement can be characterized as having two parts: the liquid water flux and the water vapor flux. Phase changes between liquid water and water vapor may also be considered. Soil water movement is tightly connected to soil heat transfer. Soil temperature difference can be a major driving force for water vapor flux, while liquid water and water vapor flux contribute to the convective heat transfer in soil. Thus, heat and water movement in soil is fully coupled. For agricultural and environmental applications, heat and water movement are important in the study of plant water uptake, soil salinization and its recovery, and soil water evaporation, especially for stage II and stage III evaporation, where evaporation occurs under the soil surface (Ouyang 2002; Federer 1979; Wu et al., 1999). For foundation engineering, the change of soil water content during freezing and thawing cycles can influence soil mechanical properties through changing the soil water content in surface layers (Li, 2000). Heat and water movements are also important in soil-plant-atmosphere continuum models, which relate to ecological and earth climate change studies (Federer 1979; Passioura, 1982).

Coupled heat and water movement experiments and numerical models have been studied for several decades (Parlange, 1998). Numerical simulations can be an efficient way to study coupled heat and water movement in soil. Theory for coupled heat and water movement traces back to the 1950s, when a model was introduced by Philip and de Vries (1957). The basic idea was to use water conservation and energy conservation within an infinitesimal control volume in soil to derive the governing equations system. The theory has been expanded and completed in the following years by a more sophisticated description of the water and energy conservative equations. For example, soil wetting heat and hysteretic phenomena were considered by Milly (1982). Chemical transport equations were added to the coupled heat and water movement model by Nassar and Horton (1989) and Nassar and Horton (1997) to include the role of solutes on heat and water movement. Experiments were used to verify the heat and water movement theories under controlled conditions. For example, Heitman et al. (2008) tested the models for various boundary and initial conditions. Davis et al. (2014) discussed soil wettability and its effects on heat and water movement. The

non-equilibrium of thermal, hydrological, and osmotic potentials in soil can produce uneven distributions of soil water and solutes. Numerical results were used to predict soil heat and water movement under several situations, where experiments were difficult to apply (Antonopoulou, 2006; Li, 2000). Moreover, coupled heat and water movement can be artificially altered, such as the use of a surface plastic cover that can preserve water in arid areas. Numerical simulations were used to evaluate the effect of such methods by estimating water movement and storage (Liu et al., 2016).

In agricultural systems, the most common way to alter heat and water movement in soil is with surface mulching, which can reduce evaporation and sensible heat flow, and increase water content near the soil surface in arid and semi-arid areas. For foundation engineering, subsurface drainage pipes are used to reduce soil profile water content. However, if the soil water content is relatively low, water accumulation and drainage can be limited. If the water vapor in soil can be concentrated in a specific subsurface layer, the soil water content of that layer will be increased to supply plant water uptake or assist drainage. In this thesis, we introduce a water vapor diode that can concentrate water in specific soil layers. The water vapor diode is designed to allow heat fluxes in both vertical directions, but it allows water vapor flux only in one direction. A detailed discussion of the water vapor diode is presented in this thesis.

## **Objectives**

The accuracy of AWIGF and second order BMO waveform analyses for short-probe TDR waveforms need to be further investigated. AWIGF was originally designed for use with long probe TDR sensors, while the second order BMO was designed for short probe TDR sensors. The performance of AWIGF and second order BMO on both long and short probe TDR waveforms have not been fully evaluated. Thus, the objectives for the improved TDR waveform analysis are to (1) design a stable second order BMO model and evaluate it with laboratory and field measurements; (2) evaluate the performance of AWIGF and second order BMO in both long and short TDR probes mathematically and experimentally, and improve the accuracy of AWIGF for short-probe waveforms using an alternative corner preserving filter.

The water vapor diode is a conceptual idea that allows water vapor transfer only in one vertical direction. Using the water vapor diode, it may be possible to accumulate water in specific soil layers. Numerical simulations will be used as a pretest for the water vapor diode concept. The objectives of the water vapor diode study are to (1) introduce the concept and properties of the water vapor diode; (2) use one-dimensional and two-dimensional simulations to give a preliminary numerical evaluation of the ideal water vapor diode, as well as the designs of water vapor diode for different applications.

### **Organization of the Thesis**

A stabilized version of the second order BMO model, i.e., the tangent line/second order BMO model is presented in Chapter 2. Chapter 3 provides an evaluation for the use of AWIGF and second order BMO on long and short TDR probes. An alternative filter is introduced to improve the accuracy of AWIGF for some challenging waveforms. Chapter 4 focuses on the water vapor diode concept, and one-dimensional numerical simulations are used to evaluate the performances of water vapor diode. A further discussion of the water vapor diode is presented in Chapter 5, with two-dimensional simulations with two designs of the water vapor diode. A general conclusion, as well as the future ideas are listed in Chapter 6.

### **References**

- Antonopoulos, V.Z. (2006). "Water movement and heat transfer simulations in a soil under ryegrass." *Biosyst. Eng.* 95:127-138. Doi: <http://dx.doi.org/10.1016/j.biosystemseng.2006.05.008>
- Davis, D.D., R. Horton, J.L. Heitman, T. Ren. (2014). "An experimental study of coupled heat and water transfer in wettable and artificially hydrophobized soils." *Soil Sci. Soc. Am. J.* 78:125-132. doi:10.2136/sssaj2013.05.0182.
- Evelt, S.R. (2000). "The TACQ computer program for automatic time domain reflectometry measurements: II. Waveform interpretation methods." *Trans. ASAE.* 43:1947–1956. doi:10.13031/2013.3100
- Federer, C.A. (1979). "A soil-plant-atmosphere model for transpiration and availability of soil water". *Water Resour. Res.* 15:555-562. DOI: 10.1029/WR015i003p00555.
- Gowda, P., Howell, T.A., Paul, G., Colaizzi, P.D., Marek, T.H., Su, B. and Copeland, K.S. (2013). "Deriving hourly evapotranspiration (ET) rates with SEBS: A lysimetric evaluation." *Vadose Zone J.* 12:1-11. doi: 10.2136/vzj2012.0110

- Greco, R. (2006). "Soil water content inverse profiling from single TDR waveforms." *J. Hydrol.* 317:325–339. DOI: 10.1016/j.jhydrol.2005.05.024
- Hatfield, J.L., Sauer, T.J. and Prueger, J.H. (2001). "Managing soils to achieve greater water use efficiency." *Agron. J.* 93:271–280. doi:10.2134/agronj2001.932271x
- Heimovaara, T.J. (1993). "Design of triple-wire time domain reflectometry probes in practice and theory." *Soil Sci. Soc. Am. J.* 57:1410–1417. doi:10.2136/sssaj1993.03615995005700060003x.
- Heitman, J. L., R. Horton, T. Ren, I. N. Nassar and D. D. Davis. (2008). "A test of coupled soil heat and water transfer prediction under transient boundary temperatures." *Soil Sci. Soc. Am. J.* 72:1197-1207. doi:10.2136/sssaj2007.0234.
- Jorenush, M.H. and Sepaskhah, A.R. (2003). "Modelling capillary rise and soil salinity for shallow saline water table under irrigated and non-irrigated conditions." *Agr. Water Manage.* 61:125–141. DOI: 10.1016/S0378-3774(02)00176-2
- Li, N., B. Chen, F. Chen, X. Xu. (2000). "The coupled heat-moisture-mechanic model of the frozen soil." *Cold Reg. Sci. Technol.* 31: 199–205. DOI: [http://dx.doi.org/10.1016/S0165-232X\(00\)00013-6](http://dx.doi.org/10.1016/S0165-232X(00)00013-6)
- Liu, X., B. He, X. Yi, L. Zhang and F. Han. (2016). "The soil water dynamics and hydraulic processes of crops with plastic film mulching in terraced dryland fields on the Loess Plateau." *Environ. Earth Sci.* 75:809-824. doi:10.1007/s12665-016-5670-x.
- Milly, P.C.D. (1982). "Moisture and heat transport in hysteretic, inhomogeneous porous media: a matric head-based formulation and a numerical model." *Water Resour. Res.* 18:489-498. doi: 10.1029/WR020i008p01087.
- Nassar, I. N. and R. Horton. (1989). "Water transport in unsaturated nonisothermal salty soil: I. Experimental results." *Soil Sci. Soc. Am. J.* 53:1323-1329. doi:10.2136/sssaj1989.03615995005300050004x.
- Noborio, K. (2001). "Measurement of soil water content and electrical conductivity by time domain reflectometry: A review." *Comput. Electron. Agric.* 31:213–237. doi:10.1016/S0168-1699(00)00184-8
- Ouyang, Y. (2002). "Phytoremediation: modeling plant uptake and contaminant transport in the soil–plant–atmosphere continuum." *J. Hydrol.* 266:62-82. DOI: [http://dx.doi.org/10.1016/S0022-1694\(02\)00116-6](http://dx.doi.org/10.1016/S0022-1694(02)00116-6)
- Or, D., Jones, S.B., Van Shaar, J.R., Humphries, S. and Koberstein, L. (2004). *User's guide WinTDR. Version 6.1.* Utah State Univ., Logan. <http://www.usu.edu/soilphysics/wintdr/documentation.cfm>
- Passioura, J. B. (1982). "Water in the soil-plant-atmosphere continuum." *Physiological plant ecology II.* Springer Berlin Heidelberg. 5-33. DOI: 10.1007/978-3-642-68150-9\_2.
- Philip J.R. and D.A. de Vries. (1957). "Moisture movement in porous materials under temperature gradients." *Trans. Am. Geophys. Union.* 38:222–232. doi:10.1029/TR038i002p00222.

- Parlange, M.B., A.T. Cahill, D.R. Nielsen, J.W. Hopmans and O. Wendroth. (1998). "Review of heat and water movement in field soils". *Soil Till. Res.* 47:5-10. DOI: [http://dx.doi.org/10.1016/S0167-1987\(98\)00066-X](http://dx.doi.org/10.1016/S0167-1987(98)00066-X)
- Ren, T., Noborio, K. and Horton, R. (1999). "Measuring soil water content, electrical conductivity and thermal properties with a thermo-time domain reflectometry probe". *Soil Sci. Soc. Am. J.* 63:450–457. doi:10.2136/sssaj1999.03615995006300030005x
- Robinson, D.A., Schaap, M., Jones, S.B., Friedman, S.P. and Gardner. C.M.K. (2003). "Considerations for improving the accuracy of permittivity measurement using time domain reflectometry: Air–water calibration, effects of cable length." *Soil Sci. Soc. Am. J.* 67:62–70. doi:10.2136/sssaj2003.0062
- Schwartz, R.C., Casanova, J.J., Bell, J.M. and Evett, S.R. (2014). "A reevaluation of time domain reflectometry propagation time determination in soils." *Vadose Zone J.* 13:1-13, doi:10.2136/vzj2013.07.0135.
- Topp, G. C., Davis, J. L., and Annan, A. P. (1980). "Electromagnetic determination of soil water content: measurements in coaxial transmission lines." *Water Resour. Res.* 16:574-582. DOI: 10.1029/WR016i003p00574.
- Wang, Z., Kojima, Y., Lu, S., Chen, Y., Horton, R. and Schwartz, R.C. (2014). "Time domain reflectometry waveform analysis with second order bounded mean oscillation." *Soil Sci. Soc. Am. J.* 78:1146-1152. doi:10.2136/sssaj2013.11.0497
- Wu, I., R. Zhang and S. Gui. (1999). "Modeling soil water movement with water uptake by roots." *Plant Soil.* 215:7–17. doi:10.1023/A:1004702807951.



## CHAPTER 2. TANGENT LINE / SECOND ORDER BOUNDED MEAN OSCILLATION WAVEFORM ANALYSIS FOR SHORT TDR PROBE

A paper published in Vadose Zone Journal

Zhuangji Wang<sup>1\*</sup>, Yili Lu<sup>2</sup>, Yuki Kojima<sup>3</sup>, Songtao Lu<sup>4</sup>, Meng Zhang<sup>2</sup>, Yan Chen<sup>2</sup>, Robert Horton<sup>1</sup>

<sup>1</sup> Agronomy Dept., Iowa State University, Ames, IA, USA, 50011

<sup>2</sup> Soil and Water Dept., China Agricultural University, Beijing, China, PRC, 100193

<sup>3</sup> Global Agricultural Sciences Dept., University of Tokyo, Tokyo, Japan, 113-8657

<sup>4</sup> Electrical and Computer Engineering Dept., Iowa State University, Ames, IA, USA, 50011

### Abstract

Tangent line (TL) methods and the second order bounded mean oscillation (BMO) method have been proposed for determining the reflection positions of time domain reflectometry (TDR) waveforms, especially for short-probe TDR sensors. However, the accuracy of TL methods is limited by the multi-reflection effects of the short probe TDR sensor, and an automatic implementation of the second-order BMO is challenging because of the superimposition of the TDR waveforms. In this study, we combined a TL method with second order BMO to develop a tangent line/second order bounded mean oscillation (TL-BMO) method. Laboratory and field data were used to evaluate the TL-BMO method. Separate tests were performed on laboratory data to compare the TL-BMO method with the TL method and the second order BMO method. For selected waveforms, the TL-BMO was more accurate than the TL method (the RMSE of TL-BMO was  $0.0197 \text{ m}^3 \text{ m}^{-3}$ , and the RMSE of TL method was  $0.1071 \text{ m}^3 \text{ m}^{-3}$ ). TL-BMO was able to avoid calculation errors associated with automatic analysis by the second-order BMO (RMSE of TL-BMO automatic analysis was  $0.0199 \text{ m}^3 \text{ m}^{-3}$ , and the RMSE of second-order BMO automatic analysis was  $0.1414 \text{ m}^3 \text{ m}^{-3}$ ). For analyzing field measurements, the TL-BMO method was able to determine soil water contents accurately over a 3-wk long measurement period.

Conclusively, the new TL-BMO method was more accurate than the TL method, and it demonstrated the stability necessary for automatic analysis of short-probe TDR sensors.

### **Abbreviation**

BMO, bounded mean oscillation; TDR, time domain reflectometry; TL, tangent line; TL-BMO, tangent line/second order bounded mean oscillation; T-TDR, thermo-time domain reflectometry

### **Introduction**

Time domain reflectometry (TDR) is an electromagnetic technique used to measure transient volumetric soil water content ( $\theta_v$ ) nondestructively and continuously (Noborio, 2001). The TDR waveforms can be represented as a sequence of reflection coefficient numbers collected during one measurement (Oswald et al., 2003). Time domain reflectometry waveforms are analyzed to estimate the soil relative permittivity ( $\epsilon_r$ ), which is related to  $\theta_v$ , i.e.,  $\theta_v = \theta(\epsilon_r)$  (Topp et al., 1980; Roth et al., 1990). The estimation of  $\epsilon_r$  from TDR waveforms depends on TDR waveform analysis, i.e., determining the first reflection position ( $t_1$ ) and second reflection position ( $t_2$ ).

A thermo-time domain reflectometry (T-TDR) sensor includes a relatively short-probe TDR sensor, with probe length of about 40 mm. The T-TDR sensors, developed by Ren et al. (1999), are used in a wide variety of measurements within the vadose zone (Ochsner et al., 2001; Ren et al., 2003; Ren et al. 2005; Kojima et al., 2014). One advantage of the T-TDR sensor is that it combines the heat pulse technique and TDR technique, providing both thermal properties and  $\theta_v$  measurements at the same location. Another advantage is that the short probe design of a T-TDR sensor makes it suitable for small scale measurements, such as measurements in the soil surface layer. However, short TDR probes can have a drawback. Multi-reflection and superimposition of waves are much more likely to occur within short TDR probes than long TDR probes due to the time resolution of TDR. Multi-reflection and superimposition may bias the shapes of TDR waveforms, particularly for measurements in low-permittivity media, making the global minimum point ( $t_0$ ) appear nearer to  $t_1$  than to  $t_2$ . We say a TDR waveform is biased if the multi-reflection and superposition of multi-reflection occur within the first two-way propagation time period, and a waveform is unbiased if the multiple reflection occurs after the first two-way signal propagation.

Compared with long-probe TDR sensors (>200 mm), short-probe TDR sensor oscillations may occur within a biased TDR waveform near  $t_2$ , and lead to unstable determination of  $t_2$  and  $\theta_v$  in long-term and repeated field measurements. Hence, this drawback of short-probe TDR sensors leads to difficulties in determining  $t_2$ . Consequently, an accurate and stable method is needed for the waveform analysis of short-probe TDR sensors.

The tangent line (TL) method can be used for automatic TDR waveform analysis via software packages, where the reflection positions and  $\varepsilon_r$  can be estimated from the waveforms without additional information (Or et al., 2004; Evett, 2000; Baker and Allmaras 1990). However, the accuracy of the TL method is limited if the waveforms are biased. The results of the TL method are stable in repeated measurements because only  $t_0$  (or an anchor point) and the most rapidly increasing point (the second inflection,  $t_{maxv2}$ ) are considered, while the waveform values near  $t_2$  are neglected. An adaptive waveform interpretation with Gaussian filtering (AWIGF) algorithm can be used for accurate analysis of long-probe TDR sensors (Schwartz et al., 2013). A Gaussian filter is used to pretreat the waveforms, and the second-order derivative is determined for the treated waveforms. The local maxima of the second order derivative are used as  $t_2$ . However, for short probe TDR sensors, AWIGF tends to over-smooth the waveforms in some cases, and the algorithm may choose  $t_0$  as  $t_2$ , which is not suitable for short-probe TDR waveforms (Wang et al., 2014).

Second-order bounded mean oscillation (BMO) can be used to determine  $t_2$  for short-probe TDR sensors, where the second-order BMO operator directly converts the non-smooth points of TDR waveforms to local maxima in the BMO domain. Although second-order BMO can provide accurate estimation of  $t_2$ , an automatic implementation of second order BMO via a software package encounters problems when used on short-probe TDR waveforms, because second-order BMO is sensitive to local oscillations in the waveforms (Wang et al., 2014), which generate multiple local maxima near  $t_2$ . Thus, a manual selection of the local maximum corresponding to  $t_2$  is necessary. If the TDR waveforms are collected with a datalogger, a large number of waveforms can be collected and tedious manual selection is required. There is a need for development of a method for automatic analysis of short probe TDR waveforms. Automatic analysis removes the need for human input of additional information for each waveform.

The TL method and the second order BMO method each have advantages and disadvantages. It may be possible to combine the two methods (Lu et al., 2012). In this study, a new method is developed for analyzing TDR waveforms that leverages the strengths of the TL method and the second-order BMO method to achieve accurate, stable, and automatic analysis results. Thus, this work has three objectives. First, combine the TL method with the second-order BMO method to develop a prediction-correction model, i.e., tangent line/second-order bounded mean oscillation (TL-BMO), to determine  $t_2$ . Second, evaluate the consistency and accuracy of the new TL-BMO automatic analysis using short-probe TDR measurements. In order for the TL-BMO method to be consistent with the TL method and the second-order BMO method, the TDR waveforms must not be too biased, allowing similar results for TL-BMO, TL, and second-order BMO, i.e., all three methods perform equally well. To demonstrate superior accuracy means that the TL-BMO method must provide better estimations of  $t_2$  than the TL method and the second-order BMO method for the biased TDR waveforms. Third, apply the TL-BMO automatic analysis method to field measurements obtained with short TDR probe sensors. Our purpose is to show that the TL-BMO method can analyze repeated measurements to provide appropriate  $\theta_v$  values over several wetting and drying cycles.

## Algorithms

### (i). Second Order Bounded Mean Oscillation

Let the TDR waveform  $u(t)$  be a function of reflection coefficients with respect to time. The second-order BMO is defined as  $Z^2(u, t, r)$  (Wang et al. 2014),

$$Z^2(u, t, r) = \frac{1}{r^2} \int_{-r}^r \left| Z(u, t + \tau, r) - \frac{1}{2r} \int_{-r}^r Z(u, t + \eta, r) d\eta \right| d\tau \quad [2.1]$$

where  $Z(u, t, r)$  can be written based on the approximation of modulus of gradient with a BMO operator (Chen et al., 2013), i.e.,

$$Z(u, t, r) = \frac{1}{r^2} \int_{-r}^r \left| u(x + \tau) - \frac{1}{2r} \int_{-r}^r u(x + \eta) d\eta \right| d\tau \quad [2.2]$$

Equation. [2.1] can be discretized and implemented numerically. The effect of random error on TDR waveforms can also be reduced with Eq. [2.1] (Wang et al., 2014).

The physical assumption of the second-order BMO method is that the reflection positions correspond to the non-smooth points of the TDR waveforms, and the effect of second-order BMO is to transfer the non-smooth points of the TDR waveforms to the local maxima in the second-order BMO curves. Thus, the local maxima in the second-order BMO curves can be used to determine the reflection positions of the TDR waveforms (Fig. 2.1).

**(ii). Tangent Line Method (Flat Line Method)**

Tangent line methods include a flat line method or a slope line method (Or et al., 2004), and a correction using linear regression on a swath of points in the TDR waveforms (Evet, 2000). The flat line method is the simplest version of the TL methods without prior knowledge or predefined parameters. In the flat line method, the first line is tangent to the  $t_0$  of the TDR waveform, and the second line is tangent to  $t_{maxV2}$  after  $t_0$ . The intersection of these two lines is used to determine  $t_2$  (Evet, 2000). An example of the application of the flat line method is shown in Fig. 2.1.

**(iii). Tangent Line/Second Order Bounded Mean Oscillation Method**

The TL-BMO method is a prediction-correction model based on a combination of the flat line method and the second-order BMO method. In the TL-BMO method, a flat line method is used to determine  $t_2^*$  of a TDR waveform, where  $t_2^*$  is an initial prediction of the actual  $t_2$ . If a threshold  $s$  is pre-fixed, a prediction interval can be obtained as  $[t_2^* - s, t_2^* + s]$ . The threshold  $s$  can either be predefined or automatically selected iteratively using second-order BMO results (see the appendix). The second-order BMO is then applied to the same TDR waveform, and the local maximum of the second-order BMO curve within the prediction interval can be selected as  $t_2$ .

Figure 2.1 illustrates the basic idea of the TL-BMO algorithm. The TDR waveform was obtained from a Nicollet sandy clay loam with  $\theta_v$  of  $0.15 \text{ m}^3 \text{ m}^{-3}$ . In the original waveform,  $t_1$  is 0.694 ns (Fig. 2.1-a). Two blue dashed lines represent the flat line method, and the

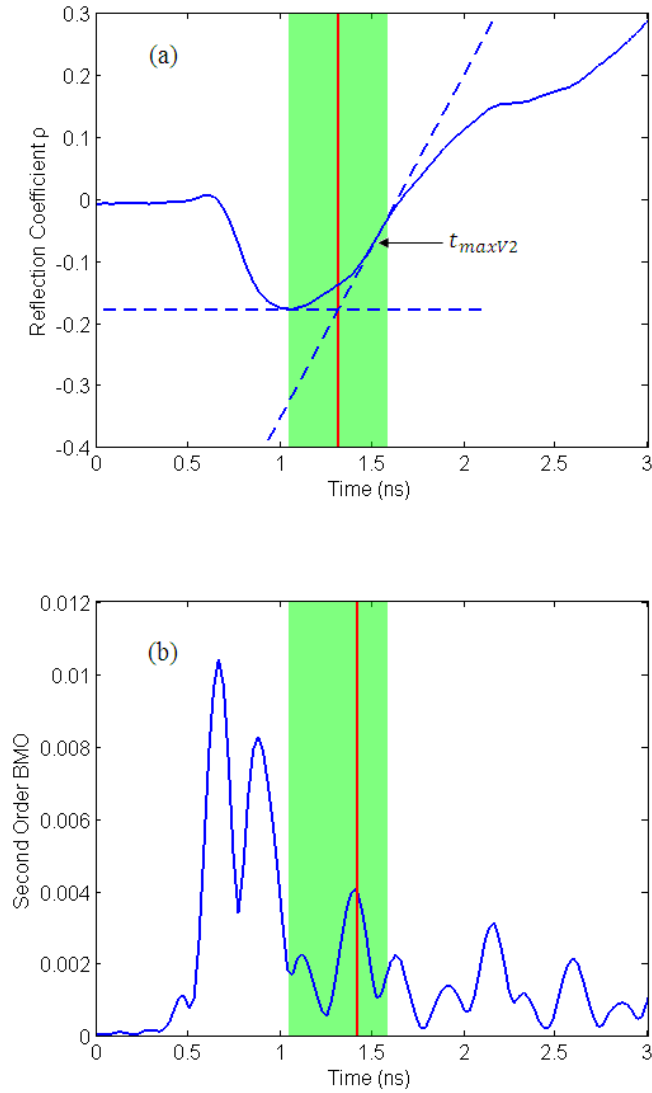


Figure. 2.1 The TDR waveform is obtained from a Nicollet sandy clay loam with water content of  $0.15 \text{ m}^3 \text{ m}^{-3}$ . (a) The TDR waveform and flat line method are shown. The red vertical line corresponds to  $t_2^*$ , and the shaded region shows the prediction interval. (b) The second order BMO curve of the TDR waveform. The shaded region shows the prediction interval, and the vertical line corresponds to  $t_2$ .

intersection corresponds to  $t_2^*$ , which equals 1.428 ns, marked with a red vertical line. The shaded region represents the prediction interval, where the threshold  $s$  is set as 0.267 ns (the time for 10 sampling points). Figure 2.1-b presents the second-order BMO analysis result for

this TDR waveform. The red vertical line represents the local maximum of the second-order BMO curve within the prediction interval, which is selected to be  $t_2$ .

## **Materials and Methods**

### **(i). Laboratory Measurements**

Time domain reflectometry measurements were made with T-TDR sensors having three 40-mm-long and 1.3-mm-diameter stainless steel probes acting as waveguides. The T-TDR sensors were connected to a Tektronix 1502B cable tester (Tektronix Inc.) via a 75- $\Omega$  coaxial cables (RG-187A/U, and the velocity fraction of the propagation in the cable was 0.695). The TDR waveforms were measured on packed samples of three soils, Nicollet sandy clay loam (fine-loamy, mixed, superactive, mesic Aquic Hapludolls), Ida silt loam (fine-silty, mixed, superactive, calcareous, mesic Typic Udorthents), and Hanlon sand (coarse-loamy, mixed, superactive, mesic Cumulic Hapludolls), at several water contents. The bulk densities of packed soil samples were 1.2 g cm<sup>-3</sup>, 1.2 g cm<sup>-3</sup>, and 1.6 g cm<sup>-3</sup>, for the Nicollet sandy clay soil, Ida silt loam, and Hanlon sand, respectively. The TDR waveforms were analyzed with TL-BMO (automatic analysis mode), second-order BMO, and winTDR (with default settings) (Or et al., 2004). The values of  $t_2$  and the calculated relative permittivities were compared among these methods. Gravimetric measurements were used to determine the actual  $\theta_v$  for each soil sample. The TDR-estimated  $\theta_v$  was based on the apparent relative permittivities from TDR waveforms and the Topp et al. (1980) equation. The TDR-estimated  $\theta_v$  and  $\theta_v$  measured directly with the gravimetric method were compared.

### **(ii). Field Measurements**

A field experiment was performed in 2013, from Day of Year (DOY) 242 (30 August) to DOY 268 (25 September). The field site was a bare soil located at the China Agricultural University experimental farm in Beijing, China. The soil texture was sandy loam with 57% sand and 14% clay. The soil organic matter content was 2.11 g kg<sup>-1</sup>. Short-probe T-TDR sensors designed by Liu et al. (2008) were used for this experiment. The T-TDR sensor was made of three stainless steel needles with lengths of 40 mm and diameters of 2 mm. The probe spacing was about 8 mm. The T-TDR probes had pointed needles to eliminate probe deflection when inserting the sensor into soil. Before the field experiment, the apparent length of each T-TDR probe was calibrated in distilled water at constant temperature of 20

°C (Souto et al., 2008). A small trench (10 cm wide and 20 cm deep) was dug in the field, and the T-TDR sensors were installed horizontally at a depth of 12 cm. The trench was backfilled carefully with soil. A TDR100 signal generator and a CR3000 micro-datalogger (Campbell Scientific) were used to obtain the TDR waveforms. The soil was exposed to wetting and drying cycles due to rainfall and evaporation. Weather data were recorded via an automated weather station in the field. After each precipitation event, intact soil samples were collected with 100-cm<sup>3</sup> cylinders from the 10- to 15-cm-depth soil layer. Three replications were obtained, and  $\theta_v$  values were determined by oven drying the samples at 105°C to a constant mass. The TL-BMO method was used to analyze the TDR waveforms. A MATLAB (MathWorks) program for the TL-BMO method is available at <http://soilphysics.agron.iastate.edu/Research/Modeling/BMO.html>.

## Results and Discussion

### (i). Consistency and Accuracy of the TL-BMO Method

Figure 2.2 presents a comparison of the TL-BMO, second-order BMO and TL results. Seven hundred forth-five laboratory waveforms measured with short-probe T-TDR sensors are used in this analysis. Figure 2.2-a shows a comparison of the  $t_2$  values determined with each method. The  $t_2$  estimated with the TL method are used as the reference values, shown as the  $x$  axis, while the  $t_2$  estimated with TL-BMO and second-order BMO are shown as the  $y$  axis. Figure 2.2-b compares the relative permittivity values of the different waveform analysis methods. The  $\epsilon_r$  values calculated with the TL method are considered as the reference values. The majority of  $t_2$  and relative permittivity values follow the 1: 1 lines in the two figures. All three of the methods provide similar results for most of the waveforms (the difference is < 2%). Similar results are obtained for non-biased waveforms. These results indicate that the TL-BMO method is consistent with the second order BMO and TL methods.

For the biased TDR waveforms, TL-BMO, second-order BMO, and TL methods provided different results. Figure 2.3 provides an example of the differences. The TDR waveform was obtained from an Ida silt loam with  $\theta_v$  of 0.138 m<sup>3</sup> m<sup>-3</sup>. The  $t_1$  value was fixed at 0.843 ns. The  $t_2$  values obtained by second-order BMO, TL-BMO, and TL methods were 1.838, 1.575, and 1.495 ns, respectively, and the  $\epsilon_r$  values from the second-order BMO, TL-BMO, and TL methods were 13.885, 7.543, and 5.387, respectively. The difference



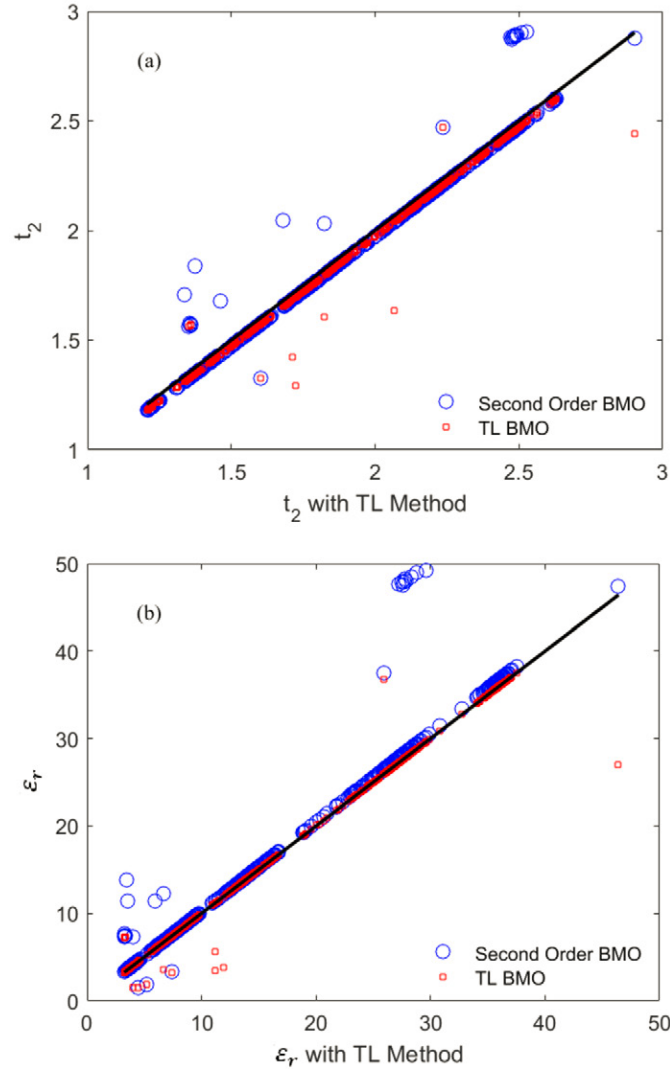


Figure. 2.2 A comparison of the analysis results for TL-BMO, second order BMO, and TL methods. (a) The  $t_2$  is calculated with second order BMO, TL-BMO and TL methods; the TL method calculated  $t_2$  is used as the x-axis. (b) The relative permittivity values calculated with second order BMO, TL-BMO and TL methods; the TL method calculated permittivity values are used as the x-axis.

between TL-BMO and second-order BMO was due to the multi-reflections that occurred in the short-probe TDR sensors, producing oscillations of the waveform near the  $t_2$ . This caused multiple local maxima in the second-order BMO curve. Without having a prediction interval to guide the second-order BMO, it selected the largest local maximum, which was

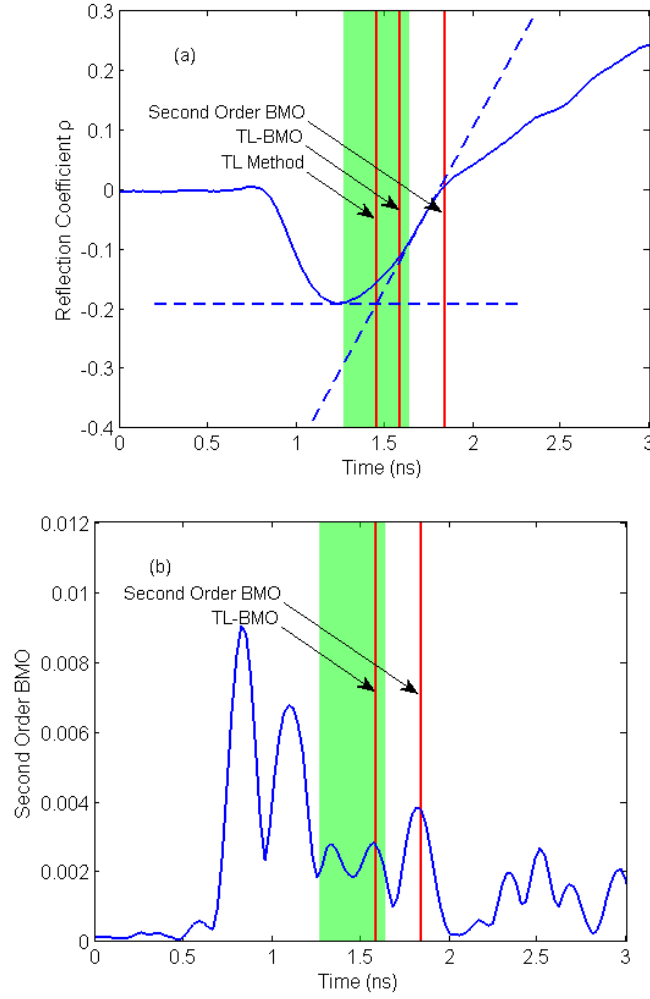


Figure. 2.3 The TDR waveform is obtained from an Ida silt loam with water content of  $0.14 \text{ m}^3 \text{ m}^{-3}$ . (a) The TDR waveform, and the  $t_2$  values from all the three methods. (b) The second order BMO curve of the TDR waveform, and the  $t_2$  values estimated with second order BMO and TL-BMO methods.

not the appropriate local maximum in this example. The multi-reflections also biased the shape of the TDR waveform and caused  $t_0$  to be closer to  $t_1$  than to  $t_2$ . The bias of the waveform caused the TL method to lose local information near  $t_2$  and to only use two points,  $t_0$  and  $t_{\max V2}$ , to estimate  $t_2$ . TL-BMO overcame that difficulty by correcting the  $t_2$  provided by the TL method using second-order BMO information.

Table 2.1. Measured water contents with the gravimetric method ( $\theta_v^*$ ), and calculated relative permittivity ( $\epsilon_r$ ) and Topp et al. (1980) estimated  $\theta_v$  with the TL-BMO and TL methods.

Soil Type	$\epsilon_r$		$\theta_v(\text{m}^3 \text{ m}^{-3})$		$\theta_v^*(\text{m}^3 \text{ m}^{-3})$
	TL-BMO	TL	TL-BMO	TL	
Nicollet	27.009	46.408	0.419	0.547	0.416
Ida	36.736	25.936	0.491	0.409	0.473
Ida	7.585	5.387	0.139	0.089	0.138
Ida	6.954	3.257	0.125	0.036	0.138
Ida	7.215	3.259	0.131	0.036	0.138
Ida	7.295	3.329	0.132	0.038	0.138
Hanlon	5.636	11.211	0.095	0.211	0.076
Hanlon	3.430	11.205	0.041	0.211	0.076
Hanlon	3.795	11.927	0.050	0.224	0.076
Hanlon	3.538	6.718	0.044	0.120	0.076

Table 2.2. Measured water contents with the gravimetric method ( $\theta_v^*$ ), and calculated relative permittivity ( $\epsilon_r$ ) and Topp et al. (1980) estimated  $\theta_v$  with the TL-BMO and second order BMO methods.

Soil Type	$\epsilon_r$		$\theta_v(\text{m}^3 \text{ m}^{-3})$		$\theta_v^*(\text{m}^3 \text{ m}^{-3})$
	Second order BMO	TL-BMO	Second order BMO	TL-BMO	
Nicollet	48.972	28.762	0.563	0.434	0.416
Nicollet	47.945	27.531	0.557	0.424	0.416
Nicollet	48.001	27.878	0.557	0.427	0.416
Nicollet	48.281	27.794	0.559	0.426	0.416
Nicollet	47.903	27.699	0.556	0.425	0.416
Nicollet	47.346	27.009	0.553	0.419	0.416
Nicollet	48.436	28.313	0.560	0.430	0.416
Nicollet	47.680	27.228	0.555	0.421	0.416
Nicollet	47.582	27.626	0.554	0.425	0.416
Nicollet	49.156	29.615	0.564	0.441	0.416
Ida	13.885	7.585	0.258	0.139	0.138
Hanlon	11.437	5.636	0.215	0.095	0.076
Hanlon	11.437	3.430	0.215	0.041	0.076
Hanlon	11.450	3.516	0.216	0.043	0.076
Hanlon	11.375	5.983	0.214	0.103	0.076
Hanlon	12.165	3.795	0.229	0.050	0.076
Hanlon	12.243	3.538	0.230	0.044	0.076

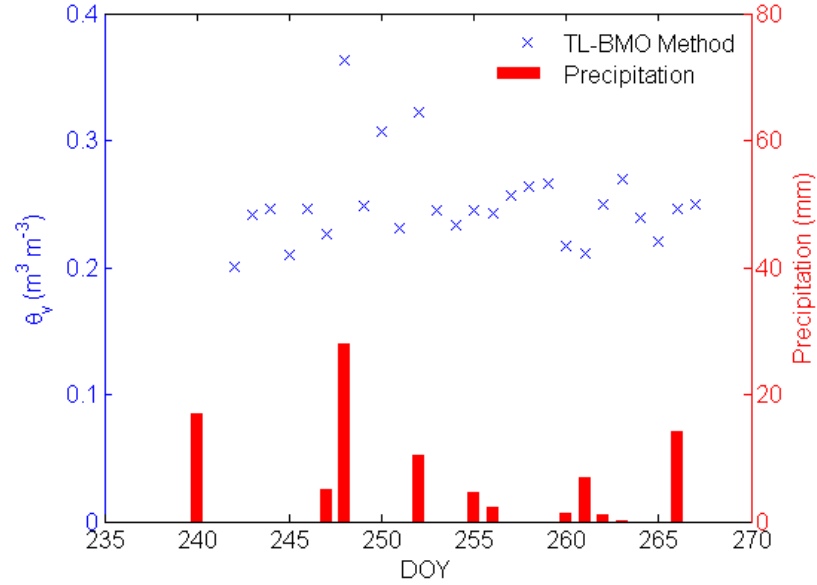


Figure. 2. 4 Topp et al. (1980) estimated  $\theta_v$  from field TDR waveforms as a function of time, day of year (DOY), in 2013. Precipitation events are indicated by the bars.

Tables 2.1 and 2.2 list all of the waveforms for which TL-BMO provides different results than the second-order BMO or TL methods. The  $\theta_v$  values measured with the gravimetric method are also listed. The calculated  $\epsilon_r$  and calculated  $\theta_v$  from TDR waveforms using the Topp et al. (1980) equation are also presented. In Table 2.1, TL-BMO is compared with the TL method, and the root mean square error (RMSE) for the estimated  $\theta_v$  values with TL-BMO is  $0.0197 \text{ m}^3 \text{m}^{-3}$ , while the RMSE for the TL method is  $0.1071 \text{ m}^3 \text{m}^{-3}$ . For Table 2.2, TL-BMO is compared with the second-order BMO method; the RMSE for the second-order BMO is  $0.1414 \text{ m}^3 \text{m}^{-3}$ , and the RMSE for TL-BMO is  $0.0199 \text{ m}^3 \text{m}^{-3}$ . In summary, TL-BMO provided better  $\epsilon_r$  and  $\theta_v$  than the second-order BMO and the TL methods.

## (ii). Application of the TL-BMO Method to Field Measurements

Precipitation and evaporation may lead to rapid changes of the field water content, causing the shapes of TDR waveforms to vary according to the field water content.

Table 2.3. Measured field water contents with the gravimetric method ( $\theta_v^*$ ), and Topp et al. (1980) estimated  $\theta_v$  by TDR with the TL-BMO method on selected days.

DOY	$\theta_v^*(\text{m}^3 \text{ m}^{-3})$	$\theta_v(\text{m}^3 \text{ m}^{-3})$
242	0.211	0.201
246	0.228	0.246
250	0.278	0.307
255	0.268	0.245
263	0.276	0.270
268	0.274	0.229

Figure 2.4 shows the field  $\theta_v$  estimated by TDR with the TL-BMO method. On selected days,  $\theta_v$  was measured gravimetrically, and the measured values along with TDR-estimated  $\theta_v$  are listed in Table 2.3. The RMSE of the TDR estimated  $\theta_v$  is  $0.025 \text{ m}^3 \text{ m}^{-3}$ . The variations of the TDR-estimated  $\theta_v$  in Fig. 2.4 are due to the transient precipitation and evaporation and subsequent soil water redistribution. Most of the TDR-estimated  $\theta_v$  values are similar to the  $\theta_v$  values measured with the gravimetric method. The small sampling size of the T-TDR sensor makes it sensitive to water content changes within a small soil volume; the intact soil samples for gravimetric measurements were not obtained exactly at the same locations as the TDR measurements, so there are small differences in the  $\theta_v$  results between the two methods.

## Summary

Tangent line methods use the intersections of tangent lines to analyze TDR waveforms, and second-order BMO provides local detection of  $t_2$  with a differential operator for short-probe TDR sensors. Tangent line methods and the second-order BMO method each have advantages and disadvantages. The TL method is stable and easy to implement automatically, and the second-order BMO is accurate for TDR waveforms measured with short TDR probes. In this study, the TL method and second-order BMO were combined to produce a new TL-BMO method, which has the advantages of both the TL method and the second-

order BMO method. For TDR waveforms biased with multi-reflection and superimposition, the second-order BMO can be used to determine  $t_2$ . When multiple local maxima occur in the second-order BMO curve, the TL method can give prediction intervals to guide the second-order BMO analysis. The TL-BMO method was validated by comparing its  $\theta_v$  values with  $\theta_v$  determined by the gravimetric method for both laboratory and field measurements. In conclusion, the TL-BMO method was shown to be more accurate than the TL method, and the TL-BMO automatic analysis method provides stable results compared with the second-order BMO automatic analysis method.

### Acknowledgements

This work was supported by the National Science Foundation under Grant 1215864, USDA-NIFA, Multi-State Project 3188, Iowa State University Department of Agronomy, the Hatch Act, and State of Iowa funds.

### References

- Baker, J.M. and R.R. Allmaras. (1990). "System for automating and multiplexing soil moisture measurement by time-domain reflectometry." *Soil Sci. Soc. Am. J.* 54: 1-6.
- Campbell, G.S., C. Calissendorff, and J.H. Williams. (1991). "Probe for measuring soil specific heat using a heat-pulse method." *Soil Sci. Soc. Am. J.* 55:291-293. doi:10.2136/sssaj1991.03615995005500010052x.
- Chen, Y., Z. Wang, and K. Zhang. (2013). "Approximations for modulus of gradients and their applications to neighborhood filters." *Front. Math. China.* 8:761-782. doi:10.1007/s11464-013-0297-7.
- Evelt, S.R. (2000). "The TACQ computer program for automatic time domain reflectometry measurements: II. Waveform interpretation methods." *Transaction of ASAE.* 43:1947-1956. doi:10.13031/2013.3100.
- Kojima, Y., J.L. Heitman, G.N. Flerchinger, T. Ren, R.P. Ewing, and R. Horton. (2014). "Field test and sensitivity analysis of a sensible heat balance method to determine soil ice contents." *Vadose Zone J.* 13(9). doi:10.2136/vzj2014.04.0036.
- Liu, X., T. Ren, and R. Horton. (2008). "Determination of soil bulk density with thermo-time domain reflectometry sensors." *Soil Sci. Soc. Am. J.* 72:1000-1005. doi:10.2136/sssaj2007.0332.
- Lu, S., J. Sun., G. Wang and J. Tian. (2012). "A novel GSC beamformer using a combination of two adaptive filters for smart antenna array." *IEEE Antenn. Wirel. Pr.* 11:377-380. doi: 10.1109/LAWP.2012.2192250

- Noborio, K. (2001). "Measurement of soil water content and electrical conductivity by time domain reflectometry: a review." *Comput. Electron. Agric.* 31:213-237. doi:10.1016/S0168-1699(00)00184-8.
- Ochsner, T. E., R. Horton, and T. Ren. (2001). "Simultaneous Water Content, Air-Filled Porosity, and Bulk Density Measurements with Thermo-Time Domain Reflectometry." *Soil Sci. Soc. Am. J.* 65:1618–1622. doi:10.2136/sssaj2001.1618
- Or, D., S.B. Jones, J.R. Van Shaar, S. Humphries, and L. Koberstein. (2004). "User's guide WinTDR. Version 6.1." Utah State Univ. Logan, UT.
- Oswald, B., H. R. Benedickter, W. Bauchtold, and H. Fluhler. (2003). "Spatially resolved water content profiles from inverted time domain reflectometry signals." *Water Resour. Res.* 39(12), 1357, doi:10.1029/2002WR001890, 2003.
- Ren, T., K. Noborio, and R. Horton. (1999). "Measuring soil water content, electrical conductivity and thermal properties with a thermo-time domain reflectometry probe." *Soil Sci. Soc. Am. J.* 63:450-457. doi:10.2136/sssaj1999.03615995006300030005x.
- Ren, T., T.E. Ochsner, and R. Horton. (2003). "Development of thermo-time domain reflectometry for vadose zone measurements." *Vadose Zone J.* 2: 544-551. doi:10.2136/vzj2003.5440.
- Ren, T., Z. Ju, Y. Gong, and R. Horton. (2005). "Comparing heat-pulse and time domain reflectometry soil water contents from thermo-time domain reflectometry probes." *Vadose Zone J.* 4:1080-1086. doi:10.2136/vzj2004.0139.
- Roth, K., R. Schulin, H. Fluhler, and W. Attinger. (1990). "Calibration of time domain reflectometry for water content measurement using a composite dielectric approach." *Water Resour. Res.* 26:2267–2273. doi: 10.1029/WR026i010p02267.
- Schwartz, R.C., J.J. Casanova, J.M. Bell, and S.R. Evett. (2014). "A reevaluation of time domain reflectometry propagation time determination in soils." *Vadose Zone J.* 13:1-13. doi:10.2136/vzj2013.07.0135.
- Souto, F.J., J. Dafonte, and M. Escariz. (2008). "Design and air–water calibration of a waveguide connector for TDR measurements of soil electric permittivity in stony soils." *Biosyst. Eng.* 101(4): 463-471. doi: 10.1016/j.biosystemseng.2008.09.015.
- Topp, G. C., J. L. Davis, and A. P. Annan. (1980). "Electromagnetic determination of soil water content: measurement in coaxial transmission lines." *Water Resour. Res.* 16:574–582. doi: 10.1029/WR016i003p00574.
- Wang, Z., Y. Kojima, S. Lu, Y. Chen, R. Horton, and R.C. Schwartz . (2014). "Time domain reflectometry waveform analysis with second order bounded mean oscillation." *Soil Sci. Soc. Am. J.* 78:1146-1152. doi:10.2136/sssaj2013.11.0497.

## Appendix

The prediction interval defined in the TL-BMO method has the form  $[t_2^* - s, t_2^* + s]$ , where the threshold  $s$  is pre-defined. However, in order to implement an automatic analysis

of TDR waveforms, the arbitrary value  $s$  should be updated adaptively. We present two strategies for the setting of  $s$ .

Semi-automatic method: the  $t_0$  and  $t_{maxV2}$  values of the TDR waveform are natural boundaries for  $t_2$ . A semi-automatic prediction interval is  $[\max(t_2^* - s, t_0), \min(t_2^* + s, t_{maxV2})]$ , where  $s$  is a predefined threshold. The  $t_0$  and the  $t_{maxV2}$  are enough to determine the prediction interval; however, the threshold  $s$  is necessary for certain challenging waveforms, when the  $t_0$  is much closer to  $t_1$  than to  $t_2$ .

Fully-automatic method: the prediction interval is formed with some small initial guess of  $s_i$ , i.e.,  $[\max(t_2^* - s_i, t_0), \min(t_2^* + s_i, t_{maxV2})]$ . If there is no local maximum of the second order BMO curve within this interval, the threshold  $s_i$  is enlarged by  $\Delta s$ , and a new prediction interval is written as  $[\max(t_2^* - s_i - \Delta s, t_0), \min(t_2^* + s_i + \Delta s, t_{maxV2})]$ . The same procedure is iterated until there is a local maximum of the second order BMO curve within the prediction interval.



### CHAPTER 3. A COMPARISON OF SECOND ORDER DERIVATIVE BASED MODELS FOR TIME DOMAIN REFLECTOMETRY WAVEFORM ANALYSIS

A paper accepted to Vadose Zone Journal

Zhuangji Wang<sup>1\*</sup>, Robert Schwartz<sup>2</sup>, Yuki Kojima<sup>3</sup>, Yan Chen<sup>4</sup>, Robert Horton<sup>1</sup>

1. Dept. of Agronomy, Iowa State University, Ames, IA, 50011

2. Conservation and Production Res. Lab, USDA-ARS, PO Drawer 10, Bushland, TX, 79012.

3. Faculty of Engineering, Gifu University, Gifu, Japan, 501-1193

4. Dept. of Soil and Water Science, China Agricultural University, Beijing, China, 100193.

\*Corresponding author: Zhuangji Wang, [cauwzj@gmail.com](mailto:cauwzj@gmail.com), 515-294-7986.

#### Abstract

Adaptive waveform interpretation with Gaussian filtering (AWIGF) and second-order bounded mean oscillation  $Z^2(u, t, r)$  are time domain reflectometry (TDR) analysis models. AWIGF was originally designed for relatively long-probe (>150 mm) TDR waveforms, while  $Z^2(u, t, r)$  was originally designed for relatively short-probe (<50 mm) TDR waveforms. The performances of AWIGF and  $Z^2(u, t, r)$  on both long and short TDR probes have not been evaluated. The main objective of this study is to evaluate theoretically and experimentally the AWIGF and  $Z^2(u, t, r)$  performances on long and short TDR probes. The evaluations are performed via mathematical analysis, and measurements of long probe and short probe waveforms in  $\text{CaCl}_2$ -solutions with various electrical conductivities (EC), adding Gaussian noise, and testing the stability of  $Z^2(u, t, r)$  and AWIGF. A corner preserving filter (CPF) is proposed to improve the stability of AWIGF on short-probe TDR waveforms. The CPF preserves the second order derivatives of the waveforms, and emphasizes the reflection positions ( $t_2$ ) compared to the original Gaussian filter. Both theoretical and experimental tests illustrate the consistency of  $Z^2(u, t, r)$  and AWIGF. The standard deviations of relative permittivity ( $\epsilon_r$ ) are less than 5% for all noise levels. In conclusion,  $Z^2(u, t, r)$  and AWIGF

can provide stable analysis for long and short probe TDR waveforms. The AWIGF with CPF is capable of stably analyzing challenging short probe TDR waveforms. The original AWIGF exhibits the lowest standard deviation of  $\varepsilon_r$  at a given EC, whereas AWIGF with CPF filter exhibits the lowest bias of  $\varepsilon_r$  across solutions varying in EC.

### **Abbreviation**

AWIGF, adaptive waveform interpretation with Gaussian filtering; BMO, bounded mean oscillation; EC, electrical conductivity; STD, standard deviation; TDR, time domain reflectometry; TL, tangent line; TL-BMO, tangent line/second order bounded mean oscillation; T-TDR, thermo-time domain reflectometry; TV, total variation,

### **Introduction**

Time domain reflectometry (TDR) is an electromagnetic technique used to measure in situ volumetric soil water content ( $\theta_v$ ) (Noborio, 2001). TDR waveforms can be considered as a digital signal of reflection coefficient values collected with respect to time (Oswald et al., 2003). Soil relative permittivity ( $\varepsilon_r$ ), which is related to  $\theta_v$ , i.e.,  $\theta_v = \theta(\varepsilon_r)$ , can be estimated with TDR waveforms (Topp et al., 1980; Roth et al., 1990). Determining the first reflection position ( $t_1$ ) and second reflection position ( $t_2$ ), especially the  $t_2$ , are the basic steps in TDR waveform analysis.

When TDR sensors have probes longer than 150 mm, relatively stable measurements are provided; however, there could be a variation of  $\theta_v$  along the probes. Determining  $\theta_v$  along the probes is complicated (Heimovaara et al., 2004), which limits the usefulness of long-probe TDR for small-scale measurements. Thermo-time domain reflectometry (T-TDR) sensors have relatively short TDR probes (40 to 50 mm). The T-TDR sensors are used in a wide variety of measurements within the vadose zone (Ren et al., 2005; Kojima et al., 2014; Tian et al., 2015). T-TDR sensors measure both thermal and electrical properties simultaneously at the same location. The short-probe design of a T-TDR sensor makes it suitable for small-scale measurements, and  $\theta_v$  usually does not vary much along the short probes. However, as the probe length becomes shorter, there is a possibility for superimposition of multireflections along the transmission line, which may bias the shapes of TDR waveforms, leading to instability in determining  $t_2$  and  $\theta_v$ . Thus, long-probe TDR waveforms and short-probe TDR waveforms must be treated as two different cases, and

different methods have been developed for analyzing long probe waveforms and short probe waveforms, respectively.

The tangent line method can be used for automatic TDR waveform analysis. It uses the  $t_0$  (or an anchor point), and the most rapidly increasing point (the second inflection,  $t_{maxV2}$ ) to determine  $t_2$  (Or et al., 2004; Evett, 2000). The results of the tangent line method are stable in repeated measurements, but the accuracy is limited for the waveforms with biased shapes. An adaptive waveform interpretation with Gaussian filtering (AWIGF) model can be used for accurate analysis of long TDR sensors (Schwartz et al., 2014). In AWIGF, an adaptive Gaussian filter is used to smooth the waveforms, and the second-order derivatives is calculated from smoothed waveforms. The local maxima of the second order derivatives are used as  $t_2$ . The Gaussian filter in AWIGF can be expressed as follows (Schwartz et al., 2014),

$$g(t; \sigma) = \frac{1}{\sqrt{2\pi}\sigma} \exp\left(-\frac{t^2}{2\sigma^2}\right); g'(t, \sigma) = -\frac{t}{\sqrt{2\pi}\sigma^3} \exp\left(-\frac{t^2}{2\sigma^2}\right) \quad [3.1]$$

where  $g'(t, \sigma)$  is the derivative of  $g(t; \sigma)$ , and  $\sigma$  is scaled based on the first-order derivative of the TDR waveforms. The second-order derivative of a TDR waveform  $u(t)$ , i.e.,  $D^2u$ , can be approximated in a convolution form,

$$D^2u = g''(t, \sigma) * u(t) \quad [3.2]$$

However, in some challenging cases, the smoothing effects can be undesirable, especially for short-probe TDR waveforms (Wang et al., 2014), where the magnitude of the local maximum associated with  $t_2$  is reduced. Relatively complicated searching methods are necessary to locate  $t_2$ . Second-order bounded mean oscillation (BMO) was proposed to determine  $t_2$  for short-probe TDR sensors, where the  $Z^2(u, t, r)$  operator directly converts the non-smoothed points of TDR waveforms to local maxima in the BMO domain, which is defined as (Wang et al., 2014),

$$Z^2(u, t, r) = \frac{1}{r^2} \int_{-r}^r \left| Z(u, t + \tau, r) - \frac{1}{2r} \int_{-r}^r Z(u, t + \eta, r) d\eta \right| d\tau \quad [3.3]$$

where  $r$  is the range of the integral,  $\tau$  and  $\eta$  are integration variables, and  $Z(u, t, r)$  can be written based on the approximation of modulus of gradient with a BMO operator (Chen et al., 2013), i.e.,

$$Z(u, t, r) = \frac{1}{r^2} \int_{-r}^r \left| u(t + \tau) - \frac{1}{2r} \int_{-r}^r u(t + \eta) d\eta \right| d\tau \quad [3.4]$$

The local maximum of  $Z^2(u, t, r)$ , corresponding to the  $t_2$ , can be detected with a tangent line/second-order BMO (TL-BMO) method described by Wang et al. (2016).

The AWIGF model was reported as an effective automatic analysis method for relatively long-probe TDR waveforms (Schwartz et al., 2014), while the  $Z^2(u, t, r)$  operator was reported as being effective on analyzing waveforms from relatively short-probe TDR sensors (Wang et al., 2014; Wang et al., 2016; Lu et al., 2016). Both of the methods are based on the second-order differentiation of TDR waveforms. Thus, AWIGF and  $Z^2(u, t, r)$  should perform similarly for both long and short TDR probes, aside from some differences induced by certain detailed implementations mentioned in Wang et al. (2014). It is meaningful to further evaluate theoretically and experimentally the AWIGF and  $Z^2(u, t, r)$  for both long-probe and short-probe TDR waveforms. Although AWIGF has been shown to be useful for many waveforms, it can over-smooth the signal for some challenging short-probe TDR waveforms. In order to improve the stability of AWIGF for short-probe TDR waveform analysis, an alternative corner persevering filter (CPF) was designed for testing.

The objectives of this study are to (i) evaluate theoretically and experimentally the performance of AWIFG and  $Z^2(u, t, r)$  for long- and short-probe TDR waveforms, including mathematical analysis and laboratory performance tests; and (ii) design a CPF and test its performance on challenging short-probe TDR waveforms. The second-order BMO and TL-BMO are two implementations of the  $Z^2(u, t, r)$  operator. Throughout the theoretical study, the  $Z^2(u, t, r)$  operator will be studied directly; while TL-BMO will be used in the laboratory tests.

## Theory

### (i) Theoretical Evaluation the Two Methods

$Z^2(u, t, r)$  and AWIFG are each constructed by applying second-order differential operators to the original waveforms, and then choosing the appropriate local maxima of the differentiated waveforms as  $t_2$ . Thus,  $Z^2(u, t, r)$  should be consistent with AWIFG, i.e., both of the methods should provide similar intermediate quantities and final results. We will show that  $Z^2(u, t, r)$  can approximate the absolute value of the second-order differentiation of  $u$  asymptotically.

Given a TDR waveform  $u(t)$ ,  $Z(u, t, r)$  can approximate the absolute value of the first-order derivative of a TDR waveform  $u$  (Wang et al., 2014), i.e.,

$$\lim_{r \rightarrow 0^+} Z(u, t, r) = |Du| \quad [3.5]$$

By using this result twice and the chain rule, we obtain

$$\lim_{r \rightarrow 0^+} Z^2(u, t, r) = |D|Du|| = \left| \frac{d|Du|}{d(Du)} D(Du) \right| = \left| \frac{D^2u}{\text{sgn}(Du)} \right| = |D^2u|.$$

Then we can approximate the second-order differentiation as,

$$\lim_{r \rightarrow 0^+} Z^2(u, t, r) = |D^2u|. \quad [3.6]$$

Since AWIGF determines the approximated second-order derivative of  $u$  (Schwartz et al., 2014), both  $Z^2(u, t, r)$  and AWIGF are methods based on the second order differentiation of the original TDR waveforms, i.e., they are consistent with each other.

In order to complete the comparison between AWIFG and  $Z^2(u, t, r)$ , it is necessary to evaluate their smoothing effects. This comparison can be done by using a local BMO quantity, which we can define as,

$$BMO_{p,loc}(u, t, r) = \frac{1}{2r} \left( \int_{-r}^r \left| u(t + \tau) - \frac{1}{2r} \int_{-r}^r u(t + \eta) d\eta \right|^p d\tau \right)^{\frac{1}{p}}. \quad [3.7]$$

The local BMO varies with respect to time and  $p$  indicates that  $p$ -norm was used in this operator. If  $p = 2$ ,  $BMO_{p,loc}(u, t, r)$  is actually the local standard deviation of the TDR waveforms. Here we choose  $p = 1$ , to be consistent with the definition of  $Z^2(u, t, r)$ .

It is expected that the smoothed TDR waveforms should have lower local BMO than the original waveforms. Consider a filter  $s(t)$  that satisfies  $0 < s(t) \leq 1$  and  $\int_0^T s(t)dt = 1$ . The smoothed TDR waveform can be expressed as the convolution form  $\hat{u} = s * u$ , and  $T$  is the total measuring time for one TDR waveform. We can express the local BMO of the smoothed waveform using Young's inequality as

$$\begin{aligned} BMO_{1,loc}(\hat{u}, t, r) &= \frac{1}{2r} \int_{-r}^r \left| s * u(t+x) - \frac{1}{2r} \int_{-r}^r s * u(t+y)dy \right| dx \\ &= \frac{1}{2r} \int_{-r}^r \left| s * \left( u(t+x) - \frac{1}{2r} \int_{-r}^r u(t+y)dy \right) \right| dx \\ &\leq \frac{1}{2r} \int_{-r}^r |s(t)|dt \int_{-r}^r \left| u(t+x) - \frac{1}{2r} \int_{-r}^r u(t+y)dy \right| dx \\ &\leq \frac{1}{2r} \int_{-r}^r \left| u(t+x) - \frac{1}{2r} \int_{-r}^r u(t+y)dy \right| dx = BMO_{1,loc}(u, t, r). \end{aligned}$$

Using this result, we can rewrite AWIGF and  $Z^2(u, t, r)$  into convolution forms with different filters.  $Z^2(u, t, r)$  contains a moving average filter,  $s_Z(t)$ , which averages the quantity  $\left| u(t+x) - \frac{1}{2r} \int_{-r}^r u(t+y)dy \right|$  with respect to time. For a signal  $f(t)$ , the smoothing effect of  $s_Z(t)$  can be characterized as  $s_Z * f = \int_{-r}^r s_Z(\tau - t)f(t)d\tau = \frac{1}{2r} \int_{-r}^r f(t)dt$ , where  $r$  is the radius of the filter. The Gaussian filter in AWIGF can be denoted as  $s_G(t)$ . To control the loss of information, the radius of the filter is related to  $\sigma$ . We compare the  $Z^2(u, t, r)$  and AWIGF on their effect of reducing the local BMO.

The  $Z(u, t, r)$  operator can be expressed into a convolution form with filter  $s_Z(t)$ ,

$$Z(u, t, r) = \frac{2}{r} s_Z * |(\delta - s_Z) * u|$$

where  $\delta$  is the Dirac function, and the convolution is based on the interval  $[x - r, x + r]$ .

Then, we have

$$Z^2(u, x, r) = \frac{4}{r^2} s_Z * |s_Z * |(\delta - s_Z) * u| - s_Z * s_Z * |(\delta - s_Z) * u||.$$

Then we apply the local BMO on both sides as follows

$$\begin{aligned} BMO_{1,loc}(Z^2(u, x, r)) &\leq BMO_{1,loc}\left(\frac{4}{r^2} s_Z * s_Z * ||(\delta - s_Z) * u| - s_Z * |(\delta - s_Z) * u||\right) \\ &\leq \frac{4}{r^2} BMO_{1,loc}(|(\delta - s_Z) * u| - s_Z * |(\delta - s_Z) * u|) \\ &\leq \frac{4}{r^2} \left[ \int_{-r}^r |s_Z + \delta| dt \right] BMO_{1,loc}(|(\delta - s_Z) * u|) \\ &\leq \frac{4}{r^2} \left[ \int_{-r}^r (s_Z + \delta) dt \right]^2 BMO_{1,loc}(u) \leq \frac{16}{r^2} BMO_{1,loc}(u). \end{aligned}$$

The leading coefficient is of the order,  $O(r^{-2})$ . In AWIGF, we use  $D(t)$  to denote the differential operator, such as the central difference, to obtain

$$BMO_{1,loc}(s_G * D^2 * u) \leq BMO_{1,loc}(D^2 * u) \leq \frac{4}{r^2} BMO_{1,loc}(u)$$

where  $s_G$  is the Gaussian filter defined in AWIGF. It is shown that the local BMO can be reduced with AWIGF as well as  $Z^2(u, x, r)$  of the same order,  $O(r^{-2})$ .

Through the analysis, the consistency and smoothing effects of  $Z^2(u, x, r)$  and AWIGF are presented. The mathematical process provides sufficient evidence that  $Z^2(u, x, r)$  and AWIGF can perform equivalently for short- and long-probe TDR waveforms. The evaluation of the performance of  $Z^2(u, x, r)$  and AWIGF on long- and short-probe TDR waveforms will be provided below.

## (ii) Design of a Corner-Preserving Filter

Although AWIGF and  $Z^2(u, t, r)$  are equivalent, they have some differences embedded in their implementations. Both AWIFG and  $Z^2(u, t, r)$  can work equivalently well for a large number of short-probe waveforms (Wang et al., 2014). However, for some challenging waveforms, the smoothing strength of the Gaussian filter in AWIGF must be carefully controlled because AWIGF can reduce the magnitude of the local maxima in the second-order derivative associated with  $t_2$ , such that the determination of  $t_2$  becomes difficult (Wang et al., 2014). Because AWIGF constructs the filter based on the maximum of the first-order derivative of the TDR waveform  $u$ , the Gaussian filter in AWIGF can preserve the steeply increasing or decreasing portion of  $u$  associated with a large first-order derivative.

However,  $t_2$  is associated with the second-order derivative. Thus, the Gaussian filter in AWIGF does not have the property to directly preserve  $t_2$  during the smoothing. There exists, therefore, an opportunity to improve AWIGF's performance by designing a new CPF based on the second-order derivative of the TDR waveforms.

To construct the CPF, we first introduce a general framework of waveform smoothing based on the total variation (TV) model. Let  $u^\diamond$  be the target smoothed waveform. The TV filter can be expressed as an optimization problem (Chambolle and Lions, 1997),

$$\min_{u^\diamond} \|u - u^\diamond\|_2^2 + R(u^\diamond) \quad [3.8]$$

where  $\|u - u^\diamond\|_2^2$  is a fidelity term to control the over-smoothing problem that measures the distance between the original waveform  $u$  and the target waveform  $u^\diamond$ , and  $R(u^\diamond)$  is a penalty term to control the noise. There are several possible choices for  $R(u^\diamond)$ . A commonly used  $R(u^\diamond)$  is the Rudin-Osher-Fatmi model, where  $R(u^\diamond) = \|Du^\diamond\|_1$  (Rudin et al., 1992). The 1-norm of the first-order derivative can reduce the local variation on the flat parts of the waveform, and causes "stair effects" on the edges of the waveform. Because a TDR waveform filter should preserve the second-order derivative of  $u$  near  $t_2$ , we need to choose  $R(u^\diamond)$  related to the second-order derivative of the waveform. Chan et al. (2000) reported several constructions of  $R(u^\diamond)$  based on second-order derivatives of a waveform, and Lysaker et al. (2003) and You et al. (2000) studied the minimization problem in Eq. [3.8] by formulizing it into a fourth-order partial differential equation.

Suppose  $R(u^\diamond) = \int_T f(D^2 u^\diamond) dt$ , and  $f$  is a positive increasing function (You et al., 2000). The Euler-Lagrange equation derived from the minimization problem is

$$D^2 \left[ f'(|D^2 u^\diamond|) \frac{D^2 u^\diamond}{|D^2 u^\diamond|} \right] = 0. \quad [3.9]$$

If we define the diffusion coefficient as a positive monotonically decreasing function,  $c(s) = \frac{f'(s)}{s}$ , then Eq. [3.9] can be written as

$$D^2 [c(|D^2 u^\diamond|) D^2 u^\diamond] = 0,$$



[3.10]

or in a gradient descent form,

$$\frac{\partial u^\diamond}{\partial t} = -D^2[c(|D^2 u^\diamond|)D^2 u^\diamond].$$

[3.11]

We choose the diffusive coefficient as  $c(s) = \frac{1}{1+s^2/k^2}$ , and  $k$  is a tuning parameter in this model that balances the preserving and smoothing effect of the filter for TDR waveforms dependent on the shape of TDR waveforms. Equation. [3.11] is our proposed CPF. The convergent results of gradient descent iteration based on Eq. [3.11] will be the solution of Eq. [3.10]. There is no specific method to determine  $k$ ; however, it is possible to find an appropriate  $k$  value that is suitable for a range of TDR waveforms. For example, we will use  $k = 0.1$  in this study, and the  $k$  should be set as a variable in other implementations.

The mathematical formulation of our proposed CPF corresponds to a fourth-order partial differential equation. We note that based on the Perona-Malik model, the Gaussian filter in AWIGF asymptotically approaches to a second-order partial differential equation (Perona and Malik, 1990). Thus, the CPF described here is essentially different from the Gaussian filter published in the AWIGF algorithm (Schwartz et al., 2014).

The CPF can be implemented by numerically solving Eq. [3.11] with the measured waveform as the initial condition. The solution of Eq. [3.11] will be the waveform after smoothing. The CPF can be embedded in the AWIGF model easily by replacing the original Gaussian filter. In the following experimental tests, an AWIGF model with a CPF was designed based on the Schwartz et al. (2014) algorithm. We use AWIGF(Gaussian) to denote the original AWIGF model; and we use AWIGF(CPF) to denote the AWIGF model with the new CPF.

## Materials and Methods

Firstly, TDR waveforms measured in soil are used as examples to test the CPF filter. Since the CPF is designed to improve the AWIGF performance on short-probe TDR sensors, we only provide short probe waveform examples. Secondly, measurements on various  $\text{CaCl}_2$ -solutions were used to evaluate the performance of AWIGF and  $Z^2(u, x, r)$  on both long- and short-probe TDR sensors.

### (i) Soil Measurements

A total of 180 waveforms were collected with short-probe TDR sensors in a Nicollet soil sample (a fine-loamy, mixed, superactive, mesic Aquic Hapludoll, with bulk density  $1.2 \text{ g cm}^{-3}$ ) and an Ida soil sample (a fine-silty, mixed, superactive, calcareous, mesic Typic Udorthent, with bulk density  $1.2 \text{ g cm}^{-3}$ ) with a range of water content. The short probe TDR sensors had three 40-mm-long and 1.3-mm-diameter stainless steel cylinders with 6-mm spacing. The probes were connected via 75- $\Omega$  coaxial cables (RG-187A/U) to a Tektronix 1502B cable tester (Tektronix, Beaverton, OR). The 75- $\Omega$  cables have less high-frequency loss than 50- $\Omega$  cables and consequently are helpful for better waveform interpretation. The TDR sensors were calibrated in air and water, and the calibration was applied independently to the experiments of this study. The actual gravimetric water content of each soil sample was measured with the oven-dry method, and converted to  $\theta_v$  as reference values to compare with the TDR results.

### (ii) Calcium Chloride Solutions Measurements

The electrical conductivity (EC) values created by the  $\text{CaCl}_2$ -solutions were equal to 0, 1, 3, 5  $\text{dS m}^{-1}$ , monitored with an EC meter (HI 4522, Hanna Instruments, Italy). Electrical conductivity is one of the factors that can affect the shape of TDR waveforms but have little or no influence on the permittivity for small changes in concentration of dilute ( $< 30 \text{ mM}$ ) ionic solutions. Thus, analyzing the long and short probe TDR waveforms with a range of EC values permits the evaluation the efficiency and stability of the algorithms. The long probe TDR sensor had three 150-mm-long, 3-mm-diameter stainless steel rods with 30-mm spacing, and the short-probe TDR sensor are of the same design as described above. The probes were connected via 75- $\Omega$  coaxial cables (RG-187A/U) to a Tektronix 1502B cable tester. The TDR sensors were calibrated in air and water. In  $\text{CaCl}_2$ -solutions measurements,  $t_1 = 1.86 \text{ ns}$  for the short-probe sensor, and for the long-probe sensor,  $t_1 = 1.48 \text{ ns}$ . Gaussian noise of different magnitudes, i.e., 0.1, 0.2, 0.5, 1, 2 and 5% (i.e., 0.0864, 0.1720, 0.4238, 0.8279, 1.5836, 3.5218 dB), were added to the waveforms. The waveforms for all of the noise levels were analyzed with AWIGF(Gaussian), AWIGF(CPF) and TL-BMO to evaluate the consistency and stability of the three models.

The stability among the three models can be characterized based on the  $\varepsilon_r$  values. The variation of  $\varepsilon_r$  values can be evaluated using the standard deviation (SD) for different EC values and different noise levels. The smaller the SD value of the results, the more stable the numerical model. The formulas of SD are shown as follows: Let  $\varepsilon_{r(i,j,k)}$  be the  $\varepsilon_r$  value of each measurement, where  $i = 1,2,3,4$  stands for 4 EC values,  $j = 1,2, \dots, 6$  represents the 6 noise levels, and  $k = 1,2, \dots, n$  is the index for replications. Then the SD of  $\varepsilon_r$  with specific EC and noise level is defined as

$$SD(\varepsilon_r) = \sqrt{\frac{1}{n} \sum_k \left( \varepsilon_{r(i,j,k)} - \frac{1}{n} \sum_k \varepsilon_{r(i,j,k)} \right)^2} \quad [3.12]$$

In order to compare the stability of the three models across different ECs and noise levels, we further define the SD for a given EC (under all noise levels) as

$$SD(\varepsilon_r) = \sqrt{\frac{1}{6} \sum_j \left[ \frac{1}{n} \sum_k \left( \varepsilon_{r(i,j,k)} - \frac{1}{n} \sum_k \varepsilon_{r(i,j,k)} \right)^2 \right]} \quad [3.13]$$

and the SD for a given noise level (averaged over all EC values)

$$SD(\varepsilon_r) = \sqrt{\frac{1}{4} \sum_i \left[ \frac{1}{n} \sum_k \left( \varepsilon_{r(i,j,k)} - \frac{1}{n} \sum_k \varepsilon_{r(i,j,k)} \right)^2 \right]} \quad [3.14]$$

## Results and Discussion

We first provide examples to demonstrate the effectiveness of the CPF filter for AWIGF model in short probe TDR waveforms. Then we present the analyzed results of  $\text{CaCl}_2$ -solutions waveforms for both long and short TDR sensors, from which we discuss the stability of AWIGF(Gaussian), AWIGF(CPF) and TL-BMO models.

### (i) Results of Soil Measurements

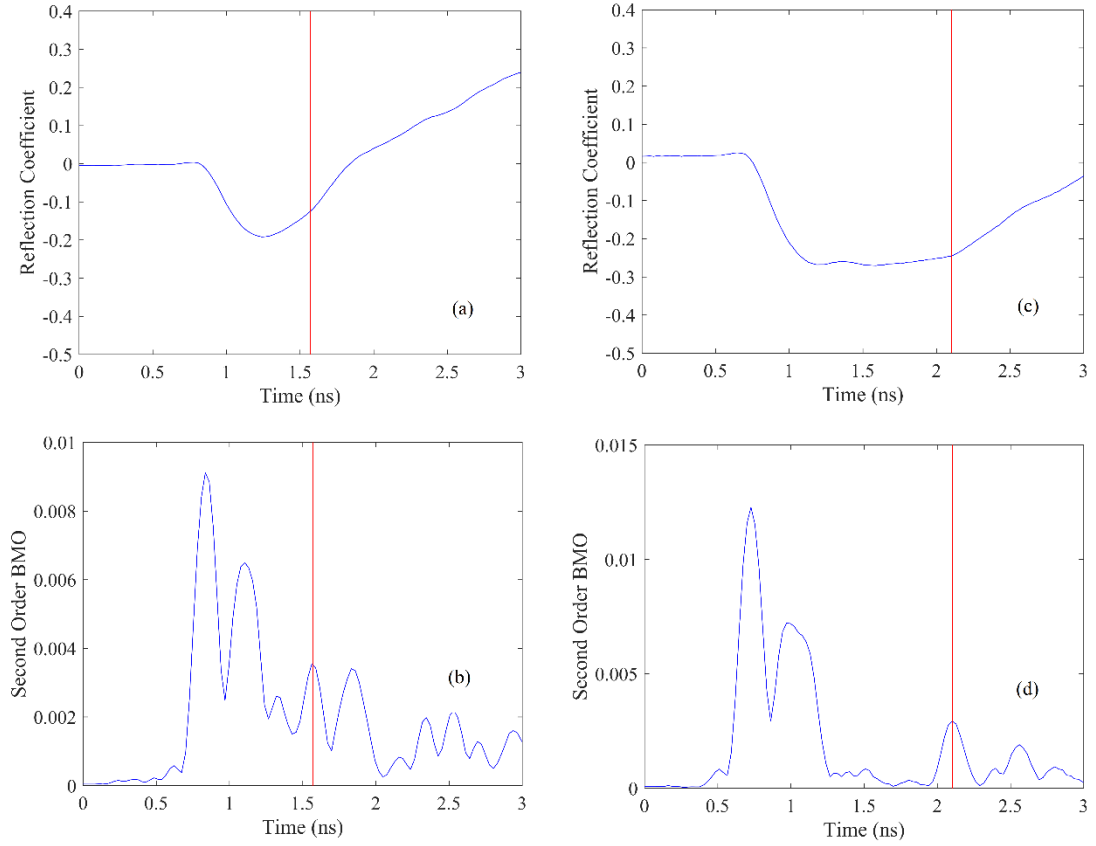


Fig. 3.1 Waveform of Ida silt loam with a water content of  $0.13 \text{ m}^3 \text{ m}^{-3}$  (a), and the  $Z^2(u, x, r)$  result (b); waveform of Ida silt loam with a water content of  $0.37 \text{ m}^3 \text{ m}^{-3}$  (c), and the  $Z^2(u, x, r)$  result (d). The vertical red lines mark the  $t_2$  value for the waveforms.

Two example waveforms are presented in Fig. 3.1, associated with the  $Z^2(u, x, r)$  results. Figure 3.1-a and b present the original waveform and results of  $Z^2(u, x, r)$  via TL-BMO for an Ida soil with water content of  $0.13 \text{ m}^3 \text{ m}^{-3}$ . We set the  $t_1 = 0.834 \text{ ns}$ . The  $t_2$  calculated with  $Z^2(u, x, r)$  via TL-BMO is  $1.554 \text{ ns}$ . Figure 3.1-c shows the waveform from Ida soil with water content of  $0.37 \text{ m}^3 \text{ m}^{-3}$ , and the  $Z^2(u, x, r)$  result is shown in Fig.3.1-d. The  $t_1 = 0.720 \text{ ns}$ . The  $t_2$  from TL-BMO is  $2.081 \text{ ns}$ . These waveforms are considered to be challenging because they are measured with short-probe TDR sensors; the  $t_0$  locates near  $t_1$  and  $t_2$  due to multiple reflections and superposition of reflections along the short probe; and the oscillations in the second-order derivatives of the waveform caused by noise have

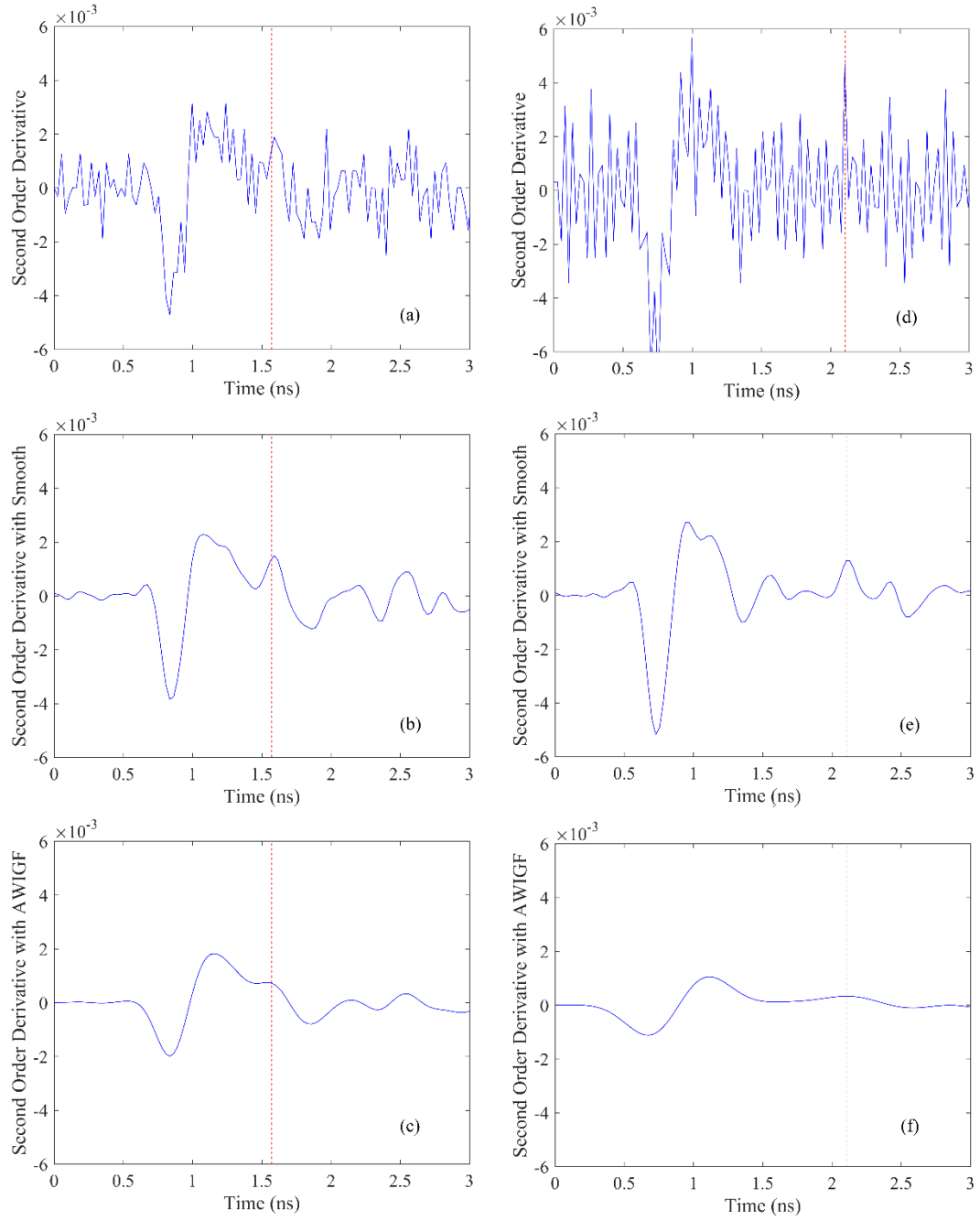


Fig. 3.2 The second order derivative without filtering (a), with CPF filter (b) and with AWIGF Gaussian filter (c) of the waveform in Fig. 1-a; the second order derivative without filtering (d), with CPF filter (e) and with AWIGF Gaussian filter (f) of the waveform in Fig. 1-b. The vertical red dash lines mark the reference  $t_2$  values calculated with TL-BMO.

magnitudes as large as the magnitude of local maxima associated with  $t_2$  (also refer to Fig. 2-a and d). The CPF should adaptively remove the oscillations caused by the noise.

Figure 3.2 presents the smoothing effects of the proposed CPF filter and the Gaussian filter in AWIGF on the second order derivatives of the TDR waveforms. The red dashed lines represent the reference  $t_2$  values determined with TL-BMO. Figure 3.2-a and d present the second order derivatives calculated from the original TDR waveforms corresponding to Fig.3.1-a, and c. Figure 3.2-b and e show the second-order derivatives determined from the TDR waveforms smoothed by the CPF filter. We set  $k = 0.1$  in the diffusion coefficient. The oscillations of the second order derivative caused by the noise are eliminated, and the local maxima near the reference  $t_2$  are preserved. Figure 3.2-c and f show the second-order derivatives determined from the TDR waveforms smoothed by AWIGF(Gaussian). The local maxima associated with  $t_2$  are reduced significantly as well as the oscillations caused by the noise. Although there are still peaks in the second-order derivative curves near the reference  $t_2$ , the peaks are weak, and a sensitive algorithm is required to detect  $t_2$ . Based on the example, the CPF, which is not as strong as the Gaussian filter in AWIGF, can smooth the TDR waveforms while preserving the second order differentiation of the waveforms adaptively near  $t_2$ . Thus, the CPF can be used as an alternative filter in AWIGF model.

Figure 3.3 presents a comparison of  $\varepsilon_r$  and  $\theta_v$  values estimated from short-probe waveforms by AWIGF(Gaussian), AWIGF(CPF) and TL-BMO models with known reference water contents values (Fig.3.3-a and b), with the error bar representing the  $\pm 1$  standard deviations. The figure also shows the magnitude of the second order derivatives values of each waveform corresponding to  $t_2$  (Fig.3.3-c). The  $\varepsilon_r$  values in Fig.3.3-a are converted to  $\theta_v$  using the Topp et al. (1980) equation. The mean TDR water content values for all three models match the reference  $\theta_v$  well, and the mean  $\theta_v$  with all three models are similar. In Fig.3.3-c, the data are sorted based on a decreasing order of the second-order derivative values at  $t_2$  with AWIGF(Gaussian). In general, both AWIGF(Gaussian) and AWIGF(CPF) provide  $\theta_v$  values similar to the TL-BMO values. However, the magnitudes of the second-order derivative at  $t_2$  with AWIGF(CPF) are larger than the magnitudes with

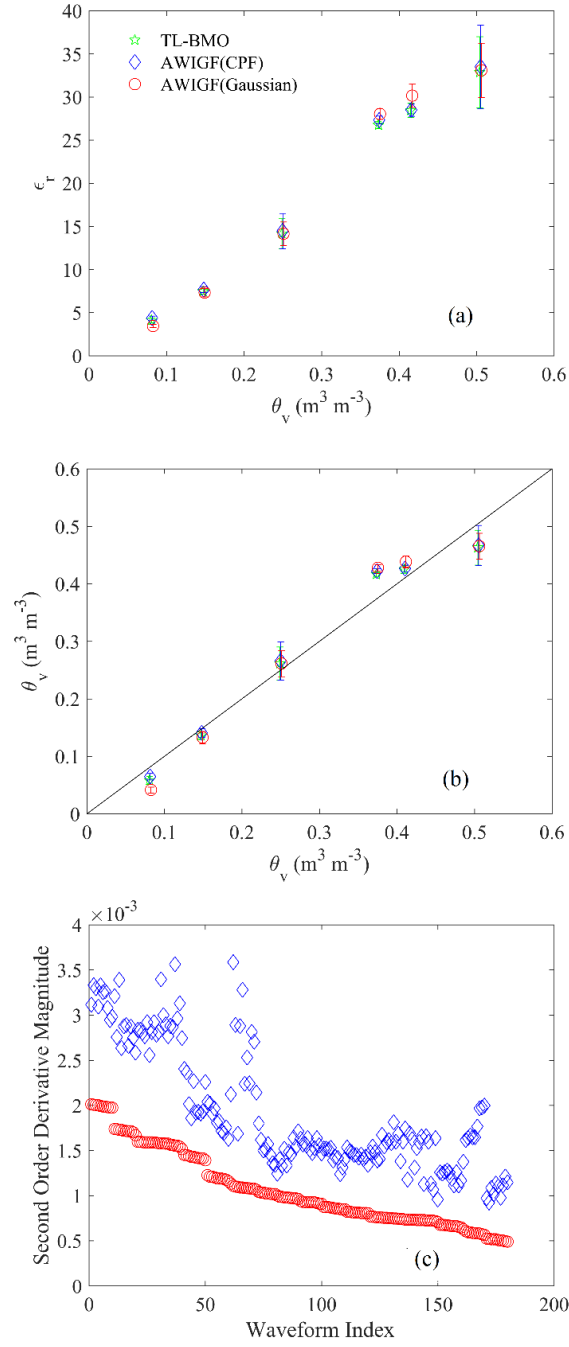


Fig. 3.3 A comparison of short probe waveform analysis mean  $\epsilon_r$ ,  $\theta_v$  results among TL-BMO, AWIGF(Gaussian), and AWIGF(CPF) with respect to  $\theta_v$  estimated from oven dry method (a) and (b), with error bars represent  $\pm 1$  standard deviations; and the magnitude of second order derivative values of each waveform corresponding to  $t_2$  (c).

AWIGF(Gaussian). For these waveforms, the larger magnitude second order derivative values with AWIGF(CPF) make the identification of  $t_2$  easier than with AWIGF(Gaussian). Thus, filtering with the CPF may make it possible to improve the effectiveness of AWIGF for some challenging waveforms measured with short probe TDR sensors.

## (ii) Results of Calcium Chloride Solutions Measurements

Figure 3.4 shows example waveforms for  $\text{CaCl}_2$ -solutions of 0, 1, 3, and 5  $\text{dS m}^{-1}$  with long and short TDR sensors. Propagation times should remain similar for waveforms in all of the different  $\text{CaCl}_2$ -solutions; however, the shapes of the waveforms vary due to the different EC values. The attenuation on the curvature of the TDR waveforms after  $t_0$  in solutions with relatively large ECs induces difficulties in determining the  $t_2$  and  $\epsilon_r$  values.

Figure 3.5 shows the means and SD values of  $\epsilon_r$  for long and short TDR sensors, respectively, for different EC and noise levels. The changes of the mean values with respect to different ECs and noise levels are shown, and the shaded areas represent SDs of given EC or noise level, following the definitions in Eqs. [3.13] and [3.14]. The mean values of TL-BMO and AWIGF(CPF) are consistent with each other, i.e., they are of the same scale and comparable. The SD values increase with respect to the noise level, but remain similar across different EC values. In general, the SD of  $\epsilon_r$  is  $< 5\%$ . The results indicate the stability of TL-BMO and AWIGF(CPF) models under noise with a variety of magnitudes.

Generally, the AWIGF(Gaussian) results have smaller SD values than the TL-BMO and AWIGF(CPF) models. A reason for the smaller SD values is that the Gaussian filter in AWIGF(Gaussian) is stronger than the CPF (see Fig. 3.2). A stronger filter tends to capture the large-scale characters of the waveforms. In these laboratory tests, for the same EC and noise level, the waveforms have similar large-scale pattern, and that causes individual waveforms to become similar after the smoothing procedure with the Gaussian filter. However, TL-BMO and AWIGF(CPF) smoothing is based on the local properties of individual waveforms, i.e., their filters are adaptive to different waveforms and different portions within one waveform, and they especially preserve the neighborhoods near  $t_2$ . That maintains the variations of  $t_2$  and  $\epsilon_r$  within each noise level and EC value, and relatively large SD values are obtained. On the other hand, a strong Gaussian filter may reduce the importance of the local-scale information near  $t_2$ . With the relatively large attenuation of



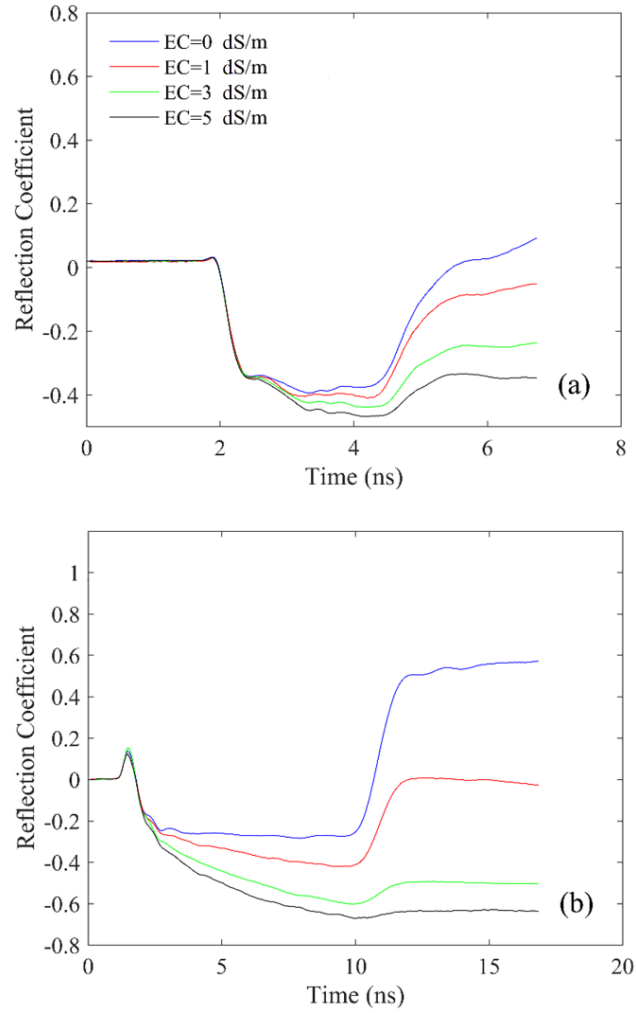


Fig. 3.4 (a) Waveforms measured with a short probe TDR sensor in  $\text{CaCl}_2$ -solutions with four different EC values; (b) waveforms measured with a long probe TDR sensor in  $\text{CaCl}_2$ -solutions with four different EC values.

curvature near  $t_2$  in large EC solutions and the relatively large noise occurring near  $t_2$ , the positions of  $t_2$  may be shifted. Thus, the SD of  $\epsilon_r$  of AWIGF(Gaussian) across different EC values and different noise levels are larger than those for TL-BMO and AWIFG(CPF), especially for short-probe sensors. These results show that the advantage of an adaptive filter is that it maintains the local-scale information, and localizes  $t_2$  for individual waveforms; while the AWIFG(Gaussian) captures the large-scale information and performs stably for a sequence of similar waveforms, even with outliers.

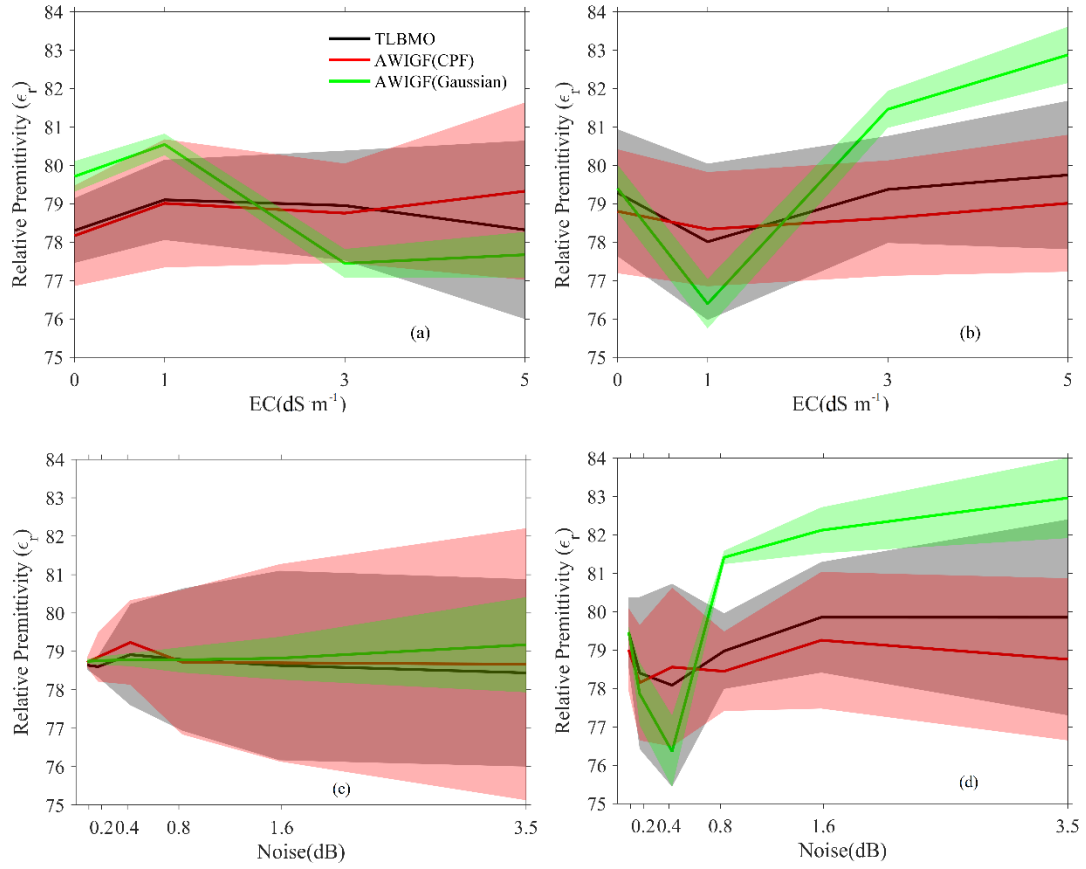


Fig. 3.5 (a) The change of mean  $\epsilon_r$  of long probe waveforms with respect to EC; (b) The change of mean  $\epsilon_r$  of short probe waveforms with respect to EC, the shaded areas in (a) and (b) show the STD for specific EC values; (c) The change of mean  $\epsilon_r$  of long probe waveforms with respect to noise level; (d) The change of mean  $\epsilon_r$  of short probe waveforms with respect to noise level, the shaded areas in (c) and (d) show the STD for specific noise level.

In general, for long probe TDR waveforms, all three models provide consistent and stable results. For short-probe TDR waveforms, AWIGF(Gaussian) shows relatively large bias of the results for different ECs. However, equipped with a CPF, the performance of AWIGF is improved, and AWIGF(CPF) produces results similar to TL-BMO. Thus, to achieve a smaller variance for long-probe TDR waveform analysis, AWIGF(Gaussian) is

recommended, while for short probe waveforms, AWIGF(CPF) and TLBMO are recommended due to the small bias of the results compared to AWIGF(Gaussian).

## Conclusions

The  $Z^2(u, t, r)$  method uses the local maximum of second-order BMO operator to determine  $t_2$ , while AWIGF calculates  $t_2$  based on second-order derivative curves of smoothed TDR waveforms. In this study, we performed both theoretical and experimental analyses of AWIGF and  $Z^2(u, t, r)$ , and an alternative CPF was tested with AWIGF. Laboratory experiments verified the effectiveness and stability of the  $Z^2(u, t, r)$  implemented by TL-BMO, AWIGF(CPF) and AWIGF(Gaussian) models on long-probe TDR waveforms, but for short-probe TDR waveforms, the performance of AWIGF(Gaussian) could be improved by using the alternative CPF filter. Then,  $Z^2(u, t, r)$  and AWIGF could be used effectively and accurately on both long-probe and short-probe TDR waveforms.

Theoretical analysis and measurements in  $\text{CaCl}_2$ -solutions are the bases of this study. Values of  $t_2$  and  $\varepsilon_r$  for soil at a range of water contents are presented as examples. Further investigation of the models on a variety of soil types is recommended. Moreover, based on the advantages of the three models, it may be possible in the future to design a generalized and heuristic model to fit any TDR waveform (Takahashi et al., 2010; Lu et al., 2012(a) ; Lu et al., 2012(b); Lu et al., 2014).

## Acknowledgements

This work was supported by the National Science Foundation under Grant 1623806, USDA-NIFA, Multi-State Project 3188, Iowa State University Department of Agronomy, the Hatch Act, and State of Iowa funds.

## References

- Chambolle, A, and P.L. Lions. (1997). "Image recovery via total variation minimization and related problems." *Numer. Math.* 76:167–188. doi: 10.1007/s002110050258.
- Chan, T., A. Marquina, and P. Mulet. (2000). "High-order total variation-based image restoration." *SIAM J. Sci. Comput.* 22:503–516. doi: 10.1137/S1064827598344169.
- Chen, Y., Z. Wang, and K. Zhang. (2013). "Approximations for modulus of gradients and their applications to neighborhood filters." *Front. Math. China* 8:761–782 . doi:10.1007/s11464-013-0297-7.

- Evett, S.R. (2000). "The TACQ computer program for automatic time domain reflectometry measurements: II. Waveform interpretation methods." *Trans. ASAE* 43:1947–1956 . doi:10.13031/2013.3100.
- Heimovaara, T.J., J.A. Huisman, J.A. Vrugt, and W. Bouten. (2004). "Obtaining the Spatial Distribution of Water Content along a TDR Probe Using the SCEM-UA Bayesian Inverse Modeling Scheme." *Vadose Zone J.* 3: 1128–1145. doi:10.2136/vzj2004.1128.
- Kojima, Y., J.L. Heitman, G.N. Flerchinger, T. Ren, R.P. Ewing, and R. Horton. (2014). "Field test and sensitivity analysis of a sensible heat balance method to determine soil ice contents." *Vadose Zone J.* 13(9). doi:10.2136/vzj2014.04.0036.
- Lu, S., D. Liu, and J. Sun. (2012(a)). "A distributed adaptive GSC beamformer over coordinated antenna arrays network for interference mitigation." *2012 Conference Record of the Forty Sixth Asilomar Conference on Signals, Systems and Computers (ASILOMAR)*, Pacific Grove, CA. 237-242.
- Lu, S., J. Sun, G. Wang and J. Tian. (2012(b)). "A Novel GSC Beamformer Using a Combination of Two Adaptive Filters for Smart Antenna Array." *IEEE Antenn. Wirel. Pr.* 11: 377-380.
- Lu, S., V.H. Nascimento, J. Sun, and Z. Wang. (2014). "Sparsity-aware adaptive link combination approach over distributed networks." *Electronic Letters.* 50: 1285 – 1287. doi: 10.1049/el.2014.2036
- Lu, Y., X. Liu, J. Heitman, R. Horton, and T. Ren. (2016). "Determining Soil Bulk Density with Thermo-Time Domain Reflectometry: A Thermal Conductivity-Based Approach." *Soil Sci. Soc. Am. J.* 80:48-54. doi:10.2136/sssaj2015.08.0315
- Lysaker, M., A. Lundervold, and X. Tai. (2003). "Noise removal using fourth-order partial differential equation with applications to medical magnetic resonance images in space and time." *IEEE Trans. Image Process.* 12:1579-1590. doi:10.1109/TIP.2003.819229.
- Noborio, K. (2001). "Measurement of soil water content and electrical conductivity by time domain reflectometry: A review." *Comput. Electron. Agric.* 31:213–237. doi:10.1016/S0168-1699(00)00184-8.
- Or, D., S.B. Jones, J.R. Van Shaar, S. Humphries, and L. Koberstein. (2004). "User's guide WinTDR. Version 6.1." Utah State Univ., Logan.
- Oswald, B., H.R. Benedickter, W. Bauchtold, and H. Flühler. (2003). "Spatially resolved water content profiles from inverted time domain reflectometry signals." *Water Resour. Res.* 39:1357. doi:10.1029/2002WR001890.
- Perona, P., and J. Malik. (1990). "Scale space and edge detection using anisotropic diffusion." *IEEE Trans. Pattern Anal. Mach. Intell.* 12:629–639. doi:10.1109/34.56205.
- Ren, T., Z. Ju, Y. Gong, and R. Horton. (2005). "Comparing heat-pulse and time domain reflectometry soil water contents from thermotime domain reflectometry probes." *Vadose Zone J.* 4:1080–1086. doi:10.2136/vzj2004.0139.

- Roth, K., R. Schulin, H. Flühler, and W. Attinger. (1990). "Calibration of time domain reflectometry for water content measurement using a composite dielectric approach." *Water Resour. Res.* 26:2267–2273. doi:10.1029/WR026i010p02267.
- Rudin L.I, S. Osher, and E. Fatemi. (1992). "Nonlinear total variation based noise removal algorithms." *Physica D.* 60:259-268. doi:10.1016/0167-2789(92)90242-F.
- Schwartz, R.C., J.J. Casanova, J.M. Bell, and S.R. Evett. (2014). "A reevaluation of time domain reflectometry propagation time determination in soils." *Vadose Zone J.* 13(1). doi:10.2136/vzj2013.07.0135.
- Takahashi, N., I. Yamada, and A. Sayed. (2010). "Diffusion least-mean squares with adaptive combiners: formulation and performance analysis." *IEEE Trans. Signal Process.* 58: 4795–4810. doi: 10.1109/TSP.2010.2051429
- Tian, Z., J. Heitman, R. Horton, and T. Ren. (2015). "Determining Soil Ice Contents during Freezing and Thawing with Thermo-Time Domain Reflectometry." *Vadose Zone J.* 14. doi:10.2136/vzj2014.12.0179.
- Topp, G.C., J.L. Davis, and A.P. Annan. (1980). "Electromagnetic determination of soil water content: Measurement in coaxial transmission lines." *Water Resour. Res.* 16:574–582. doi:10.1029/WR016i003p00574.
- Wang, Z., Y. Kojima, S. Lu, Y. Chen, R. Horton, and R.C. Schwartz. (2014). "Time domain reflectometry waveform analysis with second order bounded mean oscillation." *Soil Sci. Soc. Am. J.* 78:1146–1152. doi:10.2136/sssaj2013.11.0497.
- Wang, Z, Y. Lu, Y. Kojima, S. Lu, M. Zhang, Y. Chen, and R. Horton. (2016). "Tangent line/second-order bounded mean oscillation waveform analysis for short TDR probe." *Vadose Zone J.* 15(1). doi: 10.2136/vzj2015.04.0054.
- You, Y.L., M. Kaveh. (2000). "Fourth-order partial differential equations for noise removal." *IEEE Trans. Image Process.* 9: 1723-1730. doi: 10.1109/83.869184.

## CHAPTER 4. THE IMPACT OF WATER VAPOR DIODES ON SOIL WATER REDISTRIBUTION

A paper accepted to Journal of Hydrology

Zhuangji Wang<sup>1\*</sup>, Mark Ankeny<sup>2</sup>, Robert Horton<sup>1</sup>

1. Dept. of Agronomy, Iowa State University, Ames, IA, 50011

2. 156 Harvest Run Drive, Idaho Falls, Idaho 83404

Corresponding author: Zhuangji Wang, [cauwzj@gmail.com](mailto:cauwzj@gmail.com).

### Abstract

Diurnal soil temperature fluctuations are the prime cause for subsurface water vapor fluxes. In arid and semi-arid areas, water vapor flux is the dominant means of soil water redistribution. The directions of water vapor flux shift from upward to downward diurnally following the variations of the soil thermal gradient. A water vapor diode (WVD), acting as a check valve, allows water vapor flux in one direction but heat flux in both directions. By installing a subsurface WVD, it is possible to impose direction-controlled vapor fluxes, and WVDs can be used to accumulate or remove water in particular soil layers. The egg carton shape, with pores situated at selected peaks and valleys, is a possible design for WVDs. In this study, we provide the concept and the properties of the ideal WVDs, and we discuss four WVD configurations to control soil water redistribution. Numerical simulation is used to evaluate the impacts of the ideal WVDs. The results indicate that WVDs can increase local water contents by at least  $0.1 \text{ m}^3 \text{ m}^{-3}$  in a silt loam. For a fixed initial water and thermal condition, the effect of WVDs is related to the deployment depth and distance between two consecutive WVDs. WVDs can be used to manipulate soil water redistribution and accumulate water at specific depths to support plant growth. The numerical simulation results indicate the potential effectiveness of the ideal WVDs, and field tests should be performed to determine their function under specific soil conditions.

## **Abbreviation**

WVD: Water Vapor Diode,

## **Introduction**

Temperature driven water vapor flow is an important means for soil water redistribution in arid and semi-arid regions. The diurnal change of soil surface temperature leads to a diurnal variation in soil thermal gradients, inducing water vapor flux with intensity and direction following the soil heat flux (Jackson et al., 1973; Jackson et al., 1974). Typically, during the daytime, the soil surface temperature is warmer than the subsurface temperature, and the downward soil thermal gradient induces downward soil heat flux and water vapor transfer. During the night time, the soil surface temperature is colder than the subsurface temperature, causing an upward thermal gradient, and leading to upward soil heat flux and water vapor transfer.

Coupled heat and water transfer models can be used to simulate heat and water vapor transfer in soil. Inspired by Philip and de Vries (1957), many such models include water transfer in both liquid and vapor phases under soil water potential gradients and temperature gradients. Expanding the theory of Philip and de Vries (1957), Milly (1982) accounts for the heat of wetting and soil water hysteresis, and Nassar and Horton (1989b) include osmotic effects on coupled heat and water transfer. Coupled heat and water transfer models can simulate liquid and vapor movement for a wide range of soil types, water contents and temperatures under a variety of initial and boundary conditions (Cary, 1966; Nassar and Horton, 1989a; Nassar and Horton, 1997; Heitman et al., 2008; Bittelli et al., 2008).

In arid and semi-arid areas where soil temperature gradients are relatively large and soil water contents are relatively small, subsurface evaporation can be a major means of water loss from the root zone. There are several ways to reduce soil water evaporation. For example, surface mulching can conserve water and provide a favorable environment for plant growth (Wills et al., 1962; Sui et al., 1992; Li, 2003; Liu et al., 2016; Yang et al., 2012). Another example is the solar still, which is designed to be a water accumulating method (Jackson and van Bavel, 1965; Badran et al., 2005). A solar still consists of a hemispherical hole in the soil, covered with a transparent plastic film. The edge of the plastic film is fixed at the soil surface, and the center of the film is positioned to be lower than the surrounding soil

surface. During the daytime, the water that evaporates from the soil-air interface within the hole, under the plastic film, is trapped in the hole by the plastic cover. The water vapor will condense on the plastic film, while the heat can propagate through the film. The condensed water will flow to the lowest point of the film. A cup placed beneath the lowest point can be used to collect the liquid water that drops off the film. The solar still is considered as a desert survival technique, and in general it is useful for several days. Based on the solar still physics of separating heat and water movement with a plastic covering, it may be possible to design a simple method, i.e., a soil water vapor diode (WVD), that can accumulate water at a specific subsurface layer within the root zone.

A WVD is an extension of the solar still technique. The term ‘diode’ was borrowed from electronics to describe a device designed to rectify alternating current to direct current flow. An ideal WVD is designed to allow water vapor fluxes in one direction, but block water vapor fluxes in the opposite direction. Liquid water flow is not allowed across the WVD in both directions. However, conductive heat flux can propagate in both directions. Thus, the ideal WVD is designed as a semi-transmissible layer for water vapor, and this can lead to water accumulation on one side of a WVD. WVDs can be buried in soil to continuously accumulate water in a specific soil layer over long time periods. An egg carton shape, with pores situated at selected peaks and valleys, is a possible design for a WVD. Moreover, multiple WVDs can be combined to influence soil water distribution in various ways. WVDs provide a simple way to accumulate water in desert soils to support plant growth and biological activity.

The objectives of this study are to (1) provide a definition and properties of ideal WVDs and use the egg carton design as an example to discuss the potential influences of WVDs on soil water redistribution; (2) use a one-dimensional coupled heat and water transfer model to numerically simulate the impact of various ideal WVD deployments.

## **Theory**

### **(i) Conceptual Water Vapor Diodes**

An ideal WVD is defined as a thin layer that satisfies three basic properties: (1) allow water vapor transfer in only one vertical direction; (2) reduce liquid water flow in both vertical directions; (3) allow conductive heat flow in both vertical directions. An “egg



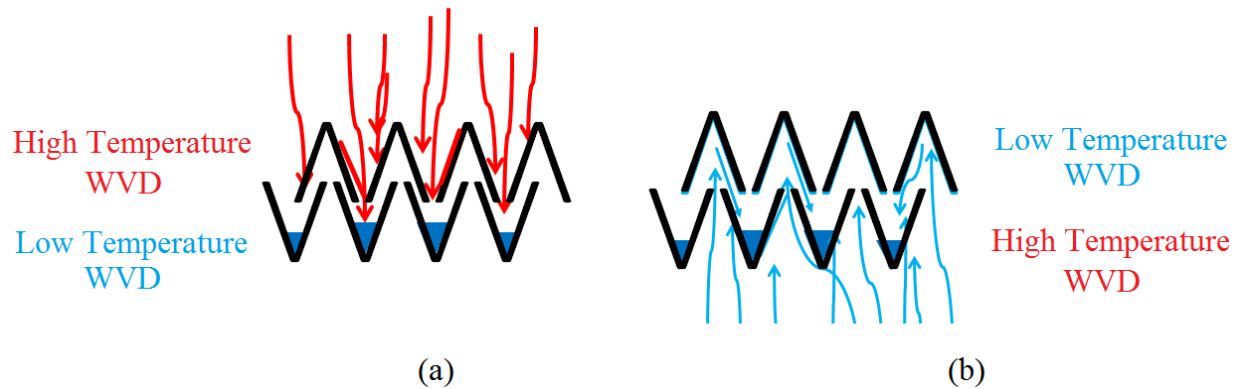


Fig. 4.1 Example water vapor diode pairs, and their effects on water vapor flow under two temperature gradient scenarios, i.e., (a) for daytime and (b) for nighttime. The red arrows indicate the trajectories of water vapor flow following the downward temperature gradient, while the azure arrows show water vapor flow following the upward temperature gradient. The “High Temperature WVD” and “Low Temperature WVD” indicate the relative temperature of the WVDs, and the blue areas in the cups of the lower WVD represent water accumulation.

carton” geometry, with pores at specific peaks and valleys, is a direct extension of the solar still, and we will use it to discuss the mechanism of the WVD. An example of a two-WVD configuration is shown in Fig. 4.1, with arrows indicating water vapor fluxes under a diurnal temperature variation. During the day time, soil heats up, and water vapor moves downwards following the direction of the temperature gradient (Fig. 4.1-a). The water vapor will first reach the bottom of the indentation, and condense in the cups of the lower WVD; while the heat will conduct through the WVD. Thus, the water will not propagate through the WVD. During the night time, the soil surface cools and the temperature gradient is upwards. Then heat and water vapor move up to the WVD (Fig. 1-b). The water vapor from the deep soil layer will be funneled through the lower WVD but stopped by the upper WVD, which can be conceptualized as multiple small-scale versions of a solar still. Thus, with the design in Fig.4.1, it is possible to create a semi-transmissible WVD layer, and water accumulates in the soil layer between the two WVDs.

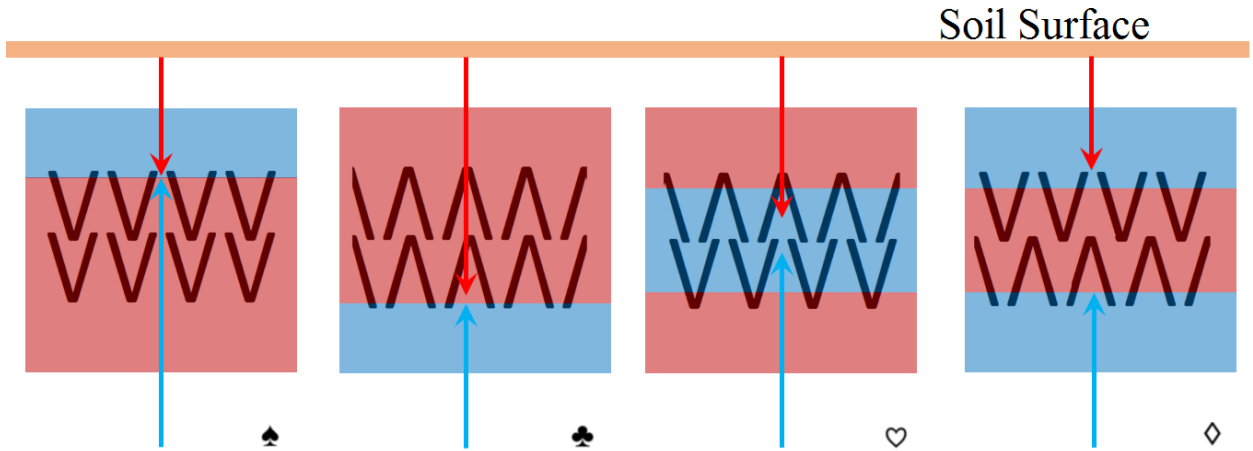


Fig. 4.2. Four configurations of the water vapor diodes. The example egg carton shape design is used. Red arrows represent day time downward vapor flow. Azure arrows represent night time upward vapor flow. Light blue rectangular areas illustrate relatively wet areas, and light red areas illustrate relatively dry areas due to water redistribution with WVDs.

Extending the example in Fig.4.1, we can control the direction of water vapor flux by shifting the WVDs. With two WVDs, we can consider the following four different configurations, which are shown in Fig. 4.2:

- ♠ (Upward): soil wetting occurs above the WVDs;
- ♣ (Downward): soil wetting occurs below the WVDs;
- ♥ (Inward): soil wetting occurs between the WVDs;
- ♦ (Outward): soil drying occurs between the WVDs.

Intuitively, ♥ is designed to accumulate water in a specific subsurface soil layer; ♦ is designed to create a dry soil layer. Conceptually, the ♠ and ♣ will accumulate water on one side of the WVDs; however, the actual impact of ♠ and ♣ on soil water distribution will depend on local climate conditions. In the following section, we will compare the four configurations to a soil condition where no WVD is applied (■).

## (ii) Coupled Heat and Water Movement Model

The liquid water and water vapor movement and heat transfer are fully coupled. Liquid water and water vapor transfers are treated as continuous processes with the assumption that the water vapor and liquid water maintain local equilibrium ( $dT/dt$ ) (de Vries, 1958). In the

model, the soil is uniform in structure and properties, and liquid water flux and water vapor flux vary with time, depth and temperature. Conduction, convection and latent heat transfer mechanisms are included in heat transfer (Milly, 1982; Nassar and Horton, 1997). Several soil specific enthalpy sources, e.g., specific enthalpy of dry soil, liquid water and water vapor, vaporization latent heat, and heat of wetting are also included in the model.

The governing equations are shown as follows. Eq. [4.1] is the water transfer equation, and Eq. [4.2] is the heat transfer equation.

$$\mathcal{H}_1 \frac{\partial h}{\partial t} + \mathcal{H}_2 \frac{\partial T}{\partial t} = \nabla \cdot \left[ \mathcal{H}_3 \frac{\partial h}{\partial z} + \mathcal{H}_4 \frac{\partial T}{\partial z} + K \mathbf{k} \right] \quad [4.1]$$

$$\mathcal{T}_1 \frac{\partial T}{\partial t} + \mathcal{T}_2 \frac{\partial h}{\partial t} = \nabla \cdot \left[ \mathcal{T}_3 \frac{\partial T}{\partial z} + \mathcal{T}_4 \frac{\partial h}{\partial z} + \mathcal{T}_5 \mathbf{k} \right] \quad [4.2]$$

$h$  (m) is the actual soil water matric potential at ambient temperature  $T$  (°C), which is a function of volumetric water content,  $\theta$  (m<sup>3</sup> m<sup>-3</sup>);  $K$  (m s<sup>-1</sup>) is hydraulic conductivity;  $t$  (s) is time;  $z$  (m) represents the depth; and  $\mathbf{k}$  is the unit vector pointing downwards. The left-hand sides of the equations represent the change of water potential and temperature with respect to time; while the right-hand sides of the equations indicate the water flow and heat flux within the soil profile. In this study, soil water redistribution relies on water vapor flux and liquid water flux.  $\mathcal{H}_1, \mathcal{H}_2, \mathcal{H}_3, \mathcal{H}_4$  are abbreviations for various soil hydraulic properties, while  $\mathcal{T}_1, \mathcal{T}_2, \mathcal{T}_3, \mathcal{T}_4, \mathcal{T}_5$  are abbreviations for various soil thermal properties. The coefficients of the water transfer equation are

$$\begin{cases} \mathcal{H}_1 = C + \frac{\phi - \theta}{\rho_l} \frac{\partial \rho_v}{\partial h} - C \frac{\rho_v}{\rho_l} \\ \mathcal{H}_2 = \frac{\phi - \theta}{\rho_l} \frac{\partial \rho_v}{\partial T} \\ \mathcal{H}_3 = D_{mv} + K \\ \mathcal{H}_4 = D_{Tv} + D_{Tl} \end{cases} \quad [4.3]$$

where  $C$  (m<sup>-1</sup>) is the specific water capacity;  $\phi$  (m<sup>3</sup> m<sup>-3</sup>) is the soil porosity;  $\rho_l \approx 1000$  kg m<sup>-3</sup> is the liquid water density;  $\rho_v$  (kg m<sup>-3</sup>) is the water vapor density;  $D_{mv}$  (m s<sup>-1</sup>) is water vapor diffusivity under soil matric potential gradient;

$D_{Tv}$  ( $\text{m}^2 \text{ } ^\circ\text{C}^{-1} \text{ s}^{-1}$ ) is water vapor diffusivity under soil thermal potential;

$D_{Tl}$  ( $\text{m}^2 \text{ } ^\circ\text{C}^{-1} \text{ s}^{-1}$ ) is liquid diffusivity under soil thermal gradient. The coefficients for the heat transfer equation are shown as follows,

$$\begin{cases} \mathcal{T}_1 = C_s + [L_0 + c_p(T - T_0)](\phi - \theta) \frac{\partial \rho_v}{\partial T} \\ \mathcal{T}_2 = [L_0 + c_p(T - T_0)] \left[ (\phi - \theta) \frac{\partial \rho_v}{\partial h} - C \rho_v \right] + [c_l(T - T_0) - W] C \rho_l \\ \mathcal{T}_3 = \lambda + c_l \rho_l (T - T_0) (D_{Tv} + D_{Tl}) \\ \mathcal{T}_4 = \rho_l L_T D_{mv} + c_l \rho_l (T - T_0) (D_{mv} + K) \\ \mathcal{T}_5 = c_l \rho_l (T - T_0) K \end{cases} \quad [4.4]$$

where  $C_s$  ( $\text{J m}^{-3} \text{ } ^\circ\text{C}^{-1}$ ) is the soil bulk heat capacity;  $L_0$  ( $\text{J kg}^{-1}$ ) is the latent heat of vaporization at reference temperature,  $T_0$ ;  $c_p$  ( $\text{J kg}^{-1} \text{ } ^\circ\text{C}^{-1}$ ) is the specific heat capacity of water vapor;  $c_l$  ( $\text{J kg}^{-1} \text{ } ^\circ\text{C}^{-1}$ ) is the specific heat capacity of liquid water;  $\lambda$  ( $\text{W m}^{-1} \text{ } ^\circ\text{C}^{-1}$ ) is the effective heat conductivity;  $L_T$  ( $\text{J kg}^{-1}$ ) is the latent heat of vaporization at temperature  $T$ . The definitions of each parameter in Eqs [4.3] and [4.4], as well as a brief derivation the governing equations, Eqs. [4.1] and [4.2], are shown in the Appendix A.

The numerical scheme used to solve Eqs. [4.1] and [4.2] is the implicit finite difference method. Central difference is used for the derivatives in the spatial domain; while implicit difference is used for the derivatives in the time domain. Since the governing equations are quasi-linear, i.e., the coefficients before  $\frac{\partial h}{\partial z}$  and  $\frac{\partial T}{\partial z}$  are related to  $h$  and  $T$ . A Picard iteration is used in the finite difference scheme.

## Materials and Methods

### (i) Soil Physical Properties

Ida silt loam (fine-silty, mixed, superactive, calcareous, mesic Typic Udorthents) properties as reported by Heitman et al. (2007) are used for the numerical simulations. The soil water retention curve (Campbell, 1974) is

$$h = h_e \left( \frac{\theta}{\theta_s} \right)^{-b} \quad [4.5]$$

Table 4.1. The parameters of soil thermal and hydraulic properties.

Soil	Textural fractions			organic matter	$\rho_b$ ( $Mg\ m^{-3}$ )
	Sand	Silt	Clay		
	%			%	
Silt loam	2	73	25	4.4	1.20
Soil	Hydraulic parameters				Permanent wilting point
	$h_e$ (m)	$b$	$\theta_s$ ( $m^3\ m^{-3}$ )	$K_s$ ( $m\ s^{-1}$ )	$\theta_{pwp}$ ( $m^3\ m^{-3}$ )
Silt loam	-0.13	6.53	0.55	$3.80 \times 10^{-7}$	0.18
Soil	Thermal conductivity parameters				
	$b_1$	$b_2$	$b_3$		
Silt loam	-0.95	-4.31	6.00		

where  $h_e$  (m) and  $b$  are fitting parameters and  $\theta_s$  ( $m^3\ m^{-3}$ ) is the saturated water content.  $K$  follows the equation (Campbell, 1974)

$$K = \frac{\mu(T_0)}{\mu(T)} \left( \frac{\theta}{\theta_s} \right)^{2b+3} K_s \quad [4.6]$$

where  $K_s$  ( $m\ s^{-1}$ ) is the saturated hydraulic conductivity at  $T_0$ ;  $\mu$  ( $m^2\ s^{-1}$ ) is the dynamic viscosity of liquid water, which is a function of  $T$ .  $C_s$  is expressed as the weighted average of the specific heat of the soil solid portion, liquid portion and gas portion (Kluitenberg, 2002), i.e.,

$$C_s = \rho_b(c_o\phi_o + c_m\phi_m) + c_g\rho_g\theta_g + c_l\rho_l\theta \quad [4.7]$$

where  $\rho_b$  ( $kg\ m^{-3}$ ),  $\rho_g$  ( $kg\ m^{-3}$ ) are the soil bulk density and gas density;  $c_o$  ( $J\ kg^{-1}\ ^\circ C^{-1}$ ),  $c_m$  ( $J\ kg^{-1}\ ^\circ C^{-1}$ ),  $c_g$  ( $J\ kg^{-1}\ ^\circ C^{-1}$ ) are the specific heats of organic matter, soil minerals and soil gas;  $\phi_o$  ( $kg\ kg^{-1}$ ) and  $\phi_m$  ( $kg\ kg^{-1}$ ) are organic fraction and mineral fraction;  $\theta_g$  ( $m^3\ m^{-3}$ ) is the soil gas fraction. The  $\lambda$ -relationship is from Horton and Chung (1991),

$$\lambda = b_1 + b_2\theta + b_3\theta^{0.5}$$

[4.8]

where the parameter values  $b_1, b_2, b_3$  for the Ida silt loam are listed in Table 4.1.

## (ii). Initial and Boundary Conditions

In this study, the initial conditions are defined as a uniform water content and temperature distribution within the soil profile. We assume the soil profile is deep enough such that the deep layers are stable in matric potential and temperature, i.e., the lower boundary condition for water transfer is the unit gradient condition; and for the heat transfer equation, a constant temperature condition is adopted.

The upper boundary conditions are related to the soil surface and atmosphere conditions. They can be formulated with the surface water and energy balance (Campbell and Norman, 1998; Horton and Chung, 1991; Sauer and Horton, 2005). Let  $E$  ( $\text{kg m}^{-2} \text{s}^{-1}$ ) denote the surface evaporation between soil and atmosphere. The surface water matric potential,  $h_s$  (m), and the surface temperature,  $T_s$  ( $^{\circ}\text{C}$ ), are the target values. The subscript s is adopted to emphasize that these conditions are for the soil surface. The mass balance relationship of water at the soil surface is shown as follows

$$C \frac{dh_s}{dt} + \frac{1}{\rho_l} \nabla \cdot (E + q_l + q_v) = 0$$

[4.9]

The energy balance equation is

$$R_n - H_s - L_T(E - q_v) - G = 0$$

[4.10]

where  $R_n$  ( $\text{W m}^{-2}$ ) is the net radiation;  $H_s$  ( $\text{W m}^{-2}$ ) is the surface sensible heat flux;  $L_T(E - q_v)$  is the latent heat flux at the soil surface, with  $E - q_v$  representing the actual surface water vaporization quantity at the soil surface;  $G$  ( $\text{W m}^{-2}$ ) is the surface ground heat flux term. Air temperature ( $T_a$ ,  $^{\circ}\text{C}$ ), air relative humidity ( $RH_a$ ), wind speed ( $u_a$ ,  $\text{m s}^{-1}$ ) and global radiation ( $R_g$ ,  $\text{W m}^{-2}$ ) are four input quantities necessary to evaluate the upper boundary conditions, and the detailed procedures are shown in Appendix B.

We can discretize Eqs. [4.9] and [4.10] to form an equation system at the soil surface, and solve for  $h_s$  and  $T_s$ . In the simulation, the measured values of  $T_a, RH_a, u_a, R_g$  are obtained

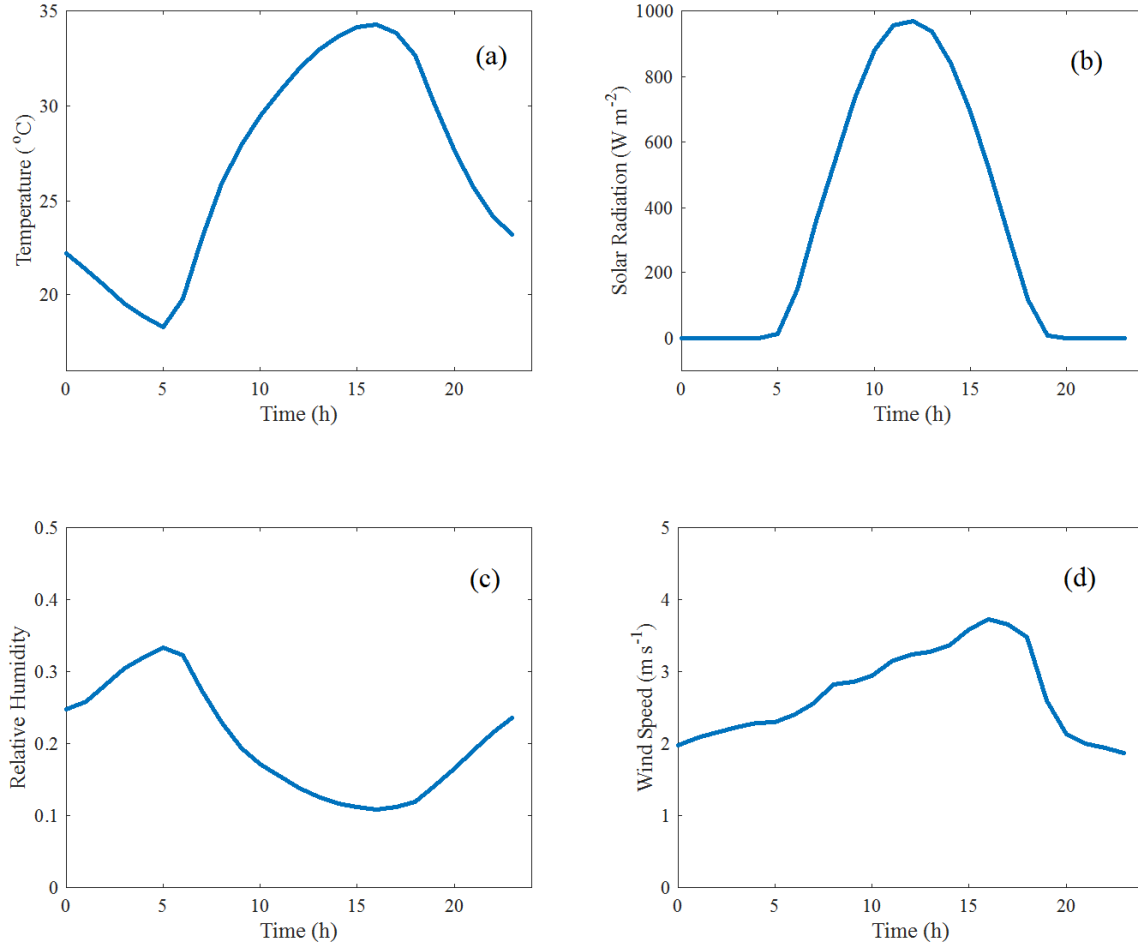


Fig. 4.3. The measured  $T_a$ ,  $RH_a$ ,  $u_a$ ,  $R_g$  data from Maricopa County, AZ, during May 2013. These data are used to create the upper boundary conditions of the coupled heat and water transfer simulation.

from weather database observed at Maricopa County, AZ, during May 2013, which are shown in Fig. 4.3 (access from <https://cals.arizona.edu/azmet/06.htm>). The 24-hour patterns of those quantities are the hourly averaged results through the whole month, and smoothed by polynomial regressions. The diurnal weather conditions are repeated for day-after-day simulations.

In order to represent the configurations of ideal WVDs in soil, internal boundary conditions are added for the WVDs. The liquid water flux across the internal WVD boundary is 0, while the water vapor flux is allowed in one vertical direction, which is based on the

WVD configuration (Fig. 4.2). Conductive heat transfer is allowed in both directions across the WVD, while the convective heat transfer through liquid water and water vapor depends on water vapor transfer across the WVDs.

## Results and Discussion

In this section, we will present the simulation with ideal WVDs. 30-day simulations were conducted as the numerical examples shown in this section. We first compare the effect of different configurations of WVDs on soil water redistribution. Secondly, we will focus on the ♡ case and evaluate the water accumulation results.

### (i) Simulation Results of Four Configurations

Figure 4.4 shows the 30-day simulation results using the coupled heat and water transfer model with the initial and boundary conditions discussed in section 3.2. WVDs are deployed at a 5-cm depth and a 10-cm depth. Figure 4.4-a presents the comparisons among ♠, ♣ and ■. During the daytime, a relatively large evaporation flux occurs at the soil surface; while during the nighttime, some water vapor will enter the soil surface and condense in the soil. Vaporization is the dominant mass transfer process in this example, and the  $\theta$  in shallow layers decreases in ■ over the 30-day simulation. WVDs in ♠ allow the upward water vapor flux during the daytime, but block the downward flux during the nighttime. Thus, compared with ■, the  $\theta$  in ♠ below the lower WVD is slightly smaller, due to zero water input from shallow soil layers during night periods. However, since evaporation is the dominant means for water transport, the difference between ♠ and ■ is quite small. WVDs in ♣ block upward liquid water and water vapor fluxes; however, the upward water transfer driven by the thermal gradient still occurs in the soil layers without WVDs. Thus, water accumulates in soil below each WVD. The  $\theta$  in the soil right above each WVDs in ♣ is smaller than that for ♠ and ■, because the WVD blocks water vapor input from the soil layers right below the WVD.

Figure 4.4-b presents the comparisons among ♡, ♦ and ■ for the 30-day simulations. In ♡, the upper WVD allows the downward water vapor flux, while the lower WVD allows the upward water vapor flux. Thus, the water is trapped between the two WVDs, and a relatively



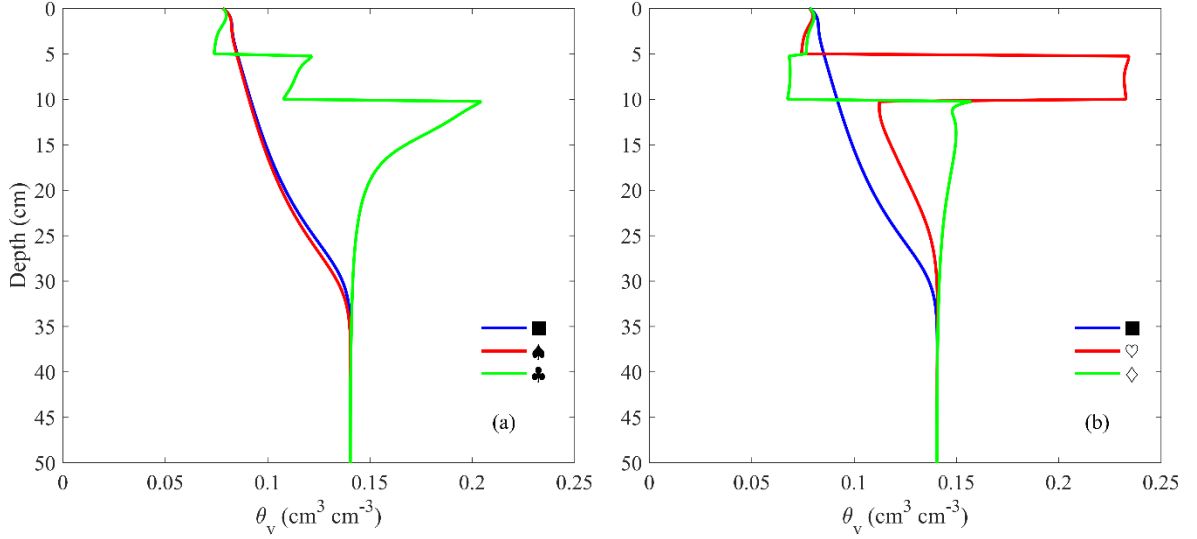


Fig. 4.4. The influence of WVD placements on soil water distribution after 30-day simulations. WVDs are set at 5 cm and 10 cm depths. The results of four different configurations are compared with the simulation results without WVD. The initial water content is  $\theta_{v,ini} = 0.14 \text{ m}^3 \text{ m}^{-3}$ ; the initial temperature is 25 °C (approximately equal to the mean air temperature); the free drainage condition is assigned to the lower boundary for water transfer; and the lower boundary condition of temperature is 25 °C. The upper boundary condition follows Eq. [4.9] and [4.10], where the weather dataset shown in Fig. 3 is repeated for 30 days.

wet 5-10 cm soil layer is created. After the 30-day simulation, the  $\theta$  is increased by  $0.1 \text{ m}^3 \text{ m}^{-3}$  compared to ■. The WVDs in  $\diamond$  are opposite to  $\heartsuit$ , where the upper WVD allows the upward water vapor transfer, and the lower WVD allows the downward water vapor transfer. Thus, in  $\diamond$ , there is no water input for the 5-10 cm soil layer, so a relatively dry soil layer is created.  $\heartsuit$  and  $\diamond$  are the two important configurations of WVDs. WVDs for  $\heartsuit$  can be deployed within a root zone to accumulate water in support of plant growth. In this numerical example, the initial  $\theta = 0.14 \text{ m}^3 \text{ m}^{-3}$ , and the permanent wilting point  $\theta_{pwp} = 0.18 \text{ m}^3 \text{ m}^{-3}$ . After the 30-day simulation, the maximum  $\theta$  between the WVDs in  $\heartsuit$  exceeds  $\theta_{pwp}$ , making the soil wet enough to supply water to plant roots. Thus,  $\heartsuit$  is the most

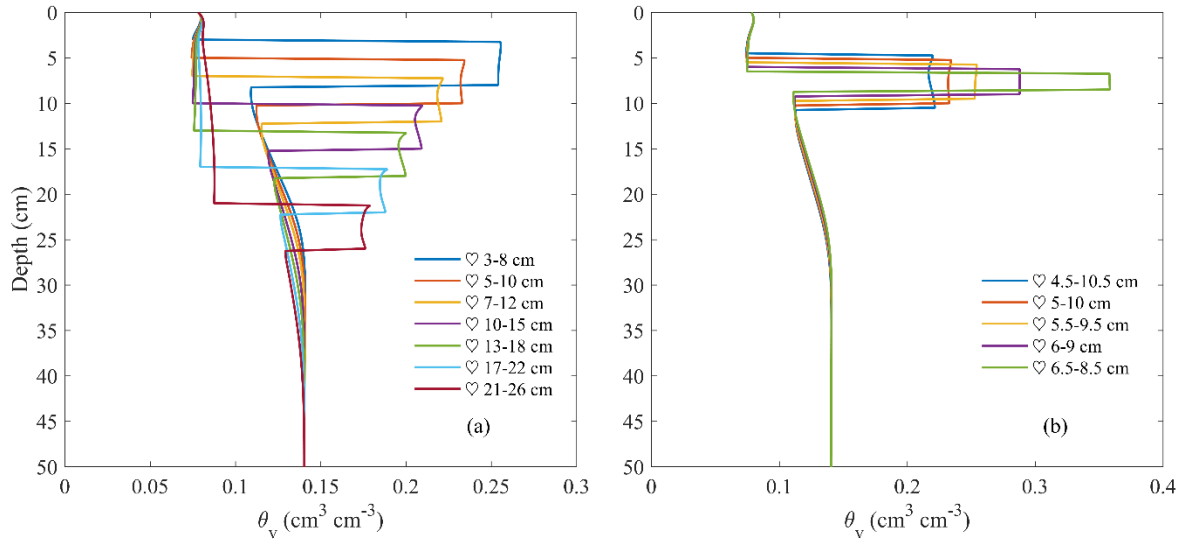


Fig. 4.5. The influence of different manipulations [depth (a) and spacing (b)] of configuration ♡ on soil water distribution after 30-day simulations.

interesting WVD configuration from a perspective of plant water availability, and we will provide more discussion on its properties in the following section. The configuration in  $\diamond$  can be used beneath the foundations of roads, where compacted dry soil is necessary to make the foundation stable.

The numerical model used for the simulations is validated with published data (Heitman et al., 2008). The simulation results are evaluated using the mass balance of water. Mass balance calculations indicate that the relative errors are less than 2% for the 30-day simulations.

## (ii) Discussion on the Inward Configuration

The configuration ♡ can be manipulated in two ways. One is to vary the depths of the two WVDs, while maintaining the same distance between the two WVDs. The other manipulation is to keep the center depth constant for the two WVDs, but shrink or expand the distance between the two WVDs. Figure 5 presents the simulation results regarding these two manipulations for the same initial and boundary conditions presented in section 3.2.

In Fig. 4.5-a, the distance between the two WVDs is kept constant at 5 cm. The upper WVDs are placed at depths of 3 cm, 5 cm, 7 cm, 10 cm, 13 cm, 17 cm and 21 cm; while the

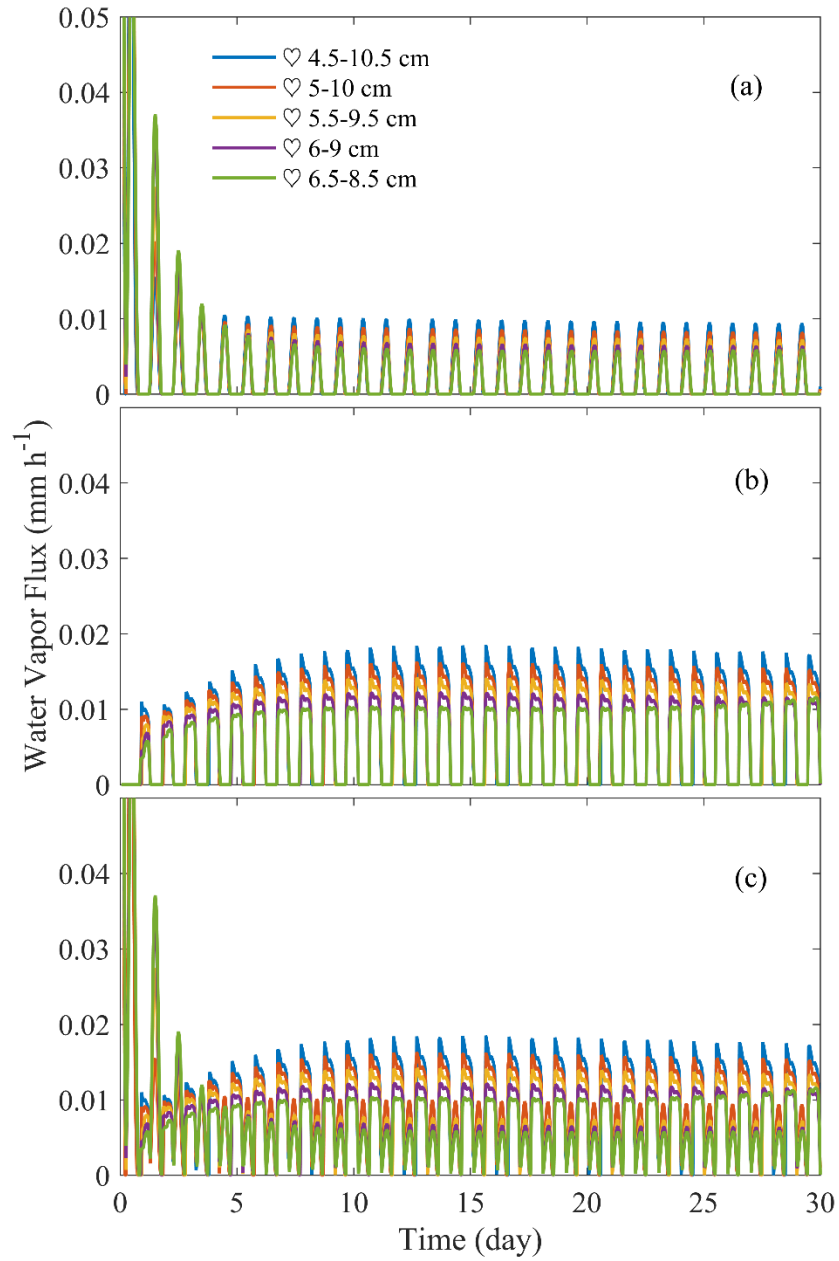


Fig. 4.6. The water vapor fluxes from the upper WVD layer (a), lower WVD layer (b) and the sum of water vapor flux (c) during the 30-day simulation period for configuration ♡ at different space separations.

corresponding lower WVDs are placed at depths of 8 cm, 10 cm, 12 cm, 15 cm, 18 cm, 22 cm and 26 cm, respectively. The simulation period is 30 days. Water accumulation between the WVDs can be observed in all of the deployments. The maximum  $\theta$  values decrease with respect to the depth. The reason is that as depth increases, magnitude of the thermal gradient decreases. Thus, the water vapor fluxes across the WVDs, driven by the thermal gradient, decrease. Compared to the WVDs at shallow depths, the deep WVDs cannot accumulate as much water. Thus, the  $\theta$  increases for deep WVDs are smaller than those for shallow WVDs.

In Fig. 4.5-b, the center of the two WVDs is fixed at a depth of 7.5 cm, and the distances between the two WVDs are 6 cm, 5 cm, 4 cm, 3 cm and 2 cm. For 30-day simulations, the thinner the soil layer between the WVDs, the larger the increase in  $\theta$ . In this case, the thickness of the soil layer becomes a dominant factor for  $\theta$  increases. The initial  $\theta = 0.14 \text{ m}^3 \text{ m}^{-3}$ , and the final  $\theta$  values range from 0.20 to  $0.36 \text{ m}^3 \text{ m}^{-3}$ . A similar amount of water enters a relatively thin soil layer, as enters a relatively thick soil layer, resulting in a relatively large increase of  $\theta$  in the thin soil layer. The importance of the two manipulations is that different WVD deployments in  $\heartsuit$  can be selected based on the specific climate condition, soil type and water accumulation needs. Numerical simulations and field validations should be performed to achieve an optimal deployment for a desired  $\theta$  increase.

Besides increasing of  $\theta$  with  $\heartsuit$  configuration, it is important to evaluate whether  $\heartsuit$  can maintain the  $\theta$  increases over a continuous time period in the presence of a water sink, such as root-water-uptake. Important values to quantify are the water fluxes through the upper and lower WVDs for the deployments associated with the results shown in Fig. 4.5-b. If a stable daily water vapor flux can be maintained, it can represent the water accumulation ability for these WVD deployments.

Figure 4.6 presents the water vapor flux from the upper WVD (Fig. 4.6-a), lower WVD (Fig. 4.6-b) and the sum of the water vapor fluxes entering the soil layer between two WVDs (Fig. 4.6-c). The initial unstable part is affected by the initial conditions. From the results, the water vapor fluxes through the upper and lower WVDs follow a “half-sine-wave” pattern. The magnitudes of the half-sine-wave for the upper WVDs decrease and approach stable values; while the magnitudes of the half-sine-wave for the lower WVDs increase to relatively stable values. It can also be observed in Fig. 4.6-a and b that for these simulations, the

maximum water vapor fluxes through the WVDs differ slightly from each other. If we consider the cumulative daily water fluxes, all of the deployments have a water accumulation ability of almost  $0.2 \text{ mm day}^{-1}$ . That value is the maximum that the sinks can remove while maintaining the relatively large  $\theta$  values between the two WVDs in configuration ♡. If the plant density is sparse allowing roots to extend laterally into soil between plants, then it may be possible that water accumulation by the WVDs can supply plant transpiration needs. Thus, WVD accumulation of water has potential ecological significance for drought-stressed arid and semi-arid plants or for plant establishment in reclamation settings.

### Summary

A WVD design based on an expansion of the solar still principle is presented in this study, and one-dimensional numerical simulations using a coupled heat and water transfer model are used to evaluate the influence of the conceptual WVDs on soil water movement. The ideal WVDs are one-directional transmissible layers for water vapor, and they are barriers for liquid water transfer. Conductive heat fluxes can propagate through the WVD in both directions. In this paper, we illustrate the mechanism using an “egg carton” design of WVD. By properly arranging two WVDs, the water vapor can be concentrated or drained laterally out of the soil between the two WVDs, and a relatively wet or dry area can be created between the two WVDs. The results show that the ideal WVDs can effectively change soil water redistribution with a variety of configurations and deployments. The inwards configuration (♡) is able to accumulate water in the soil layer positioned between two WVDs. In general, the increase of volumetric water content ( $\theta$ ) for ♡ is greater than  $0.1 \text{ m}^3 \text{ m}^{-3}$  for the conditions in this study. The  $\theta$  increase depends on the deployment of the WVDs in ♡; shallower deployments and the shorter the distances between the WVDs results in larger  $\theta$  increases. The numerical simulations also provide water vapor flux values through the two WVDs in ♡, which indicate the water accumulation ability for several deployments. In conclusion, WVDs can influence soil water redistribution. An inward configuration can be used to accumulate water in a specific soil layer to increase soil water availability to plants or other biological organisms.

In the one-dimensional simulations included in this study, all of the WVDs are considered to act as ideal one-directional barriers for water vapor, i.e., possible back-leakage of water vapor through the WVD is not allowed. In reality, potential leaking is related to the real design of the two-dimensional WVD geometries, the material used for WVDs, and the soil and weather conditions. Thus, additional two-dimensional numerical studies are needed. Under field conditions, the non-equilibrium mass transfer between liquid water and water vapor may also occur (Smits et al., 2011). Thus, real field experiments are necessary to test and verify actual WVD performances.

### Acknowledgements

This work was supported by the National Science Foundation under Grant 1623806, USDA-NIFA, Multi-State Project 3188, Iowa State University Department of Agronomy, the Hatch Act, and State of Iowa funds.

### References

- Badran, A.A., A.A. Al-Hallaq, I.A. Eyal Salman and M.Z. Odat. (2005). "A solar still augmented with a flat plate collector." *Desalination*. 172:227–234. doi: 10.1016/j.desal.2004.06.203.
- Bittelli, M., F. Ventura, G.S. Campbell, R.L. Snyder, F. Gallegati and P.R. Pisa. (2008). "Coupling of heat, water vapor, and liquid water fluxes to compute evaporation in bare soils." *J. Hydrol.* 362: 191-205. <http://dx.doi.org/10.1016/j.jhydrol.2008.08.014>
- Campbell, G.S. (1974). "A simple method for determining unsaturated conductivity from moisture retention data." *Soil Sci.* 117: 311-314. doi: 10.1097/00010694-197406000-00001.
- Campbell, G.S. and J.M. Norman. (1998). "An Introduction to Environmental Biophysics (Second Edition)." Springer, New York. doi: 10.1007/978-1-4612-1626-1.
- Cary, J.W. (1966). "Soil moisture transport due to thermal gradients: practical aspects." *Proc. Soil Sci. Soc. Am.*, 30:428-433. doi:10.2136/sssaj1966.03615995003000040011x.
- Cass, A., G.S. Campbell, and T.L. Jones. (1984). "Enhancement of thermal water vapor diffusion in soil." *Soil Sci. Soc. Am. J.* 48:25–32. doi:10.2136/sssaj1984.03615995004800010005x.
- de Vries, D.A. (1958). "Simultaneous Transfer of Heat and Moisture in Porous Media." *Trans. Am. Geophys. Union*. 39: 909–916. doi/10.1029/TR039i005p00909.
- Heitman, J. L., R. Horton, T. Ren, I. N. Nassar and D. D. Davis. (2008). "A Test of Coupled Soil Heat and Water Transfer Prediction under Transient Boundary Temperatures." *Soil Sci. Soc. Am. J.* 72:1197-1207. doi:10.2136/sssaj2007.0234.

- Horton, R. and S. Chung. (1991). "Soil Heat Flow. Modeling Plant and Soil Systems." 397-438. doi:10.2134/agronmonogr31.c17.
- Jackson R.D., B.A. Kimball, R.J. Reginato and F.S. Nakayama. (1973). "Diurnal Soil-Water Evaporation: Time-Depth-Flux Patterns." *Soil Sci. Soc. Amer. Proc.* 37: 505-509. doi:10.2136/sssaj1973.03615995003700040014x.
- Jackson, R. D., R. J. Reginato, B. A. Kimball, and F. S. Nakayama. (1974). "Diurnal Soil-Water Evaporation: Comparison of Measured and Calculated Soil-Water Fluxes." *Soil Sci. Soc. Amer. Proc.* 38:861-866. doi:10.2136/sssaj1974.03615995003800060012x.
- Jackson R.D. and C.H.M. van Bavel. (1965). "Solar Distillation of Water from Soil and Plant Materials: A Simple Desert Survival Technique." *Science*. 149:1377-1379. PMID: 5826532.
- Kimball, B.A., R.D. Jackson, R.J. Reginato, F.S. Nakayama, and S.B. Idso. (1976). "Comparison of field-measured and calculated soil heat fluxes." *Soil Sci. Soc. Am. J.* 40:18–28. doi:10.2136/sssaj1976.03615995004000010010x.
- Kluitenberg, G.J. (2002). "Heat capacity and specific heat. Methods of soil analysis." *Part 4. Physical Methods*. 1201–1208. doi:10.2136/sssabookser5.4.c49.
- Lai, S., J. M. Tiedje and A. E. Erickson. (1976). "In situ measurement of gas diffusion coefficients in soils." *Soil Sci. Soc. Am. Proc.* 40: 3-6. doi:10.2136/sssaj1976.03615995004000010006x
- Li, X. (2003). "Gravel–sand mulch for soil and water conservation in the semiarid loess region of northwest China." *Catena*. 52:105– 127. doi:10.1016/S0341-8162(02)00181-9.
- Liu, X., B. He, X. Yi, L. Zhang, and F. Han. (2016). "The soil water dynamics and hydraulic processes of crops with plastic film mulching in terraced dryland fields on the Loess Plateau." *Environ Earth Sci.* 75:809-824. doi:10.1007/s12665-016-5670-x.
- Milly, P.C.D. (1982). "Moisture and Heat Transport in Hysteretic, Inhomogeneous Porous Media: A Matric Head-Based Formulation and a Numerical Model." *Water Resour. Res.* 18:489- 498. doi: 10.1029/WR020i008p01087.
- Nassar, I. N. and R. Horton. (1989a). "Water transport in unsaturated nonisothermal salty soil: I. Experimental results." *Soil Sci. Soc. Am. J.* 53:1323-1329. doi:10.2136/sssaj1989.03615995005300050004x.
- Nassar, I.N. and R. Horton. (1989b). "Water transport in unsaturated nonisothermal salty soil: II. Theoretical development." *Soil Sci. Soc. Am. J.* 53:1330–1337. doi:10.2136/sssaj1989.03615995005300050005x.
- Nassar, I.N. and R. Horton. (1997). "Heat, water, and solute transfer in unsaturated porous media: I. Theory development and transport coefficient evaluation." *Trans. in Porous Media*. 27:17-38. doi:10.1023/A:1006583918576.

- Philip J.R. and D.A. de Vries. (1957). “Moisture Movement in Porous Materials under Temperature Gradients.” *Trans. Am. Geophys. Union*. 38:222–232. doi:10.1029/TR038i002p00222.
- Sauer, T.J. and R. Horton. (2005). “Soil Heat Flux.” *Micrometeorology in Agricultural Systems*. 131-154. doi:10.2134/agronmonogr47.c7.
- Smits, K. M., A. Cihan, T. Sakaki, and T. H. Illangasekare. (2011). “Evaporation from soils under thermal boundary conditions: Experimental and modeling investigation to compare equilibrium- and nonequilibrium-based approaches.” *Water Resour. Res.*, 47(5), W05540, doi:10.1029/2010WR009533.
- Sui, H., D. Zeng and F. Chen. (1992). “A numerical model for simulating the temperature and moisture regimes of soil under various mulches.” *Agr. Forest. Meteorol.* 61:281-299. doi: [http://dx.doi.org/10.1016/0168-1923\(92\)90054-8](http://dx.doi.org/10.1016/0168-1923(92)90054-8).
- van Bavel, C.H.M and D.I. Hillel. (1976). “Calculating Potential and Actual Evaporation from a Bare Soil Surface by Simulation of Concurrent Flow of Water and Heat.” *Agric. Meteorol.* 17: 453– 476. [http://dx.doi.org/10.1016/0002-1571\(76\)90022-4](http://dx.doi.org/10.1016/0002-1571(76)90022-4).
- Willis, W. O., H. J. Haas and J. S. Robins. (1963). “Moisture Conservation by Surface or Subsurface Barriers and Soil Configuration under Semiarid Conditions.” *Soil Sci. Soc. Am. J.* 27:577-580. doi:10.2136/sssaj1963.03615995002700050031x.
- Yang, Q, H. Zuo, X. Xiao, S. Wang, B. Chen and J. Chen. (2012). “Modelling the effects of plastic mulch on water, heat and CO<sub>2</sub> fluxes over cropland in an arid region.” *J. Hydrol.* 452:102-118. doi: <http://dx.doi.org/10.1016/j.jhydrol.2012.05.041>

## Appendix A

A brief derivation of the water transfer and heat transfer equations, i.e., Eqs. [4.1] and [4.2], is given as follows. We set  $T_0 = 20^\circ\text{C}$  as the reference temperature. For the water vapor flux,  $q_v$  ( $\text{kg m}^{-2}\text{s}^{-1}$ ), we have

$$q_v = -D\Omega(\phi - \theta) \frac{d\rho_v}{dz} \quad [4.A1]$$

$D = 2.29 \times 10^{-5}(T/273.15)^{1.75} \text{ m}^2 \text{ s}^{-1}$  is the water vapor diffusion coefficient in air (Kimball et al., 1976);  $\Omega = (\phi - \theta)^{2/3}$  is the tortuosity (Lai et al., 1976). Since the model assumes the water vapor phase is in local equilibrium with the liquid phase, we have

$$\rho_v = \rho_{vs} \times RH = \exp\left(19.84 - \frac{4975.9}{T}\right) \exp\left(\frac{gMh}{RT}\right) \quad [4.A2]$$

$\rho_{vs}$  ( $\text{kg m}^{-3}$ ) is the saturated water vapor density, which is a function of temperature (Kimball et al., 1976); and  $RH$  is the relative humidity, which is a function of gravitational



acceleration  $g \approx 9.81 \text{ m s}^{-2}$ , molecular weight of water  $M \approx 0.018 \text{ kg mol}^{-1}$ , gas constant  $R \approx 8.314 \text{ J mol}^{-1} \text{ }^\circ\text{C}^{-1}$ ,  $h$  and  $T$ . In general,  $h = h_0 \exp[-2.09 \times 10^{-3}(T - T_0)]$  is the relation of the soil matric potential between the ambient temperature and the reference temperature, where  $h$  is the matric potential at  $T$  and  $h_0$  is the matric potential at  $T_0$ . Insert Eq. [4.A2] to [4.A1] to obtain the vapor transfer equation,

$$\frac{q_v}{\rho_l} = -\eta \underbrace{\frac{D\Omega(\phi - \theta)}{\rho_l} \left[ RH \frac{d\rho_{vs}}{dT} + \rho_{vs} \frac{\partial RH}{\partial T} \right]}_{D_{Tv}} \frac{dT}{dz} - \underbrace{\frac{D\Omega(\phi - \theta)\rho_{vs}}{\rho_l} \frac{\partial RH}{\partial h}}_{D_{mv}} \frac{dh}{dz} \quad [4.A3]$$

$\eta$  is included as a vapor enhancement factor for porous media, and  $\eta = 8 + 6\theta - 7 \exp\left\{-\left[(1 + \rho/\sqrt{\alpha})\theta\right]^4\right\}$  by Cass et al. (1984) and Campbell (1985), where  $\rho = 2600 \text{ kg m}^{-3}$  is the particle density and  $\alpha \text{ (kg kg}^{-1}\text{)}$  is the mass fraction of clay. Similarly, using the total derivative of  $h$ , i.e.,  $\frac{dh}{dz} = \frac{\partial h}{\partial T} \frac{\partial T}{\partial z} + \frac{\partial h}{\partial z}$  and Darcy's Law, the soil liquid water flux,  $q_l \text{ (kg m}^{-2}\text{s}^{-1}\text{)}$ , can be written as (Nassar and Horton, 1989b; Heitman et al., 2008)

$$\frac{q_l}{\rho_l} = -K \underbrace{\frac{\partial h}{\partial T} \frac{\partial T}{\partial z}}_{D_{Tl}} - K \frac{\partial h}{\partial z} - K\mathbf{k} \quad [4.A4]$$

We write  $\frac{\partial T}{\partial z}$  to indicate that  $T$  is also a function of time,  $t$ . The total water content is  $\theta_T = \theta + \rho_v(\phi - \theta)/\rho_l$ . Thus, the left-hand side of Eq. [1] can be expanded as,

$$\begin{aligned} \frac{\partial \theta_T}{\partial t} &= \frac{\partial \theta}{\partial t} + \frac{\phi - \theta}{\rho_l} \frac{\partial \rho_v}{\partial h} \frac{\partial h}{\partial t} - C \frac{\rho_v}{\rho_l} \frac{\partial h}{\partial t} + \frac{\phi - \theta}{\rho_l} \frac{\partial \rho_v}{\partial T} \frac{\partial T}{\partial z} \\ &= \left[ C + \frac{\phi - \theta}{\rho_l} \frac{\partial \rho_v}{\partial h} - C \frac{\rho_v}{\rho_l} \right] \frac{\partial h}{\partial t} + \frac{\phi - \theta}{\rho_l} \frac{\partial \rho_v}{\partial T} \frac{\partial T}{\partial z} \end{aligned} \quad [4.A5]$$

where  $C = \frac{\partial h}{\partial \theta}$  is the specific water capacity. Using the continuity equation  $\rho_l \frac{\partial \theta_T}{\partial t} = \nabla \cdot$

$(q_l + q_v)$  and imposing local equilibrium, we obtain the water transfer equation (Eq. [4.1]),

$$\underbrace{\left[ C + \frac{\phi - \theta}{\rho_l} \frac{\partial \rho_v}{\partial h} - C \frac{\rho_v}{\rho_l} \right] \frac{\partial h}{\partial t}}_{\mathcal{H}_1} + \underbrace{\frac{\phi - \theta}{\rho_l} \frac{\partial \rho_v}{\partial T} \frac{\partial T}{\partial z}}_{\mathcal{H}_2} = \nabla \cdot \left[ \underbrace{(D_{mv} + K)}_{\mathcal{H}_3} \frac{\partial h}{\partial z} + \underbrace{(D_{Tv} + D_{Tl})}_{\mathcal{H}_4} \frac{\partial T}{\partial z} + K\mathbf{k} \right] \quad [4.A6]$$

The governing heat transfer equation (Milly, 1982; Nassar and Horton, 1997) can be written straightforward based on analysis of the water transfer equation. The total energy contained in a given unit volume of soil can be written as

$$H = c_d(T - T_0) + L_0\rho_v(\phi - \theta) + [c_p\rho_v(\phi - \theta) + c_l\rho_l\theta](T - T_0) - \rho_l \int_0^\theta W d\theta \quad [4.A7]$$

where  $H$  ( $\text{J m}^{-3}$ ) represents the energy per unit volume of bulk soil. The change of  $H$  with respect to time indicates the energy income and output from particular soil layers.

$c_d$  ( $\text{J m}^{-3} \text{ }^\circ\text{C}^{-1}$ ) is the heat capacity of dry soil.  $W$  ( $\text{J kg}^{-1}$ ) is the differential heat of wetting.

By differentiating  $H$  with respect to time, we obtain

$$\begin{aligned} \frac{\partial}{\partial t} H = & [c_d + c_p\rho_v(\phi - \theta) + c_l\rho_l\theta] \frac{\partial T}{\partial t} + [L_0 + c_p(T - T_0)](\phi - \theta) \frac{\partial \rho_v}{\partial t} \\ & - [L_0 + c_p(T - T_0)]\rho_v \frac{\partial \theta}{\partial t} + [c_l(T - T_0) - W]\rho_l \frac{\partial \theta}{\partial t} \end{aligned} \quad [4.A8]$$

Let  $C_s = c_d + c_p\rho_v(\phi - \theta) + c_l\rho_l\theta$  ( $\text{J m}^{-3} \text{ }^\circ\text{C}^{-1}$ ). Recall that in Eq. [4.A3],  $\rho_v$  is a function of  $T$  and  $h$ . We exchange  $\frac{\partial \theta}{\partial t}$  by  $\frac{\partial h}{\partial t}$  using the specific water capacity  $C$

$$\begin{aligned} \frac{\partial}{\partial t} H = & C_s \frac{\partial T}{\partial t} + [L_0 + c_p(T - T_0)](\phi - \theta) \left[ \frac{\partial \rho_v}{\partial T} \frac{\partial T}{\partial t} + \frac{\partial \rho_v}{\partial h} \frac{\partial h}{\partial t} \right] - [L_0 + c_p(T - T_0)]C\rho_v \frac{\partial h}{\partial t} \\ & + [c_l(T - T_0) - W]C\rho_l \frac{\partial h}{\partial t} \\ = & \underbrace{\left[ C_s + [L_0 + c_p(T - T_0)](\phi - \theta) \frac{\partial \rho_v}{\partial T} \right]}_{\mathcal{T}_1} \frac{\partial T}{\partial t} \\ & + \underbrace{\left[ [L_0 + c_p(T - T_0)] \left[ (\phi - \theta) \frac{\partial \rho_v}{\partial h} - C\rho_v \right] + [c_l(T - T_0) - W]C\rho_l \right]}_{\mathcal{T}_2} \frac{\partial h}{\partial t} \end{aligned} \quad [4.A9]$$

The heat flux  $q_h$  ( $\text{J m}^{-2} \text{ s}^{-1}$ ) can be written as follows (de Vries, 1958)

$$q_h = -\lambda_* \frac{\partial T}{\partial z} + L_0 q_v + c_p(T - T_0) q_v + c_l(T - T_0) q_l \quad [4.A10]$$

where  $\lambda_*$  ( $\text{W m}^{-1} \text{ }^\circ\text{C}^{-1}$ ) is the thermal conductivity of bulk soil. The first term represents the conductive heat transfer; the second terms represents the convective latent heat transfer; while the last two terms represents the convective sensible heat transfer. Use  $L_0 + c_p(T - T_0) = L_T + c_l(T - T_0)$  to define latent heat of vaporization at  $T$ , i.e.,  $L_T$ .  $q_v$  and  $q_l$  are expanded using Eqs. [4.A3] and [4.A4]. The heat flux can be rewritten as

$$\begin{aligned}
 q_h &= -\lambda_* \frac{\partial T}{\partial z} + L_T q_v + c_l(T - T_0)(q_v + q_l) \\
 &= -\underbrace{\left[ \lambda_* \frac{\partial T}{\partial z} + \rho_l L_T D_{Tv} \frac{\partial T}{\partial z} \right]}_{\lambda \frac{\partial T}{\partial z}} - \rho_l L_T D_{mv} \frac{\partial h}{\partial z} + c_l(T - T_0)(q_v + q_l) \\
 &= -\lambda \frac{\partial T}{\partial z} - \rho_l L_T D_{mv} \frac{\partial h}{\partial z} \\
 &\quad - c_l \rho_l (T - T_0) \left[ D_{Tv} \frac{\partial T}{\partial z} + D_{mv} \frac{\partial h}{\partial z} + D_{Tl} \frac{dT}{dz} + K \frac{dh}{dz} + K \mathbf{k} \right] \\
 &= -\underbrace{[\lambda + c_l \rho_l (T - T_0)(D_{Tv} + D_{Tl})]}_{J_3} \frac{\partial T}{\partial z} \\
 &\quad - \underbrace{[\rho_l L_T D_{mv} + c_l \rho_l (T - T_0)(D_{mv} + K)]}_{J_4} \frac{dh}{dz} - \underbrace{c_l \rho_l (T - T_0) K \mathbf{k}}_{J_5}
 \end{aligned} \tag{4.A11}$$

We use  $\lambda \frac{\partial T}{\partial z}$  to represent the effective conductive heat transfer, and  $\lambda$  is highly dependent on  $\theta$  (de Vries, 1958). Using the conservation law of energy,  $\frac{\partial}{\partial t} H + \nabla \cdot q_h = 0$ , the governing equation of heat transfer is shown in Eq. [4.2].

## Appendix B

For the boundary conditions, the parameters used in Eqs. [4.9] and [4.10] can be evaluated using the following procedures (Horton and Chung, 1991)

$$R_n = (1 - \alpha_b) R_g + R_l - \epsilon \sigma (T_s + 273.16)^4 \tag{4.B1}$$

$$R_l = \sigma (T_a + 273.16)^4 [0.605 + 0.048 (1370 \rho_{va})^{0.5}] \tag{4.B2}$$

$$E = g_a (\rho_{vsurf} - \rho_{va})$$

[4.B3]

$$H_s = g_a c_{air} (T_s - T_a)$$

[4.B4]

$$G = -\lambda \left[ \frac{T_2 - T_s}{\Delta z} \right] + (T_s - T_1) C_s \frac{\Delta z}{2\Delta t}$$

[4.B5]

$$g_a = \frac{0.16 u_a}{[\ln(2.0/z_0)]^2}$$

[4.B6]

where  $R_l$  ( $W m^{-2}$ ) is the longwave sky irradiance;  $\alpha_b$  is the soil surface albedo;  $\epsilon$  is the soil surface emissivity;  $\sigma = 5.67 \times 10^{-8} W m^{-2} K^{-4}$  is the Stefan-Boltzmann constant;  $\rho_{vsurf}$  ( $kg m^{-3}$ ) is the  $\rho_v$  at the soil surface, following Eq. [4.A2], with the measured values of  $T_a$  and  $RH_a$ ;  $\rho_{va}$  ( $kg m^{-3}$ ) is the  $\rho_v$  in the atmosphere;  $g_a$  ( $m s^{-1}$ ) is the surface water vapor conductance;  $c_{air}$  ( $J m^{-3} ^\circ C^{-1}$ ) is the volumetric specific heat of air; and  $z_0$  (m) is the roughness length. We follow Horton and Chung (1991) for the calculation of  $G$ , using the discretized form with  $T_s, T_1, T_2$  ( $^\circ C$ ) representing soil temperature at the surface and the first and second layers in the computing grid, and  $\Delta t$  (s),  $\Delta z$  (m) are the time and spatial steps. The estimations of  $\alpha_b$  and  $\epsilon$  are (van Bavel and Hillel, 1976),

$$\alpha_b = \begin{cases} 0.35 - \theta & \text{if } 0.10 < \theta < 0.25 \\ 0.10 & \text{if } 0.25 < \theta \\ 0.25 & \text{if } \theta < 0.10 \end{cases}$$

[4.B7]

$$\epsilon = 0.9 + 0.18\theta$$

[4.B8]

## CHAPTER 5. A TWO-DIMENSIONAL SIMULATION OF WATER VAPOR DIODES

A paper to be submitted to Vadose Zone Journal

Zhuangji Wang<sup>1\*</sup>, Mark Ankeny<sup>2</sup>, Robert Horton<sup>1</sup>

1. Dept. of Agronomy, Iowa State University, Ames, IA, 50011

2. 156 Harvest Run Drive, Idaho Falls, Idaho 83404

Corresponding author: Zhuangji Wang, [cauwzj@gmail.com](mailto:cauwzj@gmail.com).

### Abstract

In shallow soil profiles, the diurnal temperature fluctuations lead to variations in soil thermal gradient and soil water vapor flux. The thermal gradient can be the major driving force for soil water redistribution when soil water content is relatively low. An ideal water vapor diode (WVD) is defined as a check valve that only allows water vapor flux in one direction, and a pair of ideal WVDs can be combined to trap water in a specific soil layer. A one-dimensional (1D) simulation based on coupled heat and water transfer in soil has been performed to evaluate water accumulation with WVDs. However, in order to more fully understand WVD impacts on soil, two-dimensional (2D) simulations with some real WVD designs are needed. The egg-carton WVD design was proposed by Wang et al. (2017). Here we introduce a new WVD design, with a Tyvek-Soil(Wick)-Tyvek sandwich structure. The new design can include wick bundles to enable lateral removal (drainage) of water from a soil layer where water accumulates. The geometry of the new WVD design is simple, so it can be applied easier than the egg-carton WVD design. The objective of this study is to perform 2D simulations of coupled heat and water transfer to analyze water accumulation in specific soil layers with and without WVDs, as well as to determine the influence of wick bundles on water removal. Two types of WVD are evaluated, i.e., the egg-carton design and the new design. The results show that the egg-carton WVD can accumulate water in specific soil layers. The maximum water content increase is  $0.02 \text{ m}^3 \text{ m}^{-3}$  in our example. For the new WVD design, water accumulation occurs evenly along the horizontal direction within

the WVD. A stable dry area occurs beneath the new WVD. The wick removal (drainage) of water out of soil is two times larger with WVDs than without WVDs. Thus, not only does the WVD accumulate water in a specific soil layer, but the WVD can also assist soil water removal in order to control water contents beneath the WVD. Thus, WVDs can be used to increase water contents by concentrating soil profile water, and they can be used to accelerate soil profile drying by wicking accumulated water out of the soil profile.

### **Abbreviation**

WVD: Water Vapor Diode,

### **Introduction**

Diurnal soil temperature fluctuations lead to thermal gradients in surface soil layers, which are the prime causes for subsurface water vapor fluxes, especially when soil is relatively dry and water vapor becomes the major means of water movement (Jackson et al., 1973; Jackson et al., 1974). It is possible to accumulate water from subsurface soil through thermal driven water vapor flow. For example, the solar still uses a plastic film to cover a hole in the ground. Evaporated water from the hole will condense on the plastic film. Liquid water can be collected under the plastic film (Jackson and Van Bavel, 1965; Badran et al., 2005). The solar still is originally designed as a desert survival technique, and it can be used temporarily as an alternative water supply.

The physics of a solar still is to use the plastic film to separate water vapor movement from the coupled heat and water movement. Inspired by the solar still, a soil water vapor diode (WVD) is designed to trap water vapor in a subsurface soil layer. Ideal WVDs have three properties: (1) allow water vapor flux only in one vertical direction; (2) block liquid water flow in both vertical directions; (3) allow conductive heat transfer in both vertical directions (Wang et al., 2017). A plausible design of the WVD proposed in Wang et al. (2017) uses an egg-carton shape plastic sheet, with pores situated at selected peaks and valleys. The name ‘diode’ was borrowed from electronics to describe a one-way transmission property for water vapor flow across the WVD. Thus, the WVD can trap water vapor on one side of the WVD which leads to water accumulation. Paired WVDs buried in soil can have the effect of accumulating water between the WVDs over relatively long time periods. The

effects of ideal WVDs on soil water accumulation were investigated numerically by Wang et al. (2017) with an 1D coupled heat and water transfer model.

One potential application of WVDs is to concentrate water in a specific soil layer under a road and drain away the water, such that the water content in the soil profile under the road can be maintained in a relatively low value. This is important because many road construction problems are caused by the wet conditions in the soil beneath the road. In that case, fiberglass wick bundles can be inserted in soil between the paired WVDs. The wicks can transport water quickly. Their large hydraulic conductivity can assist in draining soil water laterally away from the water accumulated soil. The egg-carton WVD has a relatively complicated shape, and 1D simulations do not fully capture the effects of WVDs. In order to better estimate soil water accumulation and subsurface drainage with WVDs, the geometric configuration of WVDs should be taken into account and a 2D simulation is necessary. WVDs should be inserted into the soil horizontally at specific depths, which is not easy for real applications, especially with the egg-carton design. Thus, there is a need to improve WVD design. A Tyvek-Soil(Wick)-Tyvek structure can be used as an alternative design for the WVD. The two flat Tyvek (Dupont Inc, IA) layers allow water vapor flux but block liquid water flow. Soil and fiberglass wick bundles are used to filled in the space between the two Tyvek layers where soil water will accumulate. The Tyvek-Soil(Wick)-Tyvek can be pre-constructed for easy placement for field applications. The performance of this new WVD design must be evaluated. Thus, the objective of this study is to perform 2D numerical simulations to evaluate the water accumulation with the egg-carton WVD design and with the new WVD design. The effects of WVD on draining water from the water accumulated soil layer will also be calculated and compared to water drainage from soil profiles without a WVD and a numerical application of new WVD is shown for road construction.

## **Materials and Methods**

### **(i) Two Water Vapor Diode Designs**

The egg-carton shaped WVD, with pores situated at selected peaks and valleys, is the original WVD design in Wang et al. (2017). The geometric configuration enables the function of such WVDs. Figure 5.1-a presents two egg-carton WVDs, while Fig 5.1-b shows

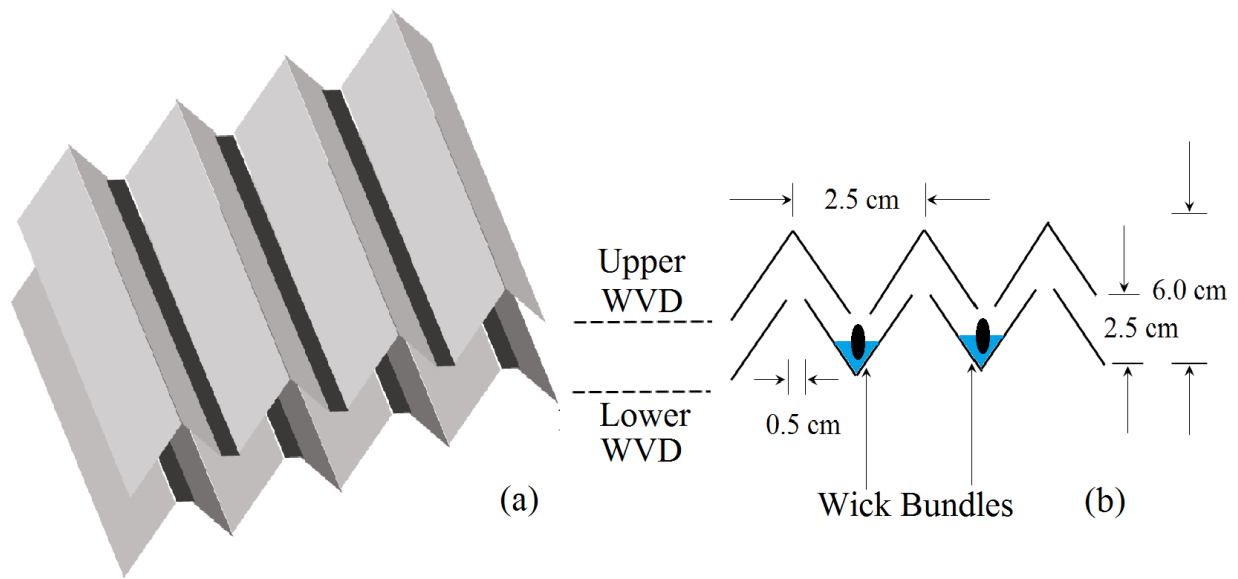


Fig. 5.1. The egg-carton WVD design. (a) The 3D view of paired WVDs, with the dark strips indicating the openings; (b) a cross-sectional view of the geometric configuration of paired WVDs.

the cross-sectional configuration of the WVDs. During the day time, the soil thermal gradient is downward, and water vapor moves downwards following soil thermal gradient. Water vapor can enter the upper diode through the pores, reach the bottom of the indentation, and condense in the cups of the lower WVD. During the night time, the soil thermal gradient is upwards, and water vapor moves upwards in the soil profile. The water vapor from beneath a WVD will be funneled through the lower WVD but stopped by the upper WVD. The water vapor stopped by the upper WVD will condense and flow into the cups of the lower WVD, similar to the water accumulation with the solar still. Thus, during a diurnal temperature fluctuation, water will accumulate in the soil layer between the two WVDs, especially in the cups of the lower diode, which is shown with the blue color in Fig. 5.1-b.

A new WVD design has a sandwich structure consisting of Tyvek-Soil(Wick)-Tyvek. Figure 5.2 presents an example placement of a new 5-cm thick WVD in a 25-cm soil profile. In this new design, Tyvek is an olefin sheet product, which is durable, tough and chemically resistant. An important property of Tyvek is that water vapor can transmit through it, but liquid water cannot move across a Tyvek sheet (DuPont, 2002). Between the two Tyvek



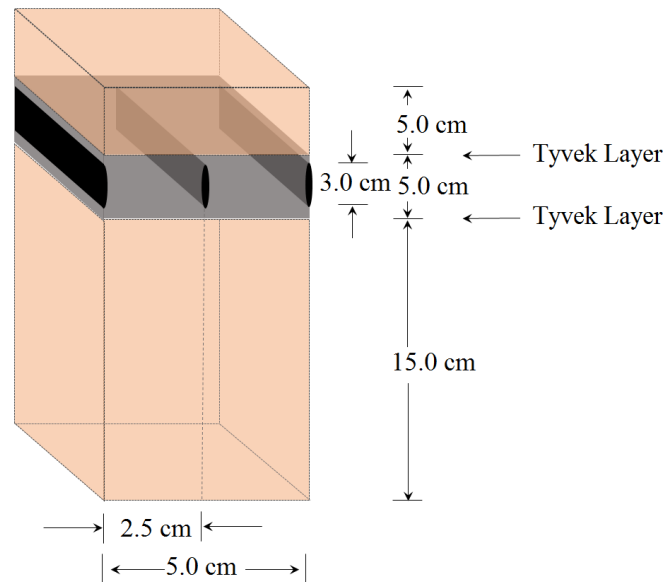


Fig. 5.2. The new WVD design embedded in a 25-cm soil profile. The light gray section shows the Tyvek-Soil(Wick)-Tyvek structure and the dark gray sections indicate the fiberglass wick bundles within the WVD layer.

layers, the WVD is filled with soil and fiberglass wicks. The wicks have been used to assist water infiltration or liquid sampling from unsaturated soils in previous studies (Knutson and Selker, 1994; Rimmer et al., 1995). In the new WVD, wicks are arranged as bundles to assist water movement laterally out of the soil profile. Bundles are shown as the dark gray tubes within the WVD. However, based on the water retention properties, the water holding ability of a wick is much smaller than that for a soil (Knutson and Selker, 1994). Thus, the soil between the two Tyvek layers helps to hold the water in the WVD when the ambient soil layers are relatively dry. The soil can be substituted by other porous materials with similar water holding properties. The advantages of the new design over the egg-carton design are (1) the new WVD is flat and (2) the new WVD can be pre-constructed and deployed directly in soil. Thus, applications of the new WVD are easier than those for the original egg-carton shaped WVD.

Table 5.1. Soil property values.

Soil	Textural fractions			organic matter	$\rho_b$ ( $Mg\ m^{-3}$ )
	Sand	Silt	Clay	— % —	
	— % —				
Silt loam	2	73	25	4.4	1.20
Soil	Hydraulic parameters				
	$\Psi_e$ (m)	$b$	$\theta_s$ ( $m^3\ m^{-3}$ )	$K_s$ ( $m\ s^{-1}$ )	
Silt loam	-0.13	6.53	0.55	$3.80 \times 10^{-7}$	
Soil	Thermal conductivity parameters				
	$b_1$	$b_2$	$b_3$		
Silt loam	-0.95	-4.31	6.00		

The new WVD design does not satisfy the three basic WVD properties, since the Tyvek allows water vapor flux in both vertical directions. Thus, the new WVD is a weak WVD. For that reason, the physics of the new WVD design is different from the original egg-carton WVD design. The idea of the new design is to separate water vapor flow from liquid water flow. When the soil thermal gradient is upward, water vapor will propagate upwards and cross the lower Tyvek sheet, entering the soil and wick between the two Tyvek sheets. Although some of the water vapor will also leak out of the upper Tyvek sheet, the amount of leakage is smaller than the water entering through the lower Tyvek sheet, because the temperature at the upper Tyvek sheet is smaller than that of the lower Tyvek sheet. Part of the water vapor entering through lower sheet is condensed, and it stays within the WVD. Similar results occur with downward soil thermal gradients, and the net effect of this design is that water will be concentrated in the WVD.

## (ii) Soil Physical Properties

In this study, properties of Ida silt loam (fine-silty, mixed, superactive, calcareous, mesic Typic Udorthents) are used for the numerical simulations. The physical properties of the Ida silt loam are reported by Heitman et al. (2007). The soil water retention curve has the form (Campbell, 1974)

$$h = h_e \left( \frac{\theta}{\theta_s} \right)^{-b}$$

[5.1]

Table 5.2. The fiberglass wick properties.

Wick	Textural fractions				
	Diameter (m)	Fiber Radius (m)	Filament Tortuosity	Bulk Density (kg m <sup>-3</sup> )	Porosity
MM 1/2 MAT	0.0126	4.5×10 <sup>-6</sup>	0.19	700	0.73
Wick	Hydraulic Conductivity				
	K <sub>sat</sub> (m s <sup>-1</sup> )		a (m <sup>-1</sup> )		
MM 1/2 MAT	6.11×10 <sup>-4</sup>		6.4		
Wick	θ <sub>s</sub> *1	θ <sub>r</sub> *2	Water Retention Curve		
	—— (m <sup>3</sup> m <sup>-3</sup> ) ——		α (m <sup>-1</sup> )	<i>n</i>	<i>m</i>
MM 1/2 MAT	0.69	0	0.55	1.124	2.229

\*1 The saturated water content of wick.

\*2 The residual water content of wick.

where  $h_e$  (m) and  $b$  are empirical parameters,  $h$  (m) is soil water matric potential;  $\theta$  (m<sup>3</sup> m<sup>-3</sup>) is the volumetric water content and  $\theta_s$  (m<sup>3</sup> m<sup>-3</sup>) is the saturated water content. The hydraulic conductivity ( $K$ , m s<sup>-1</sup>) follows the equation (Campbell, 1974)

$$K = \frac{\mu(T_0)}{\mu(T)} \left( \frac{\theta}{\theta_s} \right)^{2b+3} K_s$$

[5.2]

where  $K_s$  (m s<sup>-1</sup>) is the saturated hydraulic conductivity at reference temperature ( $T_0$ , °C);  $\mu$  (m<sup>2</sup> s<sup>-1</sup>) is the dynamic viscosity of liquid water;  $T$  (°C) is the soil temperature. The soil bulk heat capacity,  $C_s$  (J m<sup>-3</sup> °C<sup>-1</sup>), is expressed as the weighted average of the specific heat of soil solid, liquid and gas (Kluitenberg, 2002),

$$C_s = \rho_b(c_o\phi_o + c_m\phi_m) + c_g\rho_g\theta_g + c_l\rho_l\theta$$

[5.3]

where  $\rho_b$  (kg m<sup>-3</sup>),  $\rho_g$  (kg m<sup>-3</sup>) and  $\rho_l \approx 1000$  kg m<sup>-3</sup> are the soil bulk density, gas density and liquid water density;  $c_o$  (J kg<sup>-1</sup> °C<sup>-1</sup>),  $c_m$  (J kg<sup>-1</sup> °C<sup>-1</sup>),  $c_g$  (J kg<sup>-1</sup> °C<sup>-1</sup>) and  $c_l$  (J kg<sup>-1</sup> °C<sup>-1</sup>) are the specific heats of organic matter, minerals, soil gas and water;

$\phi_0$  (kg kg<sup>-1</sup>) and  $\phi_m$  (kg kg<sup>-1</sup>) are organic fraction and mineral fraction;  $\theta_g$  (m<sup>3</sup> m<sup>-3</sup>) is the soil gas fraction. The soil thermal conductivity  $\lambda$  (W m<sup>-1</sup> °C<sup>-1</sup>) versus water content function follows Horton and Chung (1991),

$$\lambda = b_1 + b_2\theta + b_3\theta^{0.5} \quad [5.4]$$

where the parameter values  $b_1, b_2, b_3$  are listed in Table 5.1.

The wick used in this study is MM 1/2 MAT (Mid-Mountain 1/2 inch matrix braid). The hydraulic conductivity of the wick follows the modified exponential equation (Rijtema, 1965; Knutson and Selker, 1994)

$$K = K_s \exp(ah). \quad [5.5]$$

The water retention curve of the wick follows the van Genuchten (1980) equation

$$\frac{\theta - \theta_r}{\theta_s - \theta_r} = \frac{1}{[1 + (\alpha|h|)^n]^m} \quad [5.6]$$

where  $\theta_r$  (m<sup>3</sup> m<sup>-3</sup>) is the residual water content, which is 0 for the MM 1/2 MAT wick. The model parameters of Eqs. [4.5] and [4.6] are shown in Table 5.2.

We remark here that if water accumulation without drainage is desired, the wick is not included for the original and new WVD. In the following simulation, we assume the wick is used only when drainage is considered.

### (iii) 2D Simulation Methods

Coupled heat and water transfer models are widely used for liquid and vapor movement simulations over various soil types (Nassar and Horton, 1989a; Nassar and Horton, 1997; Heitman et al., 2008, Bittelli et al., 2008). This model is used for simulating the soil water redistribution examples in our study. The governing equations for water and heat transfer are derived from the conservation of soil water and the conservation of soil heat (Philip and de Vries, 1957; Milly, 1982; Nassar and Horton, 1997). Liquid water transfer and water vapor transfer occur in response to water potential gradients and temperature gradients (Nassar and Horton, 1989b). Conduction, convection, latent heat transfer, and heat of wetting are

included in the heat transfer equation (Milly, 1982; Nassar and Horton, 1997). The liquid water and vapor phases are assumed to have local equilibrium.

$$\mathcal{H}_1 \frac{\partial h}{\partial t} + \mathcal{H}_2 \frac{\partial T}{\partial t} = \nabla \cdot \left[ \mathcal{H}_3 \frac{\partial h}{\partial z} + \mathcal{H}_4 \frac{\partial T}{\partial z} + K \mathbf{k} \right] \quad [5.7]$$

$$\mathcal{T}_1 \frac{\partial T}{\partial t} + \mathcal{T}_2 \frac{\partial h}{\partial t} = \nabla \cdot \left[ \mathcal{T}_3 \frac{\partial T}{\partial z} + \mathcal{T}_4 \frac{\partial h}{\partial z} + \mathcal{T}_5 \mathbf{k} \right] \quad [5.8]$$

In this model,  $\theta$  is connected to  $h$ , following the water retention curve;  $t$  (s) is time; and  $z$  (m) represents the depth.  $\mathcal{H}_1, \mathcal{H}_2, \mathcal{H}_3, \mathcal{H}_4$  are abbreviations for soil hydraulic properties, which include the hydraulic conductivity, water diffusivity, and specific water capacity; while  $\mathcal{T}_1, \mathcal{T}_2, \mathcal{T}_3, \mathcal{T}_4, \mathcal{T}_5$  are abbreviations for soil thermal properties. The derivation of those properties is provided in Wang et al. (2017).

In the simulation examples, a 25-cm deep soil profile is considered. The horizontal dimension of the soil profile is  $X = 10$  cm. The egg-carton WVDs and new WVD design are inserted in shallow soil layers. For the egg-carton WVDs, the peaks of the upper diode are at a depth of 5 cm, while the valleys of the lower diode are at a depth of 10 cm. The new WVD layer is 5-cm thick, and when placed in the soil profile, the central depth is 7.5 cm. The initial water content of the soil profile is set as  $0.15 \text{ m}^3 \text{ m}^{-3}$  ( $\sim -60$  bar), which is lower than the permanent wilting point of the soil ( $\sim 0.18 \text{ m}^3 \text{ m}^{-3}$ ). For simplicity, Dirichlet boundary conditions are used for water content and temperature. The water content at a depth of 25 cm is fixed at  $0.17 \text{ m}^3 \text{ m}^{-3}$  ( $\sim -27$  bar), while the water content at the soil surface is set as  $0.10 \text{ m}^3 \text{ m}^{-3}$  ( $\sim -850$  bar). The temperature of the lower boundary is  $30^\circ\text{C}$ , and at the upper boundary, the temperature varies as a sine curve, ranging from  $10^\circ\text{C}$  to  $50^\circ\text{C}$ . For actual applications, the initial and boundary conditions can be set as measured values. Besides water accumulation, an aim of the WVD is to assist with subsurface drainage via the wicks. The threshold for the wicks to begin draining water is  $0.15 \text{ m}^3 \text{ m}^{-3}$ , i.e., if  $\theta$  is lower than  $0.15 \text{ m}^3 \text{ m}^{-3}$ , no drainage will occur; otherwise, the water will drain until the  $\theta$  is equal to  $0.15 \text{ m}^3 \text{ m}^{-3}$ .

## Results and Discussion

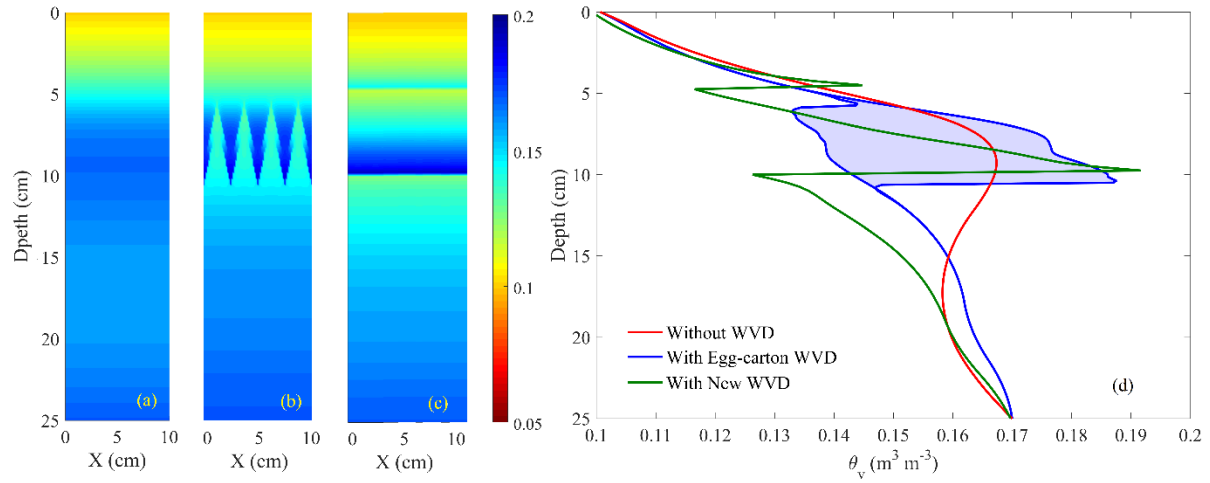


Fig. 5.3. The 2D simulation of coupled heat and water movement in soil with and without WVDs. (a) shows the soil water distribution without WVDs; (b) is the soil water distribution with paired egg-carton WVDs; (c) is the soil water distribution with a new WVD; (d) presents the water content with respect to depth, and the blue lines and the light blue area show the range of water contents along the horizontal direction (X).

The first example compares the water accumulation of the two WVD designs with the soil water distribution without the WVD. The simulation results are shown in Fig. 5.3. Fig. 5.3-a presents the soil water distribution without a WVD. For the egg-carton WVDs, water is concentrated in the soil between the two WVDs (Fig. 5.3-b), and for the new WVD, water accumulated in the WVD layer near the lower Tyvek (Fig. 5.3-c). A vertical cross-section of water distribution is shown in Fig. 5.3-d. The red curve shows  $\theta$  with respect to depth in a soil profile without WVDs, indicating the soil water redistribution under temperature fluctuations. The blue lines and the light blue area show the range of  $\theta$  along X due to the geometric configuration of the egg-carton WVDs. The largest  $\theta$  between the WVDs is  $0.02 \text{ m}^3 \text{ m}^{-3}$  larger than the  $\theta$  without WVDs; and the smallest  $\theta = 0.135 \text{ m}^3 \text{ m}^{-3}$ . The green curve represents the vertical  $\theta$  distribution with the new WVD. From the comparisons, some drawbacks of the egg-carton design are observed. First, the accumulated water, which is right below the openings of the upper diode, does not diffuse quickly in the soil between the two

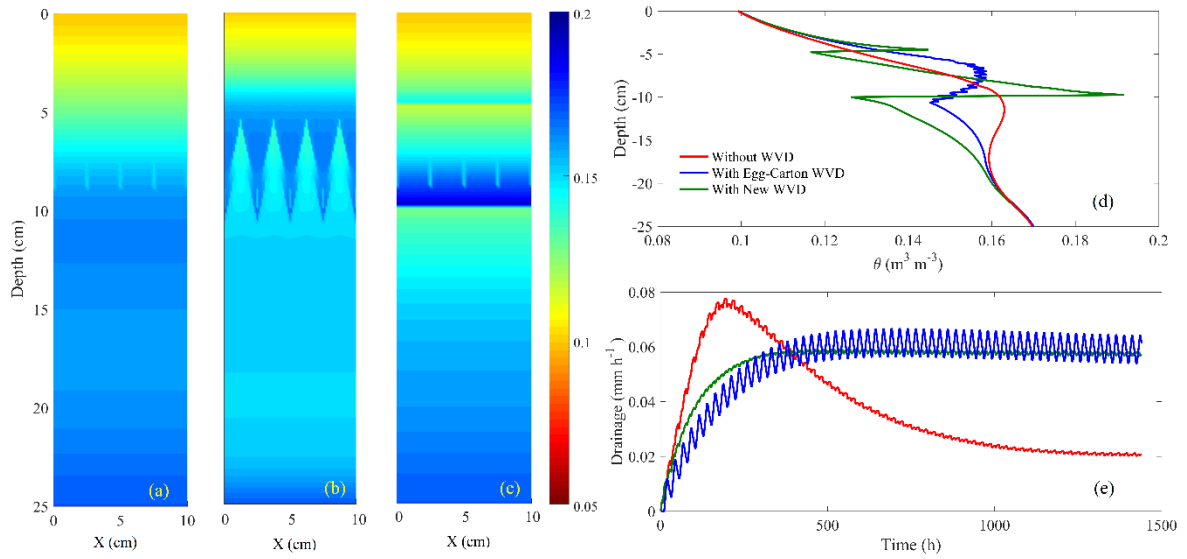


Fig. 5.4. The 2D simulation of coupled heat and water movement in soil with fiberglass wick bundles. (a) shows the soil water distribution without WVDs; (b) is the soil water distribution with egg-carton WVDs; (c) is the soil water distribution with a new WVD; (d) presents the soil water content with respect to depth, averaged along the X direction; and (e) presents the drainage flux from the wicks in the WVD layer.

WVDs. This can block the downwards water vapor flux through the openings, making water stay in the valleys of the upper diode. When the temperature gradient is upwards, the water that is trapped between the WVDs can easily move upwards and out of the soil layers between the two WVDs. Second, relatively dry regions develop below the peaks of the upper diode, and above the openings of the lower diode. These dry regions, having small water diffusivity, may also slow the upwards movement of water vapor into the soil layer between the WVDs. Thus, the actual effects of the egg-carton WVD do not strictly satisfy the three properties of ideal WVD, and those two drawbacks will reduce the efficiency of the WVDs. For the new WVD design, which is not uni-directional for water vapor, water accumulates from dynamic water inflow and leakage. Thus, the water accumulating efficiency of the new WVD also has some limitations due to leakage. One way to keep a positive net flux of soil water moving into the soil layer between the egg-carton WVDs or the Tyvek sheets is to incorporate a sink in the soil layer in order to remove some of the accumulated water. In our

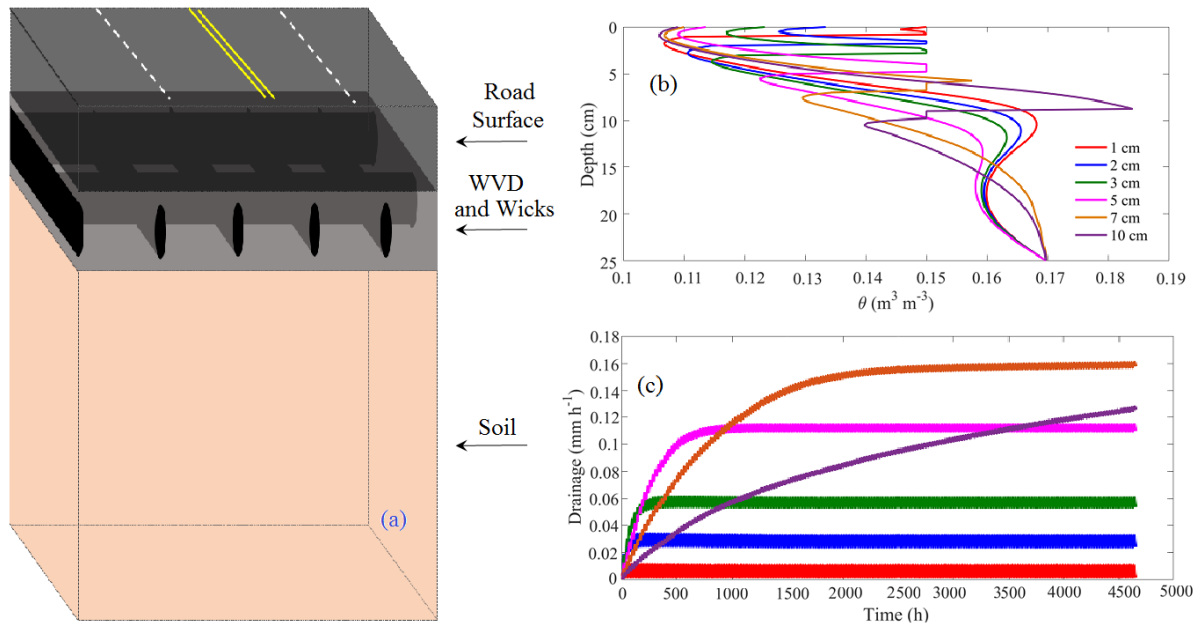


Fig. 5.5 An example application of the new WVD under a road surface. (a) shows the WVD placement for this application; (b) is the water content distribution under the road surface; (c) is the drainage flux from the wicks.

examples, fiberglass wick bundles are used as the sinks to assist the lateral removal (drainage) of water from the WVD soil layer.

In the second example, the effects of the original egg-carton WVD and the new WVD on water drainage from soil layers are evaluated. The example provides a comparison of  $\theta$  with and without WVDs, which include wick bundle sinks as indicated in Fig. 5.1 and Fig. 5.2. Water removal fluxes are also calculated. Figure 5.4-a shows the  $\theta$  distribution in the case of having a wick sink for lateral water removal, but without the presence of a WVD. Figure 5.4-b presents  $\theta$  for the original egg-carton WVD with wick bundles. The  $\theta$  for the new WVD with wick bundles is shown in Fig. 5.4-c. The horizontally averaged  $\theta$  is shown in Fig. 5.4-d, with respect to depth. Figure. 5.4-e shows the lateral water drainage values for each soil condition. For the original and the new WVD conditions, the stable drainage rate is two times larger than the drainage rate for the condition of a soil without a WVD. These results indicate that WVDs can assist in soil profile drying and that a relatively dry zone develops beneath the WVD. The original egg-carton WVDs and the new WVD provided similar performances



based on the numerical simulations. The new WVD has a simpler geometry than the egg-carton WVD, so it may be easier to install in actual field settings.

Fig. 5.5 shows an example placement of the newly designed WVD under a road surface. The WVD is shown to attach to the underside of the road surface, so that as water is removed by wick bundles in the WVD, a dry soil zone can form just beneath the WVD (Fig. 5.5-a). The road surface is assumed to be impermeable to liquid water and water vapor. In a series of numerical simulations, WVDs of a range of thicknesses (1-cm, 2-cm, 3-cm, 5-cm, 7-cm and 10-cm) are investigated. In each case wick bundles are placed in the WVD just above the lower Tyvek layer, where water is expected to accumulate. Fig. 5.5-b shows the  $\theta$  distributions in the WVDs and soil profiles beneath the road surface for six WVD cases, while Fig. 5.5-c presents the lateral rates of soil water removal through the fiberglass wick bundles. From the lateral drainage results, as the WVD layer thickens, the stable drainage rate increases, but the time to reach the stable state also increases. The maximum water removal rate by the end of the simulation occurs for the 7-cm thick WVD. After 4500 h of simulation, the trend for the 10-cm thick WVD is still increasing. Thus, the best selection of the WVD in this example could be either the 7-cm thick WVD or the 10-cm thick WVD, depending on how one balances the drainage rate and the time needed to reach the stable state. In real application, the desirable WVD thickness may also vary with actual soil and weather conditions, and site-specific numerical studies are recommended.

## Summary

A WVD is defined as a uni-directional water vapor barrier, which blocks liquid water flow and allows conductive heat transfer in both vertical directions. In this study, we use a 2D numerical simulation to study water accumulation in a selected soil profile layer caused by WVDs. Two WVD designs are included, the original egg-carton design and the new Tyvek-Soil(Wick)-Tyvek design. The physics of these two designs are discussed and numerical results based on assumed initial and boundary conditions are presented. The maximum water content with two WVD designs is roughly  $0.02 \text{ m}^3 \text{ m}^{-3}$  larger than the soil water content without WVDs. The low efficiency of water accumulation is because the designs do not fully satisfy the requirements of fully functioning WVDs. Fiberglass wick bundles can be inserted directly into soil layers without WVD to drain the water laterally

from the soil profile. The drainage rates for wicks placed within a WVD are two times larger than those for wicks without a WVD. The egg-carton WVD has a relatively complicated geometrical shape, and the pair of WVDs should be put in soil at specific depths. However, the newly designed WVD is flat and can be preconstructed as one intact fabric membrane. Thus, the new WVD can be placed easily in a foundation during road construction.

The dimensions and placement depths of the WVD can be adjusted to adaptive to local soil and weather conditions. An application example for a road foundation is discussed, and numerical simulation is recommended to evaluate the WVD effects before application. The study of the real applications is important to evaluate the actual performance of the WVD in soil, where the initial and boundary conditions for real applications can be based on measured values. Actual physical deployment of WVDs will be evaluated in future studies.

### **Acknowledgements**

This work was supported by the National Science Foundation under Grant 1623806, USDA-NIFA, Multi-State Project 3188, Iowa State University Department of Agronomy, the Hatch Act, and State of Iowa funds.

### **References**

- Badran, A.A., A.A. Al-Hallaq, I.A. Eyal Salman and M.Z. Odat. (2005). "A solar still augmented with a flat plate collector." *Desalination*. 172:227–234. doi: 10.1016/j.desal.2004.06.203.
- Bittelli, M., F. Ventura, G.S. Campbell, R.L. Snyder, F. Gallegati and P.R. Pisa. (2008). "Coupling of heat, water vapor, and liquid water fluxes to compute evaporation in bare soils." *J. Hydrol.* 362: 191-205. <http://dx.doi.org/10.1016/j.jhydrol.2008.08.014>
- Campbell, G.S. (1974). "A simple method for determining unsaturated conductivity from moisture retention data." *Soil Sci.* 117: 311-314. doi: 10.1097/00010694-197406000-00001.
- de Vries, D.A. (1958). "Simultaneous Transfer of Heat and Moisture in Porous Media." *Trans. Am. Geophys. Union*. 39: 909–916. doi/10.1029/TR039i005p00909.
- DuPont. 2002. Product Handbook for DuPont Tyvek. [http://www.dupont.com/content/dam/dupont/products-and-services/fabrics-fibers-and-nonwovens/industrial-fabrics/documents/DPT\\_Tyvek\\_Product\\_Handbook.pdf](http://www.dupont.com/content/dam/dupont/products-and-services/fabrics-fibers-and-nonwovens/industrial-fabrics/documents/DPT_Tyvek_Product_Handbook.pdf)
- Heitman, J. L., R. Horton, T. Ren, I. N. Nassar and D. D. Davis. (2008). "A Test of Coupled Soil Heat and Water Transfer Prediction under Transient Boundary Temperatures." *Soil Sci. Soc. Am. J.* 72:1197-1207. doi:10.2136/sssaj2007.0234.

- Horton, R. and S. Chung. (1991). "Soil Heat Flow. Modeling Plant and Soil Systems." 397-438. doi:10.2134/agronmonogr31.c17.
- Jackson R.D., B.A. Kimball, R.J. Reginato and F.S. Nakayama. (1973). "Diurnal Soil-Water Evaporation: Time-Depth-Flux Patterns." *Soil Sci. Soc. Amer. Proc.* 37: 505-509. doi:10.2136/sssaj1973.03615995003700040014x.
- Jackson, R. D., R. J. Reginato, B. A. Kimball, and F. S. Nakayama. (1974). "Diurnal Soil-Water Evaporation: Comparison of Measured and Calculated Soil-Water Fluxes." *Soil Sci. Soc. Amer. Proc.* 38:861-866. doi:10.2136/sssaj1974.03615995003800060012x.
- Jackson R.D. and C.H.M. van Bavel. (1965). "Solar Distillation of Water from Soil and Plant Materials: A Simple Desert Survival Technique." *Science*. 149:1377-1379. PMID: 5826532.
- Kluitenberg, G.J. (2002). "Heat capacity and specific heat. Methods of soil analysis." *Part 4. Physical Methods*. 1201–1208. doi:10.2136/sssabookser5.4.c49.
- Knutson, J.H. and Selker, J.S. (1994). "Unsaturated Hydraulic Conductivities of Fiberglass Wicks and Designing Capillary Wick Pore-Water Samplers." *Soil Sci. Soc. Am. J.* 58:721-729. doi:10.2136/sssaj1994.03615995005800030012x
- Milly, P.C.D. (1982). "Moisture and Heat Transport in Hysteretic, Inhomogeneous Porous Media: A Matric Head-Based Formulation and a Numerical Model." *Water Resour. Res.* 18:489- 498. doi: 10.1029/WR020i008p01087.
- Nassar, I. N. and R. Horton. (1989a). "Water transport in unsaturated nonisothermal salty soil: I. Experimental results." *Soil Sci. Soc. Am. J.* 53:1323-1329. doi:10.2136/sssaj1989.03615995005300050004x.
- Nassar, I.N. and R. Horton. (1989b). "Water transport in unsaturated nonisothermal salty soil: II. Theoretical development." *Soil Sci. Soc. Am. J.* 53:1330–1337. doi:10.2136/sssaj1989.03615995005300050005x.
- Nassar, I.N. and R. Horton. (1997). "Heat, water, and solute transfer in unsaturated porous media: I. Theory development and transport coefficient evaluation." *Trans. in Porous Media*. 27:17-38. doi:10.1023/A:1006583918576.
- Philip J.R. and D.A. de Vries. (1957). "Moisture Movement in Porous Materials under Temperature Gradients." *Trans. Am. Geophys. Union*. 38:222–232. doi:10.1029/TR038i002p00222.
- Rijtema, P. E. (1965). "An analysis of actual evapotranspiration. Rep 659." Center for Agricultural Publications and Documentation. PUDOC, Wageningen, the Netherlands.
- Rimmer, A., Steenhuis, T. S. and Selker, J. S. (1995). "One-Dimensional Model to Evaluate the Performance of Wick Samplers in Soils." *Soil Sci. Soc. Am. J.* 59:88-92. doi:10.2136/sssaj1995.03615995005900010013x.

- van Bavel, C.H.M and D.I. Hillel. (1976). "Calculating Potential and Actual Evaporation from a Bare Soil Surface by Simulation of Concurrent Flow of Water and Heat." *Agric. Meteorol.* 17: 453– 476. [http://dx.doi.org/10.1016/0002-1571\(76\)90022-4](http://dx.doi.org/10.1016/0002-1571(76)90022-4).
- van Genuchten, M. T. (1980). "A Closed-form Equation for Predicting the Hydraulic Conductivity of Unsaturated Soils." *Soil Sci. Soc. Am. J.* 44:892-898.  
doi:10.2136/sssaj1980.03615995004400050002x
- Wang, Z., Ankeny, M and Horton, R. (2017). "The Impact of Water Vapor Diodes on Soil Water Redistribution." Submitted to *J. Hydrol.*

## CHAPTER 6. GENERAL CONCLUSIONS

This chapter is used to give a general conclusion of numerical methods on TDR waveforms analysis and the effect of water vapor diode on soil water redistribution and accumulation.

The key findings of this research are shown as follows,

1. TLBMO is an effective and stable operator to determine the  $t_2$  values in TDR waveforms, especially TDR waveforms measured with short TDR probes.
2. The TLBMO method provides more plausible results than do tangent line methods for some short-TDR waveforms.
3. Although the second order BMO and AWIGF methods perform well on both long probe and short probe TDR waveforms, a CPF filter improves the performance of AWIGF in some short probe TDR waveforms.
4. One-dimensional simulations show the WVD effect on soil water redistribution.
5. Two-dimensional simulations with WVD demonstrate that water accumulated in specific soil layers, and the effect of WVDs on assisting laterally water drainage from the water accumulated region.

The following recommendations are provided for future studies:

1. The second order BMO method should be investigated for its abilities to determine soil water content distributions along the TDR probes.
2. Actual field application should be performed to verify the effects of WVDs to accumulate water in specific soil layers.

## APPENDIX: NUMERICAL SCHEMES FOR CHAPTER 4 AND CHAPTER 5

### Numerical Scheme for Chapter 4

In chapter 4, an implicit scheme is used to discretize Eqs. [4.1] and [4.2], i.e.

$$\begin{aligned} \mathcal{H}_1 \frac{h_i^{t+1} - h_i^t}{\Delta t} + \mathcal{H}_2 \frac{T_i^{t+1} - T_i^t}{\Delta t} \\ = \mathcal{H}_3 \frac{h_{i+1}^{t+1} + h_{i-1}^{t+1} - 2h_i^{t+1}}{\Delta Z^2} + \mathcal{H}_4 \frac{T_{i+1}^{t+1} + T_{i-1}^{t+1} - 2T_i^{t+1}}{\Delta Z^2} + \frac{K_{i+1}^t - K_{i-1}^t}{\Delta Z} \end{aligned} \quad [A1]$$

$$\begin{aligned} \mathcal{J}_1 \frac{T_i^{t+1} - T_i^t}{\Delta t} + \mathcal{J}_2 \frac{h_i^{t+1} - h_i^t}{\Delta t} \\ = \mathcal{J}_3 \frac{T_{i+1}^{t+1} + T_{i-1}^{t+1} - 2T_i^{t+1}}{\Delta Z^2} + \mathcal{J}_4 \frac{h_{i+1}^{t+1} + h_{i-1}^{t+1} - 2h_i^{t+1}}{\Delta Z^2} + \frac{(\mathcal{J}_5)_{i+1}^t - (\mathcal{J}_5)_{i-1}^t}{\Delta Z} \end{aligned} \quad [A2]$$

Rearranging the two equations, a linear equation system can be constructed in order to solve for temperature  $T^{t+1}$  and matric potential  $h^{t+1}$ , i.e.,

$$\begin{aligned} \mathcal{H}_3 \frac{\Delta t}{\Delta Z^2} h_{i+1}^{t+1} - \left( 2\mathcal{H}_3 \frac{\Delta t}{\Delta Z^2} + \mathcal{H}_1 \right) h_i^{t+1} + \mathcal{H}_3 \frac{\Delta t}{\Delta Z^2} h_{i-1}^{t+1} + \mathcal{H}_4 \frac{\Delta t}{\Delta Z^2} T_{i+1}^{t+1} \\ - \left( 2\mathcal{H}_4 \frac{\Delta t}{\Delta Z^2} + \mathcal{H}_2 \right) T_i^{t+1} + \mathcal{H}_4 \frac{\Delta t}{\Delta Z^2} T_{i-1}^{t+1} \\ = -\mathcal{H}_1 h_i^t - \mathcal{H}_2 T_i^t - \frac{K_{i+1}^t - K_{i-1}^t}{\Delta Z} \Delta t \\ \mathcal{J}_3 \frac{\Delta t}{\Delta Z^2} T_{i+1}^{t+1} - \left( 2\mathcal{J}_3 \frac{\Delta t}{\Delta Z^2} + \mathcal{J}_1 \right) T_i^{t+1} + \mathcal{J}_3 \frac{\Delta t}{\Delta Z^2} T_{i-1}^{t+1} + \mathcal{J}_4 \frac{\Delta t}{\Delta Z^2} h_{i+1}^{t+1} \\ - \left( 2\mathcal{J}_4 \frac{\Delta t}{\Delta Z^2} + \mathcal{J}_2 \right) h_i^{t+1} + \mathcal{J}_4 \frac{\Delta t}{\Delta Z^2} h_{i-1}^{t+1} \\ = -\mathcal{J}_1 T_i^t - \mathcal{J}_2 h_i^t - \frac{(\mathcal{J}_5)_{i+1}^t - (\mathcal{J}_5)_{i-1}^t}{\Delta Z} \Delta t \end{aligned} \quad [A3]$$

The equation systems in Eq. [A3] for  $i = 0, 1, 2, \dots, n$  consists of  $2(n + 1)$  equations. In this study, a MATLAB built-in solver “/” was used for the linear system, and it followed the generalized minimal residual (GMRES) model.

In order to determine the coefficients  $\mathcal{H}_1, \mathcal{H}_2, \mathcal{H}_3, \mathcal{H}_4, K, \mathcal{T}_1, \mathcal{T}_2, \mathcal{T}_3, \mathcal{T}_4, \mathcal{T}_5$ , a Picard iteration was used. Suppose at time-step  $t$ , the simulation needed to calculate  $h$  and  $T$  at time-step  $t + 1$ . The coefficients were first determined using  $h^t$  and  $T^t$  values. Then, a temporary  $h^*$  and  $T^*$  could be determined from the equation system Eq. [A3]. Then, the coefficients were calculated using  $h^*$  and  $T^*$  again, and a new  $h^*$  and  $T^*$  were determined with the new coefficient values. If the  $h^*$  and  $T^*$  converged, the numerical simulation moved to the next step  $t + 1$ . Otherwise, the iteration would be continued. In this study, if the Picard iteration did not converge in 10 iterations, then the simulation would return to time  $t$ , and the time step  $\Delta t$  would be cut into half, and a new Picard iteration would start from the time-step  $t$  with the new time-step.

### Numerical Scheme for Chapter 5

In chapter 5, an implicit scheme is used to discretize the governing equation in a 2D computational domain, i.e.

$$\begin{aligned}
 & \mathcal{H}_1 \frac{h_{i,j}^{t+1} - h_{i,j}^t}{\Delta t} + \mathcal{H}_2 \frac{T_{i,j}^{t+1} - T_{i,j}^t}{\Delta t} \\
 &= \mathcal{H}_3 \left( \frac{h_{i+1,j}^{t+1} + h_{i-1,j}^{t+1} - 2h_{i,j}^{t+1}}{\Delta x^2} + \frac{h_{i,j+1}^{t+1} + h_{i,j-1}^{t+1} - 2h_{i,j}^{t+1}}{\Delta z^2} \right) \\
 &+ \mathcal{H}_4 \left( \frac{T_{i+1,j}^{t+1} + T_{i-1,j}^{t+1} - 2T_{i,j}^{t+1}}{\Delta x^2} + \frac{T_{i,j+1}^{t+1} + T_{i,j-1}^{t+1} - 2T_{i,j}^{t+1}}{\Delta z^2} \right) \\
 &+ \frac{K_{i,j+1}^t - K_{i,j-1}^t}{\Delta z}
 \end{aligned} \tag{A4}$$

$$\begin{aligned}
 & \mathcal{T}_1 \frac{T_i^{t+1} - T_i^t}{\Delta t} + \mathcal{T}_2 \frac{h_i^{t+1} - h_i^t}{\Delta t} \\
 &= \mathcal{T}_3 \left( \frac{T_{i+1,j}^{t+1} + T_{i-1,j}^{t+1} - 2T_{i,j}^{t+1}}{\Delta x^2} + \frac{T_{i,j+1}^{t+1} + T_{i,j-1}^{t+1} - 2T_{i,j}^{t+1}}{\Delta z^2} \right) \\
 &+ \mathcal{T}_4 \left( \frac{h_{i+1,j}^{t+1} + h_{i-1,j}^{t+1} - 2h_{i,j}^{t+1}}{\Delta x^2} + \frac{h_{i,j+1}^{t+1} + h_{i,j-1}^{t+1} - 2h_{i,j}^{t+1}}{\Delta z^2} \right) \\
 &+ \frac{(\mathcal{T}_5)_{i,j+1}^t - (\mathcal{T}_5)_{i,j-1}^t}{\Delta z}
 \end{aligned}$$

[A5]

Rearranging the two equations, a linear equation system can be constructed in order to solve for temperature  $T^{t+1}$  and matric potential  $h^{t+1}$ , i.e.,

$$\begin{aligned}
& \mathcal{H}_3 \frac{\Delta t}{\Delta x^2} h_{i+1,j}^{t+1} + \mathcal{H}_3 \frac{\Delta t}{\Delta x^2} h_{i-1,j}^{t+1} + \mathcal{H}_3 \frac{\Delta t}{\Delta z^2} h_{i,j+1}^{t+1} + \mathcal{H}_3 \frac{\Delta t}{\Delta z^2} h_{i,j-1}^{t+1} \\
& - \left( 2\mathcal{H}_3 \frac{\Delta t}{\Delta x^2} + 2\mathcal{H}_3 \frac{\Delta t}{\Delta z^2} + \mathcal{H}_1 \right) h_{i,j}^{t+1} \\
& + \mathcal{H}_4 \frac{\Delta t}{\Delta x^2} T_{i+1,j}^{t+1} + \mathcal{H}_4 \frac{\Delta t}{\Delta x^2} T_{i-1,j}^{t+1} + \mathcal{H}_4 \frac{\Delta t}{\Delta z^2} T_{i,j+1}^{t+1} + \mathcal{H}_4 \frac{\Delta t}{\Delta z^2} T_{i,j-1}^{t+1} \\
& - \left( 2\mathcal{H}_4 \frac{\Delta t}{\Delta x^2} + 2\mathcal{H}_4 \frac{\Delta t}{\Delta z^2} + \mathcal{H}_2 \right) T_{i,j}^{t+1} \\
& = -\mathcal{H}_1 h_{i,j}^t - \mathcal{H}_2 T_{i,j}^t - \frac{K_{i,j+1}^t - K_{i,j-1}^t}{\Delta z} \Delta t \\
& \mathcal{T}_3 \frac{\Delta t}{\Delta x^2} T_{i+1,j}^{t+1} + \mathcal{T}_3 \frac{\Delta t}{\Delta x^2} T_{i-1,j}^{t+1} + \mathcal{T}_3 \frac{\Delta t}{\Delta z^2} T_{i,j+1}^{t+1} + \mathcal{T}_3 \frac{\Delta t}{\Delta z^2} T_{i,j-1}^{t+1} \\
& - \left( 2\mathcal{T}_3 \frac{\Delta t}{\Delta x^2} + 2\mathcal{T}_3 \frac{\Delta t}{\Delta z^2} + \mathcal{T}_1 \right) T_{i,j}^{t+1} \\
& + \mathcal{T}_4 \frac{\Delta t}{\Delta x^2} h_{i+1,j}^{t+1} + \mathcal{T}_4 \frac{\Delta t}{\Delta x^2} h_{i-1,j}^{t+1} + \mathcal{T}_4 \frac{\Delta t}{\Delta z^2} h_{i,j+1}^{t+1} + \mathcal{T}_4 \frac{\Delta t}{\Delta z^2} h_{i,j-1}^{t+1} \\
& - \left( 2\mathcal{T}_4 \frac{\Delta t}{\Delta x^2} + 2\mathcal{T}_4 \frac{\Delta t}{\Delta z^2} + \mathcal{T}_2 \right) h_{i,j}^{t+1} \\
& = -\mathcal{T}_1 T_{i,j}^t - \mathcal{T}_2 h_{i,j}^t - \frac{(\mathcal{T}_5)_{i,j+1}^t - (\mathcal{T}_5)_{i,j-1}^t}{\Delta z} \Delta t
\end{aligned}$$

[A6]

Eq. [A6] represents the linear system that solves for  $T_{i,j}^{t+1}$  and  $h_{i,j}^{t+1}$ ,  $i, j = 1, 2, \dots, n$ . A Picard iteration procedure similar to the one shown for chapter 4 was also used here to determine the coefficients for the linear system.



## ACKNOWLEDGEMENTS

I would like to express the deepest appreciation to my major advisor, Dr. Robert Horton. I would like to thank him for the financial support and opportunity that supported me to complete my PhD program. His guidance, knowledge, encouragement and patience gave me both technical and emotional support to finish this thesis. I would also like to thank my committee members, Dr. Attinger, Dr. Jaynes, Dr. Rossmanith and Dr. Sauer for their help to complete this thesis.

I would like to thank Dr. Yuki Kojima for providing short probe TDR data. I would like to thank Dr. Mark Ankeny for introducing the water vapor diode concept and designs. I would like to thank all my colleagues in Agronomy and friends that accompanied me during the time of my study.

Lastly, I would like to thank my parents, Zhaokuan Wang and Yuye Hu, for their selfless help to support me to complete this study.